Carl von Ossietzky Universität Oldenburg

Characterization of industrially processed chalcopyrite solar cells with varied absorber composition

Von der Fakultät für
Mathematik und Naturwissenschaften
der Carl von Ossietzky Universität Oldenburg
zur Erlangung des Grades eines
Doktors der Naturwissenschaften
(Dr. rer. nat.)
angenommene Dissertation

von

Robin Knecht

geboren am 05. August 1981
in Haiger

Erstgutachter: Prof. Dr. Jürgen Parisi (Universität Oldenburg)
Zweitgutachter: Prof. Dr. Derck Schlettwein (Universität Gießen)

Tag der Disputation: 7. Dezember 2012

In honor of

All who came before us,

Dedicated to

Our children

Abstract

In the present thesis loss mechanisms in industrially processed chalcopyrite thin film solar cells were investigated. The investigations were conducted on heterojunction solar cells of the conventional ZnO:Al/i-ZnO/CdS/Cu(In,Ga)(Se,S)$_2$/Mo layer structure. Different conditions during chalcopyrite formation yielded absorbers with varying compositional depth profiles. Two processing methods have matured to commercial production of chalcopyrite Cu(In,Ga)(Se,S)$_2$ photovoltaic modules: (1) The chalcogenization of elemental precursors via annealing in a reactive atmosphere and (2) the co-evaporation of Cu, In, Ga and Se onto a heated substrate. The results of this thesis were obtained within two independent projects with different industry partners each applying either of these principally different processing technologies.

A comprehensive characterization procedure was devised and applied in order to strategically identify and evaluate the loss mechanisms in the photovoltaic device. This procedure revealed that in solar cells obtained from both processing methods the device performance was determined by similar features. These features were the specifics of the bandgap grading and the concentration of mid-gap defects.

The implementation of a front bandgap grading via sulfur incorporation in solar cells from the sequential deposition-reaction process (1) was the subject of the first industry project. In samples from this production method it is difficult to achieve the front grading with gallium which is generally used to realize the back grading. The segregation of a Ga-rich phase at the back contact and a Ga-depleted phase towards the heterojunction require the incorporation of sulfur at the absorber surface in order to realize the front grading. The sulfur incorporation widens the bandgap at the heterointerface which is expected to reduce interface recombination and consequently improve device performance. The results obtained from temperature dependent diode analysis and defect spectroscopy showed that the performance increase due to sulfur incorporation was rather caused by a passivation of mid-gap recombination centers.

The subject of the second project was the identification of those material characteristics which were responsible for performance variations observed in nominally equal processed solar cells produced in different co-evaporation chambers (2). Profiling the distribution of chemical elements revealed different slopes of the bandgap grading. The lower minimum bandgap in the sample featuring the stronger gradient contributed only partially to the reduced open circuit voltage which was found for this sample. Via one-dimensional simulations it was concluded that the most reasonable origin of the remaining open circuit voltage drop was due to a larger concentration of mid-gap defects.

Kurzfassung

In der vorliegenden Dissertation wurden die Verlustmechanismen in industriell gefertigten Chalkopyrit-Dünnschichtsolarzellen untersucht. Die Untersuchungen wurden an Solarzellen mit Heteroübergang durchgeführt, welche in der konventionellen Schichtstruktur ZnO:Al/i-ZnO/CdS/Cu(In,Ga)(Se,S)$_2$/Mo hergestellt wurden. Unterschiedliche Bedingungen während der Chalkopyritbildung resultierten in Absorbern, welche bezüglich der chemischen Zusammensetzung unterschiedliche Tiefenprofile aufwiesen. Zwei Herstellungsmethoden haben bei der kommerziellen Produktion von Cu(In,Ga)(Se,S)$_2$ Photovoltaikmodulen Marktreife erlangt: (1) Die Chalcogenisierung elementarer Vorläuferschichten durch Erhitzen in einer reaktiven Atmosphäre und (2) die Koverdampfung von Cu, In, Ga und Se auf ein erhitztes Substrat. Diese Abschlussarbeit wurde angefertigt im Rahmen zweier unabhängiger Projekte mit unterschiedlichen Industriepartnern, welche je eine dieser prinzipiell unterschiedlichen Herstellungsmethoden angewendet haben.

Um die Verlustmechanismen im photovoltaischen Bauteil zu identifizieren und zu bewerten wurde eine umfassende Charakterisierungsprozedur entwickelt und angewendet. Mittels dieser Prozedur zeigte sich, dass in Solarzellen hergestellt mit beiden Prozessierungsmethoden, das Betriebsverhalten durch ähnliche Eigenschaften bestimmt wurde. Diese Eigenschaften waren der spezifische Bandlückenverlauf sowie die Konzentration der Bandlückenmittendefekte.

Die Implementierung eines Bandlückengradienten an der Vorderseite durch Schwefeleinbau in Solarzellen aus dem sequentiellen Abscheidung-Reaktion Prozess (1) war das Thema des ersten Industrieprojektes. In Proben aus diesem Herstellungsprozess ist es schwierig den Bandlückengradienten an der Vorderseite mittels Gallium zu realisieren, welches üblicherweise zur Erstellung des Bandlückengradienten zum Rückkontakt verwandt wird. Die Phasentrennung zwischen einer Gallium-reichen Phase am Rückkontakt und einer Gallium-verarmten Phase in Richtung des Heterokontakts machen den Einbau von Schwefel an der Absorberoberfläche notwendig, um den Bandlückengradienten an der Vorderseite zu realisieren. Der Schwefeleinbau verbreitert die Bandlücke an der Heterogrenzfläche, was voraussichtlich die Grenzflächenrekombination reduziert und folglich die Leistung des Bauteils verbessert. Die Ergebnisse, welche durch die Temperatur abhängige Analyse der Diodenparameter und durch Störstellenspektroskopie gewonnen wurden, zeigten, dass die Erhöhung der Leistung eher durch Passivierung von Rekombinationszentren in der Mitte der Bandlücke verursacht wurde.

Thema des zweiten Projektes war die Identifizierung derjenigen Materialcharakteristika, welche für die Leistungsunterschiede verantwortlich sind, die in Proben beobachtet wurden, die unter nominell gleichen Prozessbedingungen in unterschiedlichen Koverdampfungskammern hergestellt wurden (2). Die Tiefenprofile der chemischen Zusammensetzung offenbarten unterschiedliche Steigungen der Bandlückengradienten. Das niedrigere Bandlückenminimum befand sich in der Probe mit dem steilsten Gradienten und lieferte einen Teil der Erklärung für die reduzierte Leerlaufspannung in dieser Probe. Mittels ein-dimensionaler Simulationen wurde gefolgert, dass die naheliegendste Ursache für den übrigen Verlust der Leerlaufspannung eine höhere Konzentration an Bandlückenmittendefekten ist.

Contents

1 Preface:

This work is a dissertation presented to achieve the German academic degree of doctor of natural sciences (Dr. rer. nat.). It is devised as a thesis by publication and is based on three articles which have been published in or submitted to peer reviewed journals from the field of applied and solid state physics. The common theme of all articles is the characterization of chalcopyrite Cu(In,Ga)(Se,S)$_2$ photovoltaic devices which were manufactured in the same production lines as large-area modules for the mass market. The articles resulted from the work on two independent projects in collaboration with two different industrial partners. Both are manufacturers of chalcopyrite photovoltaic modules albeit their processing technology is fundamentally different. Due to these boundary conditions the focus of each project varied, however, in each case a comprehensive characterization was required. This characterization was performed at the Energy- and Semiconductor Research Laboratory (EHF) at the University of Oldenburg.

In this thesis a characterization procedure was devised to identify the loss mechanisms present in the investigated absorber variations. At the outset of each measurement series a basic characterization was performed in order to identify those macroscopic cell parameters which were affected by the process variation. With the obtained results suitable and more advanced methods were identified and subsequently applied to gain a deeper insight about the loss mechanisms. Despite the different focus at the outset of each project the influence of bandgap gradings and defects on the device performance was a common issue.

The questions investigated with the procedure were the implementation of a double bandgap grading with the deposition-reaction process in the first project and the reproducibility of the module performance with different co-evaporation chambers in the second project. In the first project the absorber variations were prepared by reaction in atmospheres with different H$_2$Se/H$_2$S concentration. A larger sulfur incorporation into the chalcopyrite close to the heterojunction widens the bandgap which repels charge carriers from the heterointerface. It is expected that this reduces interface recombination and increases overall device performance and the investigations on this issue resulted in the articles in chapters 3 and 4. The second project resulted in the article presented in chapter 5. Two samples were examined which were nominally produced under equal conditions in two separate evaporation chambers. Their open circuit voltage differed significantly raising the question about the elementary material characteristics which cause these deviations. The clarification of this issue is important in order to improve the reproducibility and homogeneity of the module production.

In chapter 3, the absorber modifications Cu(In,Ga)Se$_2$ and Cu(In,Ga)(Se,S)$_2$ manufactured via rapid thermal processing of metal precursors were examined. In a first phase of the reactive annealing both samples were exposed to selenium only, while during a second annealing phase the atmosphere contained either selenium or sulfur. Current-voltage measurements showed that the sulfurized samples exhibit an improved power conversion efficiency which is caused by a slightly increased fill factor and substantially higher open circuit voltage. The introduction of sulfur caused a significant decrease of the surface doping concentration which leads to widening of the space charge region as observed with capacitance-voltage measurements. Ideality factors determined from temperature dependent diode analysis suggested a reduction of the space

charge region recombination in sulfur containing devices. Compared to neat Cu(In,Ga)Se$_2$ devices this would result in a larger splitting of the quasi-Fermi levels and therefore an enhanced open circuit voltage.

The improvement caused by the incorporation of sulfur was further investigated in chapter 4. In this study four modules were exposed to different sulfur concentrations during the reactive annealing. Using electrical characterization, composition profiling and defect spectroscopy the enhancement of the open circuit voltage was mainly attributed to a reduced minority carrier trap concentration in the sulfur-rich samples. Structural characterization techniques showed differences in the formation of the interfacial Mo(S,Se)$_2$ layer which could not be explained by the different sulfurization conditions alone and emphasized the importance of detailed process control.

This issue of process control was further pursued in the second project. The subject of chapter 5 was deviations of module performance due to an incomprehensive control of process parameters. Samples processed by the co-evaporation deposition method which were apparently manufactured under equal production conditions exhibited substantial deviations of the open circuit voltage and the fill factor. Applying fundamental device analysis, space charge and defect spectroscopy, depth profiling of the chemical gradients of the absorber films as well as transient photoluminescence access to fundamental device characteristics was gained which were used to set up a one-dimensional simulation baseline. Based on the simulation results it was concluded that the apparent deviations are related to variations of the band gap grading and the presence of deep recombination centers with different concentration within the Cu(In,Ga)Se$_2$ absorber.

In chapter 2 the reader is acquainted to chalcopyrite photovoltaic devices and the methodological background of the investigations detailed in the articles. After the research is motivated the multinary material system of chalcopyrites is introduced and the different production methods are presented in detail. Subsequently the characterization procedure and the applied experimental and analysis methods are introduced. The results of this thesis are summarized in chapter 6.

The presented articles were prepared in cooperation with the named co-authors and further partners which chose not to be mentioned. The following listing highlights the contributions of each author to the individual publications.

(1) R. Knecht, M. Knipper, J. Ohland, I. Riedel, J. Parisi, "*Optoelectronic characteristics of Cu(In,Ga)(S,Se)$_2$ thin film solar cells obtained from varied chalcogenization processes*", Thin Solid Films 519 (2011) 7324–7327

R. Knecht:	thermal evaporation of metal contact grid, sample preparation, characterization strategy, all measurements and analysis, composition of the manuscript, discussion with reviewers
M. Knipper:	discussion with reviewers
J. Ohland, I. Riedel, J. Parisi:	discussions
Unnamed industry partner:	sample manufacturing

(2) R. Knecht, M. S. Hammer, J. Parisi, I. Riedel, "*Impact of varied sulfur incorporation on the device performance of sequentially processed Cu(In,Ga)(Se,S)$_2$ thin film solar cells*", Physica Status Solidi (a) (status: submitted)

R. Knecht:	thermal evaporation of metal contact grid, sample preparation, characterization strategy, all measurements and analysis, composition of the manuscript, discussion
M. S. Hammer:	assistance with performance and evaluation of the DLTS measurements, discussions
I. Riedel, J. Parisi:	discussions
Unnamed industry partner as in (1):	sample manufacturing
Other:	
GDOES measurements:	R. Knecht, R. Meishner
XRD measurements:	R. Knecht, U. Mikolajczak, M. Knipper

(3) R. Knecht, J. Parisi, I. Riedel, R. Schäffler, B. Dimmler, "*Investigation of CIGSe Solar Cell Performance Deviations in Nominally Equal Absorbers*", Japanese Journal of Applied Physics 51 (2012) 10NC07

R. Knecht:	sample preparation, characterization strategy, all measurements and simulations (except methods mentioned below), analysis, composition of the manuscript, discussion with reviewers
I. Riedel:	defect spectroscopy, discussions
J. Parisi:	discussions
R. Schäffler, B. Dimmler: (Manz, formerly Würth Solar)	sample manufacturing, discussions
Other:	
TRPL measurements:	J. Ohland, V. Gerlitz
GDOES measurements:	R. Knecht, R. Meishner

2 Introduction:

2.1 Motivation

Solar radiation as the origin of light, heat and subsequently wind and rain provides us with an abundant amount of energy. Primary energy in the form of electromagnetic radiation is stored as kinetic energy of air and water masses, chemical energy in biomass and by extension of the latter even fossil fuels [1]. A multitude of technologies have been developed [2] to harvest the different forms of energy from the sun. Photovoltaic (PV) is the latest of these technologies and was seriously developed only since the 1950s [3]. By transforming the light energy of photons into low entropy electric energy PV is the most direct and thus efficient method to capture the energy from the sun [4].

A considerable amount of semiconductor materials and compounds have been discovered which are suitable for PV power generation [3,8]. Several production methods have been invented in order to increase production output and quality at decreasing cost for the mass market [9]. Thin-film technologies belong to the second generation of PV, and having entered the market place only in recent years they hold great potential [10]. Their production uses only a small amount of material compared to devices based on crystalline silicon and enables the integrated production of interconnected modules. This allows for quicker, more energy efficient and cheaper manufacturing of modules [11,12] with energy payback times below a year for South European insolation conditions [13].

Thin film chalcopyrite photovoltaic devices based on the multinary compound $Cu(In,Ga)(Se,S)_2$ (CIGSSe) have achieved power conversion efficiencies over 20% in the laboratory [6]. Being a direct semiconductor, CIGSSe has excellent absorption properties [14], absorbing almost all light within a layer thickness of 2 µm [15]. Considering that this p-type semiconductor is usually grown as polycrystalline film in a rather slim process window and is composed of five elements, its performance is remarkably tolerant against structural defects and off-stoichiometry [16]. By changing the [Ga]/([Ga]+[In]) ratio (GGI) and the [S]/([S]+[Se]) ratio (SSSe) the bandgap can be tuned in a wide range between 1.04 eV and 2.43 eV [5] which includes the optimum bandgap range 1.1 eV-1.5 eV for photovoltaic power generation [4,17]. However, despite 30 years of research some physico-chemical characteristics of the absorber have not been fully understood, e.g. metastabilities [18], the formation and specific nature of interface layers [19] or the origin of a characteristic defect signature called N1 [20]. But not only the absorber is the subject of ongoing research, many studies investigate alternative buffer [21] and window layers [22], back contact materials [23] and various substrate options [24].

Figure 2.1: Development of CIGSSe research cell and module efficiencies of chalcopyrite devices manufactured with the co-evaporation and deposition-reaction (Dep-Rec) method (after [5–7])

Module efficiencies trail behind the laboratory champion cells by a few years

(see Figure 2.1). The efficiency gap is expected to decrease by means of better control of the process parameters and transfer of the laboratory know-how onto large-scale production [25–27]. However, with the characterization methods available to the manufacturer some features of the device, which are crucial for the performance, are not accessible because the required methods for their detection are not inline capable.

Inline capable methods need to be quick and non-destructive. For example performance parameters can be quickly accessed by

Figure 2.2: Interaction of the project partners: The industrial partners manufacture the samples (details in Figure 2.6) and provide them to the research laboratory where they are investigated via a comprehensive characterization procedure (specifics in Figure 2.7). Feedback on material properties inaccessible to the industry partners enables the production of improved samples.

flashing [28] or modules with a high concentration of shunts can be detected by electroluminescence measurements [29]. Sometimes methods are available which are not inline capable, like x-ray diffraction for the detection of crystal phases or x-ray fluorescence for control of the integral ratios of chemical elements, and they are employed for spot checking of the production output. However, even these methods might not be capable to detect crucial properties like the distribution of chemical elements in the absorber. As laboratory record cells inhibit sophisticated bandgap gradings which are implemented by varying the GGI or SSSe ratios throughout the absorber thickness, knowledge of the chemical profiles is substantial [30]. However, detection of the distribution of chemical elements requires successive removal and analysis of the absorber material which is a destructive method. A second crucial device feature which influences losses via recombination is the presence of defects in the material. The detection of defects, however, is very time consuming and special care has to be taken with sample preparation. It is of great scientific interest to understand the influence of features like the bandgap grading or defects in order to develop new models or methods which help to improve the device performance.

The purpose of this work is the identification of the limiting mechanisms in chalcopyrite photovoltaic devices by establishing a comprehensive characterization procedure which includes those time-consuming and destructive methods not available to industrial manufacturers. The research was conducted in a dedicated research laboratory (EHF) over the course of two industrial projects. The characterization procedure was applied on several absorber variations and by application of advanced methods their characteristic features could be detected. These features were communicated and discussed with the industry partner thus enabling the production of improved devices (Figure 2.2).

2.2   Chalcopyrite photovoltaic devices

This chapter provides information about the photovoltaic devices studied in this thesis. The formation of the chalcopyrite absorber is influenced by indiffusion of elements from other layers in the stack structure. Therefore the layer sequence which constitutes the solar cell device is introduced before the chalcopyrite absorber material is described in more detail. After this the

Figure 2.3: a) Scanning electron microscope image of the cross section through a chalcopyrite solar cell with an absorber manufactured by the deposition-reaction method b) Schematic cross section of an exemplary CIGSSe module detailing the device layer structure and the monolithical serial interconnection achieved by the P1, P2 and P3 scribes (dimensions strongly out of scale). At P2 the front contact of the left cell is in contact with the back contact of the right cell.

band diagram of the solar cell and the function of a graded bandgap are discussed. Strategies to realize bandgap gradings are briefly touched upon in the subsequent section which introduces the two most common processing methods which are applied in commercial production. The final section of this chapter treats difficulties with up-scaling from laboratory solar cells to large modules and explains the integrated serial connection of multiple solar cells.

2.2.1 Device structure

The chalcopyrite devices investigated in this thesis are designed in the conventional layer structure (shown in Figure 2.3) which is well established and documented [31]. Due to its thin-film nature the layer stack has been successfully deposited on curved and even flexible substrates from various materials like steel or polyamide [24,32,33]. This does have advantages as this enables the application of more cost efficient processing methods (e.g. roll-to-roll) and creates new market opportunities beyond flat panels. However, the studied samples were deposited on flat soda-lime glass sheets which currently are the most widely used substrates in industrial development. Soda-lime glass is the most reliable substrate because it has a similar thermal expansion coefficient as CIGSSe [5] and chalcopyrite devices on soda-lime glass yield the largest power conversion efficiencies. A milestone in the understanding of CIGSSe solar cells was the discovery of the beneficial effects of sodium diffusion from the soda-lime glass substrate into the absorber which are detailed in the next section [34]. Therefore on sodium-free substrates an additional layer which contains sodium, i.e. sodium selenide, is added [35]. In order to achieve more control about this so-called "substrate effect", a sodium diffusion barrier is deposited onto sodium containing substrates which is followed by the controlled deposition of a layer containing sodium [5,36].

Onto the substrate a molybdenum layer is deposited by DC magnetron sputtering as back contact which is chosen for its cost effectiveness [23,37] and tendency to form a $MoSe_2$ layer [38,39] during the subsequent processing of the chalcopyrite absorber [40]. If the $MoSe_2$ layer is present in the hexagonal structure and its c-axis is perpendicular to the Mo surface it results in a more ohmic contact and improved adhesion [37,41] of the adjacent absorber on the back electrode. It further reduces the valence band offset to the Mo back electrode improving majority carrier injection [42,43].

The majority of charge generation happens in the polycrystalline p-type chalcopyrite absorber which will be discussed in more detail in the next section. The pn-heterojunction [44] is realized by deposition of two thin buffer layers and a highly n-doped window layer. A thin n-type CdS buffer layer with a bandgap of about 2.4 eV is deposited directly on the absorber [45]. Most widely this is achieved by chemical bath deposition (CBD) [31] though other deposition methods are investigated [46]. As Cd is toxic, its use in the buffer layer encourages research into buffer layer alternatives like ZnS, $In(O,H)_xS_y$ [47–50]. Still the advantages of CBD-CdS like removal of surface oxides and low lattice mismatch with the absorber overweight the disadvantages of toxicity and inline-incapability [31]. A thin i-ZnO layer (not visible in Figure 2.3a) is deposited onto the CdS. Its major role is the filling of pinholes in CdS and providing protection against the sputtering of the transparent conductive oxide (TCO) [51,52].

For charge carrier collection the device layer stack is completed with a highly conductive n-type window layer as a front contact exhibiting a large bandgap which is transparent for the majority of the solar spectrum. Highly doped ZnO:Al deposited via DC magnetron sputtering is the most common TCO in commercial applications due to its low cost [51], though alternatives like ZnO:B, In_2O_3:Mo (IMO), In_2O_3:Ti (ITiO), and others are investigated [22]. The bandgap of 3.3 eV [45] limits high energy photons to reach the absorber and free-carrier absorption in the TCO reduces the number of charge carriers generated at larger wavelengths [53]. Since the latter scales with the TCO thickness a trade-off between TCO resistance losses and absorption losses has to be made.

2.2.2 Chalcopyrite materials

The chalcopyrite absorber is a p-type direct bandgap semiconductor which is grown in a polycrystalline phase in commercial devices [31]. The unit cell of the chalcopyrite structure (see Figure 2.4) is composed of chemical elements from groups I, III and VI in the ratio I-III-VI$_2$ and is based on a double zinc-blende structure. Specifically the materials investigated in this thesis contain the elements Cu (I), In and Ga (III) as well as Se and S (VI). Different mixing ratios $x = [Ga]/([Ga]+[In])$ and $y = [S]/([Se]+[S])$ within group III resp. VI influence the unit cell dimensions a and c in accordance to Vegard's law [54,55]. This enables the calculation of the $Cu(In_{1-x}Ga_x)(Se_{1-y}S_y)_2$ crystal dimensions from the neat ternary chalcopyrites (see Table 2.1):

$$a_{Cu(In_{1-x}Ga_x)(S_ySe_{1-y})_2} = xy\, a_{CuGaS_2} + x(1-y)\, a_{CuGaSe_2} + (1-x)y\, a_{CuInS_2} + (1-x)(1-y)\, a_{CuInSe_2}$$
$$c_{Cu(In_{1-x}Ga_x)(S_ySe_{1-y})_2} = xy\, c_{CuGaS_2} + x(1-y)\, c_{CuGaSe_2} + (1-x)y\, c_{CuInS_2} + (1-x)(1-y)\, c_{CuInSe_2}$$

$$(2.1)$$

By increasing the gallium content the conduction band minimum increases while the valence band position is essentially not affected. This results in an increased bandgap E_g and decreasing electron affinity χ (see Figure 2.5) [56,57]. In contrast, the addition of sulfur increases the conduction band minimum and decreases the valence band maximum almost symmetrically [58,59]. The different alignment of the conduction and valence band upon variation of x resp. y is explained by a common internal reference energy for band alignment in the Cu(In,Ga)(Se,S)$_2$ alloy

Crystal	a (Å)	c (Å)	E_g (eV)
CuGaS$_2$	5.35	10.46	2.40
CuGaSe$_2$	5.61	10.98	1.70
CuInS$_2$	5.52	11.13	1.45
CuInSe$_2$	5.78	11.62	1.00

Table 2.1: Crystal dimensions [5] and energy bandgap of the ternary chalcopyrite phases according to eq. (2.2)
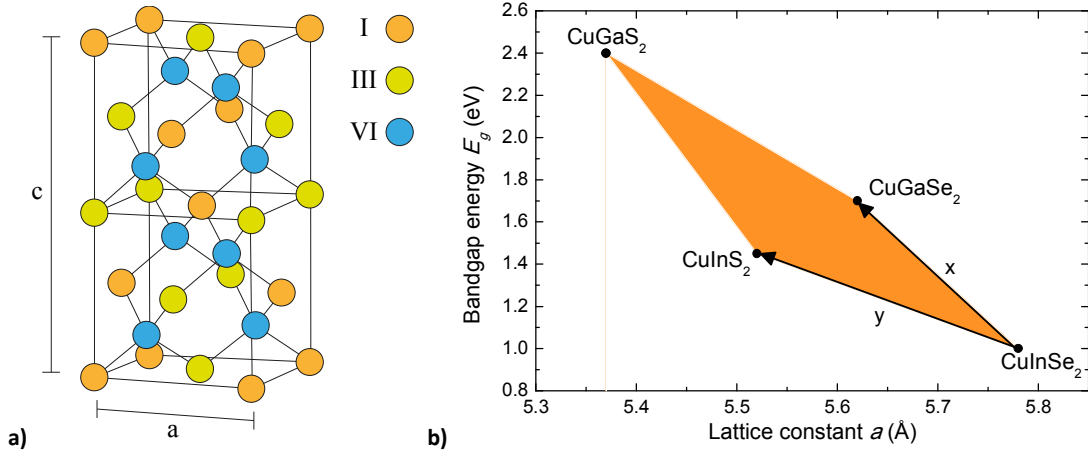
Figure 2.4:   a) Chalcopyrite unit cell (based on [31]) b) Range of bandgaps available by tuning *x* and *y*

system which is identified as the dominant acceptor level. The energetic depth of this reference level does not change with increasing *x* but becomes larger with the increase of *y* which results in the relative reduction of the valence band. The dependence of E_g on *x* and *y* is in fact not linear and corrected with bowing factors resulting in the following empirical formula [60]:

$$
E_{g,Cu(In_{1-x}Ga_x)(S_ySe_{1-y})_2} =
$$
$$
(0.98 + 0.167x^2 + 0.17y^2 + 0.023x^2y - 0.17xy^2 + 0.397xy + 0.31y + 0.523x)\ eV
$$

(2.2)

According to equation (2.2) the bandgap can be tuned in the range of 1.0 eV-2.4 eV (see Figure 2.4b) such that the bandgap can be optimally adjusted to the solar spectrum. However, the incorporation of gallium or sulfur has additional effects which will be discussed next.

In the phase diagram the existence window for the desired chalcopyrite α phase is rather slim but the presence of gallium during chalcopyrite formation widens this process window and increases the reproducibility of the α phase [61]. In CIGSSe prepared by co-evaporation a maximum grain size was observed at about *x* = 0.23 which corresponds to the ratio *c/a* = 2 indicating that strain during growth influences the grain size [62]. A minimum of the bulk defect density was observed for *x* = 0.3 [63]. In S-free devices this ratio corresponds to E_g = 1.15 eV which is very close to the second maximum of the theoretical calculations for the most efficient bandgap under terrestrial conditions [4]. In the deposition-reaction process the formation of the indium rich chalcopyrite is kinetically faster than the formation of the Ga-rich chalcopyrite which leads to a phase segregation and accumulation of the Ga-rich phase at the back contact [64]. The gradual increase of the conduction band acts as an electron mirror effectively reducing back contact recombination [65]. The sulfur concentration is observed to increase towards the absorber back and front surfaces [66]. At the latter the increased interface bandgap could reduce interface recombination. This increases the open circuit voltage which is suggested to be further enhanced by sulfur-induced passivation of recombination centers [67].

As mentioned in the previous section sodium diffusion into the absorber has beneficial effects. Widening the process window for α-CIGSSe formation [68] it supports the growth of larger grains [34] and a higher degree of crystal orientation [69]. However, grain size does not seem to be limiting CIGSSe performance, which is explained by sodium in the grain boundaries. Sodium catalyses the oxidation of dangling bonds in the form of selenium vacancies at the surface and

reduces the density of this compensating donor which increases the p-type conductivity of the material [34,70,71].

The complexity of the polycrystalline multinary compound CIGSSe causes many electronic defects. The defect levels of vacancies, interstitials and anti-sites were calculated for $CuInSe_2$ and $CuGaSe_2$ [69,72–74]. Shallow acceptor states like the copper vacancy appear to be the origin of the intrinsic p-type doping, other candidates are the Cu_{In} anti-site and indium vacancy [75]. Defects may form electronically passive defect complexes like $(V_{Cu}-In_{Cu})$ such that the performance is not inhibited by large defect concentrations. The absorber surface is commonly observed to be copper depleted [61,76] and formation of aggregated $(V_{Cu}-In_{Cu})$ defect pairs results in the off-stoichiometry phases $CuIn_3Se_5/Cu_2In_5Se_9$ also called ordered defect compounds (ODC) [16,77]. Their bandgap is about 1.4 eV which is wider than $CuInSe_2$ [78]. Mainly the valence band position is reduced which increases the type inversion at the heterojunction [45]. However, the general presence of this layer is debated [31].

2.2.3 Band diagram and bandgap grading

Figure 2.5 shows the simulated one dimensional band diagram of a CIGSSe device manufactured with the deposition-reaction process similar to the samples investigated in chapter 3 and 4. Due to the large doping of the window layer ($N_D \sim 10^{18}$ cm^{-3}) as compared to the doping density in the CIGSSe ($N_A \sim 10^{16}$ cm^{-3}) the space charge region (SCR) extends mainly into the absorber. The large band bending at the heterojunction brings the Fermi level close to the conduction band giving this region n-type character. This is called the type inversion which causes the location of maximal recombination where the concentration of electrons n equals the hole concentration p to shift away from the defect-rich interface.

The ability to tune the chalcopyrite bandgap [30,79,80] by controlling the mixing ratios opens
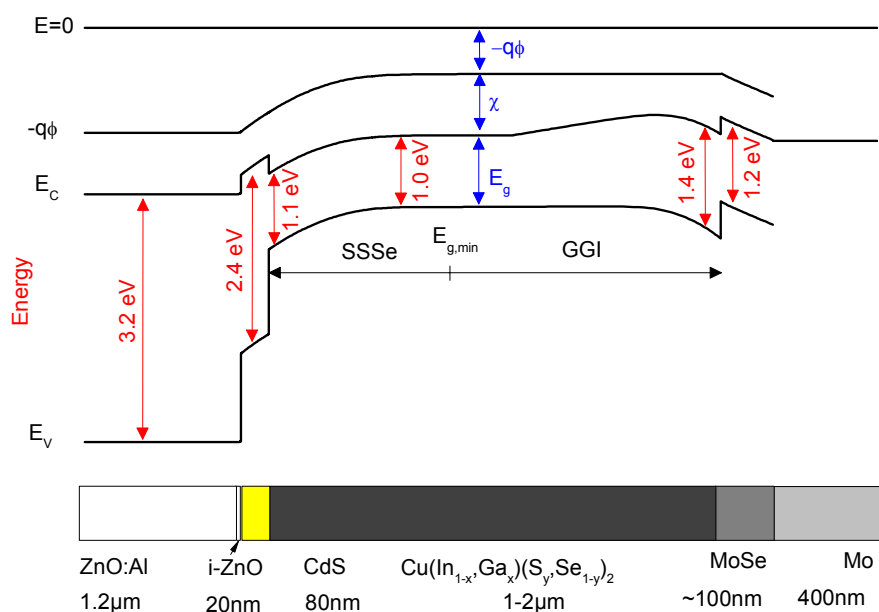
Figure 2.5: Band diagram of a chalcopyrite solar cell device structure. This one dimensional presentation represents a double bandgap grading as in devices examined in chapter 4 and is not valid for all samples investigated in this thesis. In this specific example the front grading is achieved by an increase of *y* whereas the back grading is realized by an increase of *x*.

the opportunity to engineer bandgap gradings in the device. In the best devices a double bandgap grading is used to repel one charge carrier species from the interface. In Figure 2.5 the separation of a Ga-depleted and a Ga-rich phase is evident in the increase of the conduction band minimum towards the back contact. This establishes a back surface field for the minority charge carriers which decreases the back surface recombination velocity [81]. In absorbers where minority charge carriers have only a short diffusion length the carrier collection can be improved by a more uniform grading over the whole of the bulk [30,65]. Note that the distance of the valence band to the vacuum energy stays relatively constant. The minimum bandgap is situated around the edge of the space charge region.

In devices from the co-evaporation process it is possible to realize the front grading as well via an increase of the gallium concentration. The conduction band offset at the CdS/CIGSSe interface which appears as a spike in Figure 2.5 decreases with increasing Ga concentration eventually forming a cliff. This increases the energetic distance between the Fermi level and the absorber conduction band minimum which reduces the type inversion [82]. Therefore it is more suitable to implement the front grading by incorporation of sulfur at the heterojunction since the reduction of the valence band enhances the type inversion [58]. As sulfur is preferentially incorporated close to the heterojunction and at the back contact, carrier collection is not influenced by sulfur. Therefore mainly the open circuit voltage is improved and no increase of the short circuit current density is expected [31]. Because of the band bending the widening at the heterojunction due to sulfur is barely visible in Figure 2.5. The band diagram also shows the $MoSe_2$ layer between the absorber and the back contact which reduces the Schottky type behavior of a CIGSSe/Mo interface [83].

2.2.4 Absorber Manufacturing

A multitude of production methods for the chalcopyrite absorber have been developed in order to improve process quality and processing speed and/or further decrease manufacturing costs. While chalcopyrite films were successfully deposited via chemical vapor deposition [84], spray pyrolysis [85], electrodeposition [86] and a few other methods [31,87], only co-evaporation [88] and the deposition-reaction method [89] have matured to industrial mass production. Since samples from both the co-evaporation and the deposition-reaction method have been investigated these two processing methods are briefly described in the following sections.

Deposition – Reaction

The deposition-reaction process is characterized by two separate stages (upper route in Figure 2.6). In the first stage a stack of slightly copper-poor precursor layers consisting of Cu, Ga and In is deposited onto the Mo back contact through sputtering [66], electrodeposition [41], screen printing [90] or other methods [31]. The [Cu]/([In]+[Ga]) ratio as well as the GGI of the final absorber are controlled by the composition of the precursor layer [66]. The precursor stack is called stacked elemental layer if Se or optionally Na is also deposited during this stage [91]. The chalcopyrite absorber is formed in a second stage at temperatures between 400 K-500 K in a reactive atmosphere composed of either H_2Se/H_2S at ambient pressure [41,92], Se vapor [93] or using rapid thermal processing (RTP) [94,95]. The p-type conductivity is explained by the low formation energy of native shallow acceptors (V_{Cu}) and can be increased by annealing in selenium overpressure [16,75]. By annealing in low selenium pressure, however, the material becomes more n-type which is explained by an increase of selenium vacancies which act as

compensating donors [31,75]. Since the formation of CuGa(Se,S)$_2$ is kinetically delayed as compared to CuIn(Se,S)$_2$ [96,97] often a phase separation of the In-rich phase at the front and a Ga-rich phase [64] at the back contact is observed. In order to counteract this effect and achieve a smoother bandgap grading many alternative sequences of precursor layer arrangements are employed [98,99]. In RTP the Ga diffusion to the front can alternatively be improved by annealing at larger temperatures which also increases MoSe$_2$ formation rates due to Se overpressure [31]. Because of the lack of Ga at the heterojunction the desired bandgap widening is achieved via the incorporation of sulfur [100]. Laboratory record efficiencies of sequentially processed solar cells are below the efficiencies achieved with solar cells manufactured by co-evaporation. Even though, this method can be more easily upscaled such that champion modules obtained by this method rival the ones from co-evaporation (see Figure 2.1). However, it is more difficult to control the reaction and diffusion processes during absorber formation [5]. The modules investigated in this thesis were manufactured through precursor deposition via DC-magnetron sputtering and RTP. In chapter 3 the effects of changing the annealing atmosphere from H$_2$Se to H$_2$S were examined which was further explored in chapter 4 by varying the partial pressure of H$_2$S during annealing.

Co-Evaporation

The simultaneous thermal evaporation of the absorber constituents from multiple elemental effusion cells onto the heated substrate is called co-evaporation (lower route in Figure 2.6). The absorber grows directly from the gas phase and growth rate and composition can be directly controlled through the flux intensity [15] and distribution of the elemental sources [101,102]. Best results have been achieved with an overall slight Cu deficiency and excess Se. The classical method of growing the chalcopyrite in a single step [103] with all sources active has been further developed by several laboratories. In order to engineer sophisticated absorbers multistage processes are employed [101,104] in which sequentially different combinations of elements are evaporated providing better control of the reaction kinetics. Through this flexibility Cu(In,Ga)Se$_2$ layers with improved crystallinity [105], advanced bandgap gradients [106] and the chalcopyrite record efficiencies on the laboratory scale have been achieved [107]. The modules investigated in chapter 5 have been manufactured using the single stage co-evaporation process.
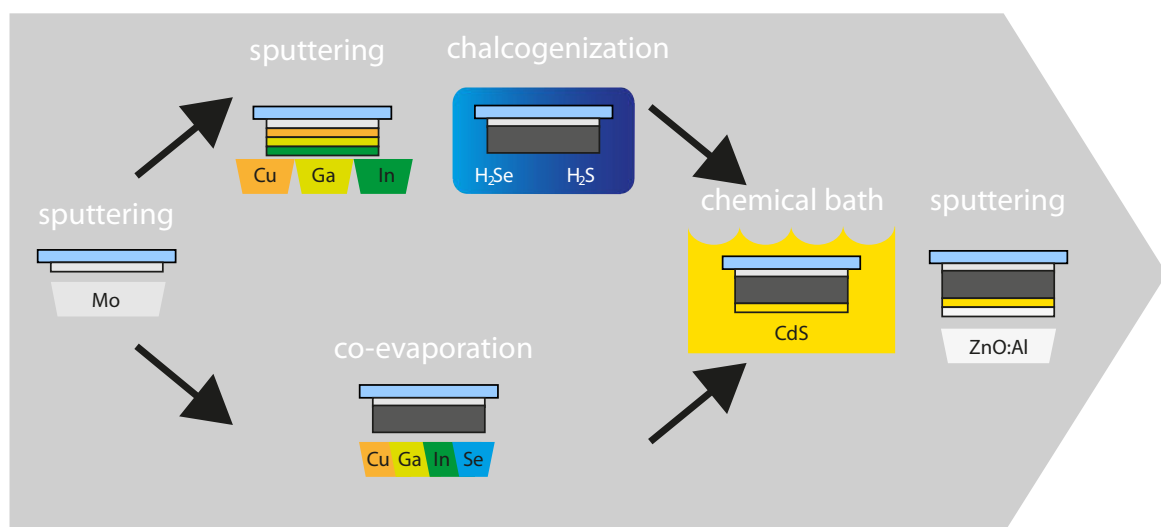
Figure 2.6:   CIGSSe deposition methods for the samples provided by the industry partners (compare Figure 2.2): upper route: deposition reaction method, lower route: co-evaporation.

2.2.5   Module design aspects

Commercial modules are designed differently to laboratory champion cells in a few important aspects. In order to achieve reasonable voltages photovoltaic modules are composed of many cells in a serial connection. Thin film production allows for cost-efficient monolithic serial connection of the cells by inclusion of mechanical and laser scribing steps during manufacturing (see Figure 2.3b) [31]. Three patterning steps P1-P3 are required to realize a monolithic interconnection of cell stripes [108]: P1 and P3 separate the back and front electrodes of the adjacent cells, while P2 establishes the series connection between neighboring cells by the direct connection of the two electrodes. This has the main advantage that no additional collection grids are necessary which reduces shadow casting. However, this is offset by the disadvantage that the region between P1 to P3 (W_{loss} in Figure 2.3b) cannot be used for power generation leaving parts of the aperture area unused. Anti-reflective coatings are able to reduce reflection losses below one percent but the need for a cover glass on modules renders this impractical [31]. Transparent conductive oxides form the serial interconnection and are thicker than in laboratory cells to reduce ohmic losses, however, this causes further losses due to free carrier absorption [109]. With large area processing homogeneous devices are more difficult to achieve. Variations in layer thicknesses could result in local shunts which reduce the fill factor (see next section). Lateral variations in composition might lead to fluctuations of the valence and conduction bands. These energy band fluctuations enhance radiative and non-radiative recombination processes which decrease device performance substantially [110,111].

2.3   Characterization methods

In the first section of this chapter an overview of the methodological approach is provided and the relations between the characteristic physical quantities are visualized along with the methods which were identified and applied to extract them (Figure 2.7). In the following sections the applied methods are briefly introduced and literature references are supplied for more details. For the principles of photovoltaic device physics refer to [4,44]. A brief background to device simulation is presented in the last section, as in chapter 5 one dimensional simulations are performed in order to analyze the influence of different bandgap gradings on the device performance.

2.3.1   Methodical Approach

Primary goal of the characterization procedure is to identify the loss mechanisms in photovoltaic devices. By establishing a reasonable sequence of experiments, losses observed in macroscopic cell parameters can be narrowed down to material and device characteristics. The knowledge of these characteristics forms the basis for the development of further optimization strategies. An established diagnosis chain could enable a quick, focused and efficient identification of the crucial loss mechanisms and support cell development in research and production. The application of such a problem oriented characterization procedure has the additional advantage that many material, interface, and device characteristics are assessed which can be used as input parameters for device simulations. The development of a simulation baseline has the further advantage that the device properties like bandgap grading, layer sequence and material and interface characteristics can be easily modified in order to further optimize the device.
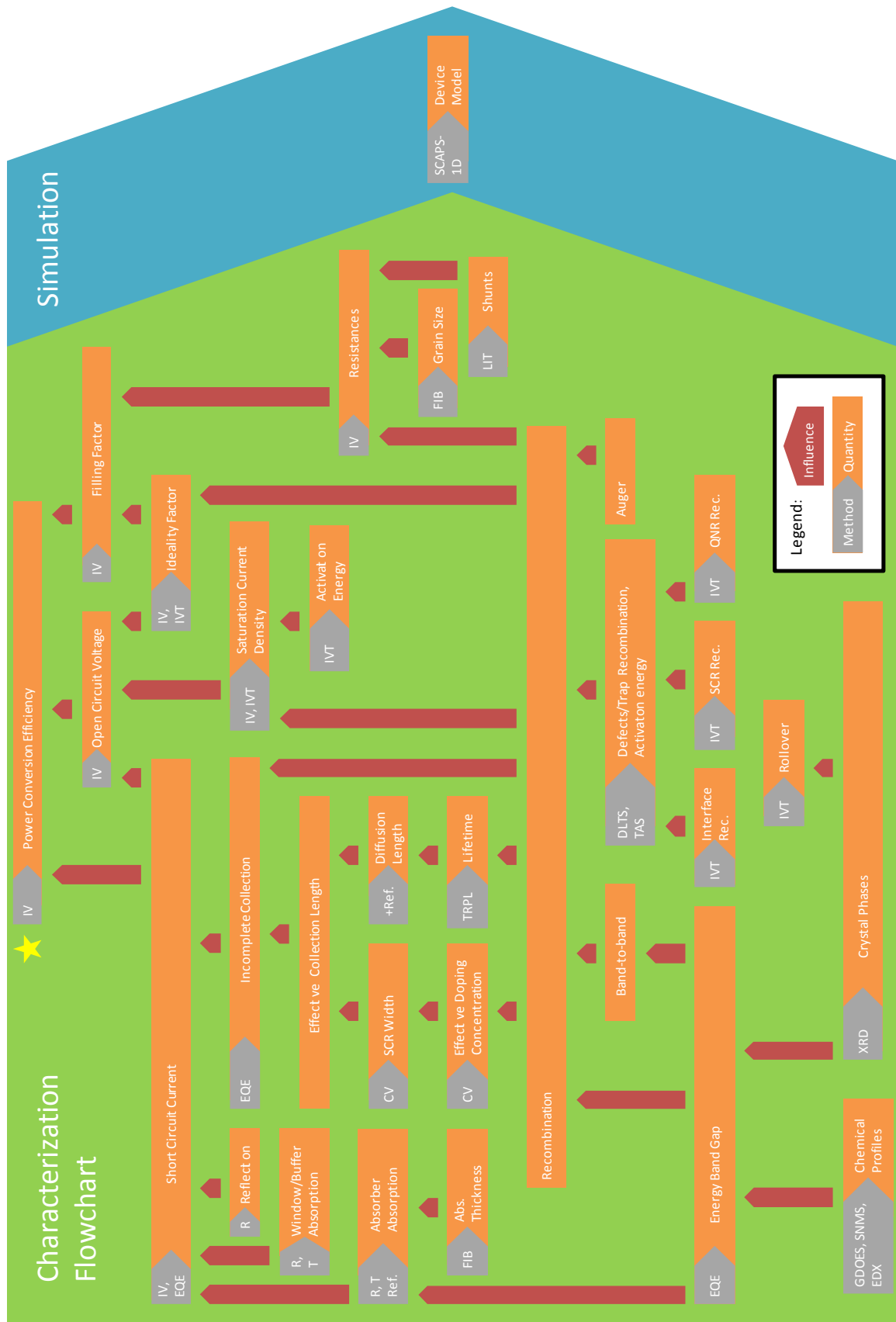
Figure 2.7: Characterization flowchart visualizing device parameter and material properties, interdependencies and characterization methods suited for refining the understanding of particular quantities.

Figure 2.7 displays the characterization flow chart, visualizing how the macroscopic cell parameters (positioned towards the top) are determined by the material properties of the device (positioned towards the bottom). Characterization methods suited to determine the cell parameters and material properties are given such that the next steps necessary to narrow down the responsible loss mechanism can be easily identified. All experimentally determined cell parameters and material characteristics in the green area might be input into the simulation tool for advanced device optimization.

The characterization procedure begins with the assessment of the power conversion efficiency as the most basic but also the most important device quality parameter for comparison of photovoltaic devices. This parameter is extracted from current voltage measurements under standard test conditions but can actually be described by more specific cell parameters (e.g. open circuit voltage, short circuit current). The limiting cell parameter(s) should be identified by comparison of the measurement data with some reference, for example, from a process variation or from the literature. Using Figure 2.7 the cell parameters/material properties which influence a quantity can be identified by tracking the vertical arrows to their base. The measurement and assessment of these more fundamental quantities provide a clearer picture about the nature of the responsible loss mechanisms. Ideally this process is repeated until the elementary origin of the loss mechanism is determined and by extension the processing step is identified which gave rise to its occurrence. Based upon this, the knowledge about the processing might be improved which could result in better devices and a more reproducible production output.

The characterization procedure displayed in Figure 2.7 is far from exhaustive and might not identify the loss mechanisms in every device. In this case the procedure should be enhanced by suitable characterization methods. However, this is not always applicable as some elementary characteristics might not be measurable. The influence of those inaccessible parameters could be investigated with suitable simulation programs by setting up a reasonable simulation baseline including all the experimentally determined quantities.

All samples were initially examined in a basic characterization consisting of quantum efficiency, current-voltage and capacitance voltage measurements to categorize the loss mechanisms in the device into optical, ohmic and recombinatoric loss mechanisms. With these results the subsequent more advanced methods are determined.

2.3.2 Electrical characterization

External quantum efficiency

The external quantum efficiency $EQE = \#e^-_{out} / \#\gamma_{in}$ is defined by the number of extracted electrons per unit time and unit area $\#e^-_{out}$ relative to the number of incoming photons per unit time and unit area $\#\gamma_{in}$. It is a measure for the ability of a photovoltaic device to absorb photons, generate charge carriers, separate them and finally collect them as current J at the external contacts. These processes depend on the photon energy $E = hc/\lambda$, where h is Planck's constant, c is the speed of light and λ is the wavelength of the light. By studying $EQE(E)$ several loss mechanisms can be identified (Figure 2.8a) [112]. The EQE is independent of the
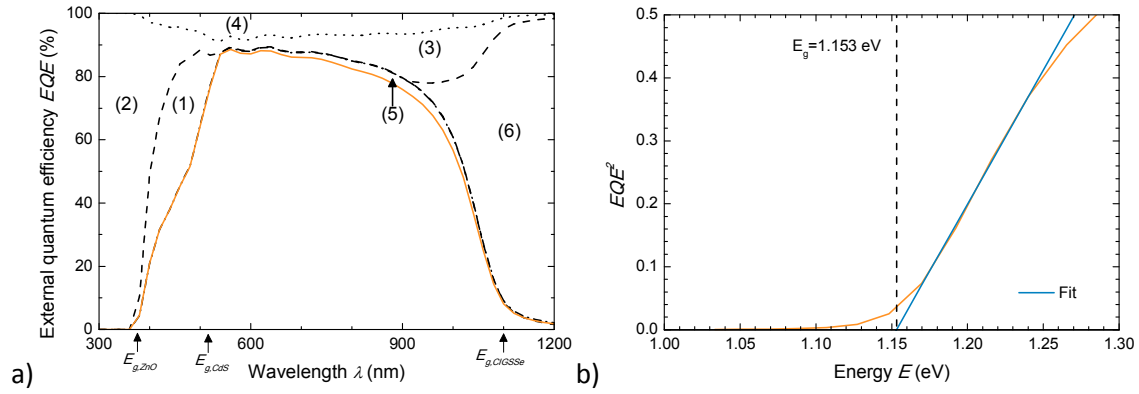
Figure 2.8: a) External quantum efficiency spectrum. Several loss mechanisms reduce the EQE in the marked regions. Refer to the text for further explanations. b) Estimation of the minimal bandgap via a linear fit

illumination spectrum and using a light source with known power density $P_L(E) = \# \gamma_{in}(E) \times E$ the number of extracted electrons is determined by measuring the short circuit current density $J_{SC}(E) = q \times \# e^-_{out}(E)$ for each value on the energy scale by means of dispersing the illumination spectrum with a monochromator.

The photocurrent of the device under an arbitrary illumination spectrum $P_L(E)$ is then calculated according to [44]:

$$J_{SC} = q \int \frac{1}{E} EQE(E) P_L(E) dE \qquad (2.3)$$

Assuming a linear behavior of the absorption $\alpha(E) \propto \sqrt{E - E_g}$ close to the absorption edge E_g in the direct semiconductor [44] as well as $EQE(E) \propto \alpha(E)$, the minimum bandgap $E_{g,min}$ can be estimated by a linear fit of the low energy edge of EQE^2(E) (see Figure 2.8b). However, it must be considered that the high wavelength region is potentially influenced by several loss mechanisms thereby introducing additional errors to this method.

The short circuit current density is reduced by the loss mechanisms marked in Figure 2.8a:

(1) CdS band-to-band absorption: Photons with energy $E > E_g^{CdS}$ which corresponds to a wavelength about 515 nm are absorbed in the buffer layer and do not reach the absorber. Charge carriers generated in the buffer layer are assumingly not collected and recombine, therefore the current loss scales proportionally with the CdS thickness [31].

(2) ZnO band-to-band absorption: Photons with energy $E > E_g^{ZnO}$ which corresponds to a wavelength about 375 nm are absorbed in the TCO and do not reach the absorber. The generated charge carriers are lost by recombination.

(3) ZnO free carrier absorption: This loss mechanism in highly doped materials is discussed in more detail in section 2.3.6

(4) Reflection losses: without anti-reflective coating these losses amount to about 10% and are determined using an integrating sphere in a UV-Vis spectrometer.

(5) Transport losses: Photons with higher wavelength penetrate deeper into the absorber bulk. The electrons generated within one diffusion length L_D from the depletion region edge are

collected. Charge carriers generated outside the effective collection region $L_D + W_{SCR}$, where W_{SCR} denotes the width of the depletion region, will eventually recombine. According to the Einstein relation L_D depends on the charge carrier lifetime τ which is determined by the recombination kinetics in the bulk.

(6) Incomplete absorption: In too thin absorbers only a fraction of the high wavelength photons will be absorbed. The rest is transmitted, as are photons with energy $E < E_g^{CIGSSe}$ for which the absorber is transparent [15]. The slope of the EQE spectrum in the infrared region is influenced by bandgap gradings [31].

Current-voltage measurements

In $Cu(In,Ga)(Se,S)_2$ solar cells the intrinsic asymmetry required for photovoltaic power generation [4] is implemented via a pn-junction. In the dark the current J_{dark} of such a device at voltage bias V is described by Shockley's diode equation:

$$J_{dark}(V) = J_0 exp\left(\frac{qV}{AkT} - 1\right),$$ (2.4)

where J_0 denotes the saturation current density, A the ideality factor, k the Boltzmann constant and T the cell temperature. The dark current $J_{dark} = J_{diff} + J_{rec}$ includes contributions of the diffusion current J_{diff} and the recombination current J_{rec} which are of the same general mathematical form as equation (2.4). For demonstration purposes the recombination current is here assumed to originate only from Shockley-Read-Hall recombination in the SCR:

$$J_{diff}(V) \propto n_i^2 \left[\exp\left(\frac{qV}{kT}\right) - 1 \right]$$ (2.5)

$$J_{SCR}(V) \propto n_i \left[\exp\left(\frac{qV}{2kT}\right) - 1 \right]$$ (2.6)

Note that both contributions differ in their dependency on the intrinsic carrier concentration n_i which is responsible for their different temperature behavior as will be discussed later. If neither J_{diff} nor J_{rec} are dominating, then J_0 and A in equation (2.4) should be viewed just as auxiliary quantities to describe the current-voltage behavior. However, if one process is dominating, then J_0 and A in equation (2.4) approximate the corresponding values of the dominating contribution. Therefore valuable information can be obtained about the dominating contribution to the dark current in the device by analysis of J_0 and A. Yet, it should be noted, that it is a great simplification to consider only J_{diff} and J_{SCR}. However, it is beyond the scope of this thesis to discuss all possible recombination channels in chalcopyrite thin-film devices. Refer to [5] for a comprehensive discussion of many recombination channels (e.g. recombination in the quasi neutral region/space charge region/interfaces via band-to-band, discrete or distributed recombination centers and considering further effects like tunneling assisted recombination or Fermi-level pinning).

The non-ideal behavior of an illuminated thin-film photovoltaic device generating a photocurrent J_{SC} can be described by equation (2.7) which takes into account the effect of a series resistance R and shunt conductance G [112]:

$$J(V) = J_0 exp\left[\frac{q}{AkT}(V - RJ)\right] + GV - J_{SC} \qquad (2.7)$$

Figure 2.9a shows the typical current-voltage behavior of the investigated solar cells. In the following the performance parameters which can be determined from this characteristic are briefly discussed. In order to extract the diode parameters J_0 and A the JV characteristic is corrected to adjust for influences from the series and shunt resistance according to the procedure described in [112] (see Figure 2.9b). The photocurrent J_{SC} corresponds to the short circuit current as calculated from the EQE and as such is a measure for the ability to extract charge under a given spectrum. At the open circuit voltage V_{OC} the dark current fully compensates the photocurrent:

$$V_{OC} = \frac{AkT}{q} \ln\left(\frac{J_{SC}}{J_0}\right) \qquad (2.8)$$

At the maximum power point (mpp) the device delivers the largest power output $P = VJ$ which is larger the closer V_{mpp} is to V_{OC} and J_{mpp} is to J_{SC}, in other words the degree of "squareness" of the JV characteristic. This is summarized in the fill factor $FF = J_{mpp}V_{mpp}/J_{SC}V_{OC}$. The power conversion efficiency η of the photovoltaic device is consequently defined as $\eta = \frac{FF\, J_{SC}\, V_{OC}}{P_L}$ [44].

In order to approximate the standard test conditions (STC: cell temperature: 25 °C, Air Mass 1.5g standard spectrum with an integrated illumination intensity 1000 W/m^2 [113]) in the laboratory further aspects have to be considered. The intensity of the solar simulator is adjusted using a calibrated (Fraunhofer ISE) reference Si cell. In order to account for the different EQE of the reference cell (ref) and the device under test (DUT) as well as differences of the standard spectrum (AM1.5g) to the actual spectrum delivered by the solar simulator (SolSim) the spectral mismatch factor M is calculated: [114]

$$M = \frac{J_{SC,ref}^{AM1.5g}}{J_{SC,ref}^{SolSim}} \frac{J_{SC,DUT}^{SolSim}}{J_{SC,DUT}^{AM1.5g}} \qquad (2.9)$$
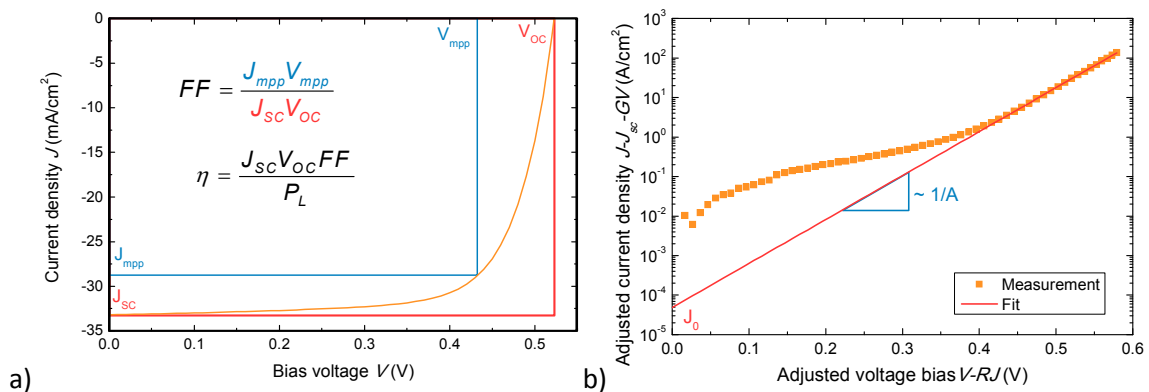
Figure 2.9: a) typical JV characteristic of a solar cell b) same JV characteristic corrected by R and G in a semilogarithmic prestentation

18
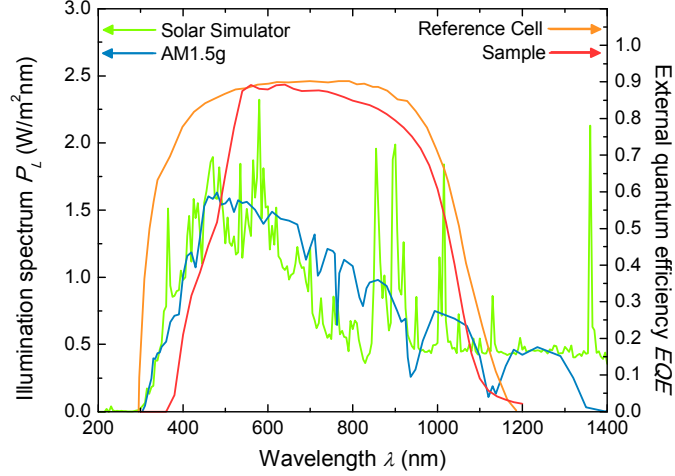
Figure 2.10: Comparison of the standard AM1.5 and the solar simulator spectrum as well as the quantum efficiencies of the Si-reference cell and a CIGSSe sample

From equation (2.9) follows that the measured $J_{SC,DUT}^{SolSim}$ corresponds only to the desired $J_{SC,DUT}^{AM1.5g}$, if the light intensity is set such that $J_{SC,ref}^{SolSim} = J_{SC,ref}^{AM1.5g}/M$. The solar simulator spectrum measured with a spectrometer is shown in Figure 2.10. The actually measured currents I were normalized to an active area of 1 cm^2. The active area of the photovoltaic cells was determined using a high resolution camera.

Temperature dependent current-voltage measurements

In the previous section the different dependency of equations (2.5) and (2.6) on the intrinsic carrier concentration was already mentioned. According to the Boltzmann approximation this bias independent material property is thermally activated:

$$n_i^2 \propto \exp\left(-E_g/kT\right) \tag{2.10}$$

Therefore, the temperature behavior of the saturation current density can be written in the general form:

$$J_0 = J_{00}\exp\left(-\frac{E_a}{AkT}\right) \tag{2.11}$$

with the weakly temperature-dependent reference current density J_{00}, and the activation energy E_a which differs for the various recombination channels [5]. The type and location of the most dominant recombination channel might be identified by the determination of E_a and $A(T)$ which motivates temperature dependent current voltage measurements (IVT) [115]. An alternative method to determine A and J_0 at a certain temperature which avoids the influence of the series resistance is to plot $\ln(J_{SC})$ against V_{OC} for different illumination intensities [115,116]:

$$\ln J_{SC} = \frac{q}{AkT}\cdot V_{OC} + \ln J_0 \tag{2.12}$$

Combining equations (2.11) and (2.8) gives a method to determine the activation energy of the saturation current from the intercept of $V_{OC}(T)$:

$$V_{OC} = \frac{E_a}{q} - \frac{AkT}{q} \ln\left(\frac{J_{00}}{J_{SC}}\right) \tag{2.13}$$

However, if a distribution of recombination centers is present or the tunnel effect must be considered in the description of the dominating recombination channel, this method is not applicable [115,117]. In this case A has to be corrected for the temperature-dependent contributions and E_a can be determined according to equation (2.11) from the slope of an Arrhenius plot.

2.3.3 Capacitative methods

The significance of the space charge region width W_{SCR} for charge carrier collection has been mentioned in the previous section. With a few assumptions it can be determined from capacitance-voltage (CV) measurements. The n-type window layer is more highly doped than the p-type absorber (n$^+$p junction) motivating the assumption that the depletion region extends only within the absorber for a distance equal W_{SCR} [118]. The SCR is further assumed to be fully depleted, therefore the SCR can be approximated by a parallel plate capacitor $C = \varepsilon/W_{SCR}$. The dielectric constant $\varepsilon = 13.6\varepsilon_0$ was obtained from the literature [119], ε_0 denotes vacuum permittivity. The device is modeled by a parallel RC circuit [120] in which the ac-current generated by an alternating small voltage bias $V = V_0\cos(\omega t)$ with excitation frequency ω is described using the complex admittance Y: $I = YV = (R^{-1} + i\omega C)V$. By measuring the resistance R and the phase shift $\theta = \arctan(1/\omega CR)$ the capacitance and therefore the depletion width can be calculated. The application of a bias voltage V causes an oscillation of the SCR width as:

$$W_{SCR} = \sqrt{\frac{2\varepsilon\varepsilon_0\left(V_{bi} - V\right)}{N_{d,eff}}} \tag{2.14}$$

where V_{bi} is the built-in voltage and $N_{d,eff}$ the effective doping concentration. According to equation (2.15) $N_{d,eff}$ can be profiled using a bias sweep as shown in Figure 2.11a [112]:

$$N_{d,eff}(W) = C^3\left[q\varepsilon\frac{dC}{dV}\right]^{-1} \tag{2.15}$$
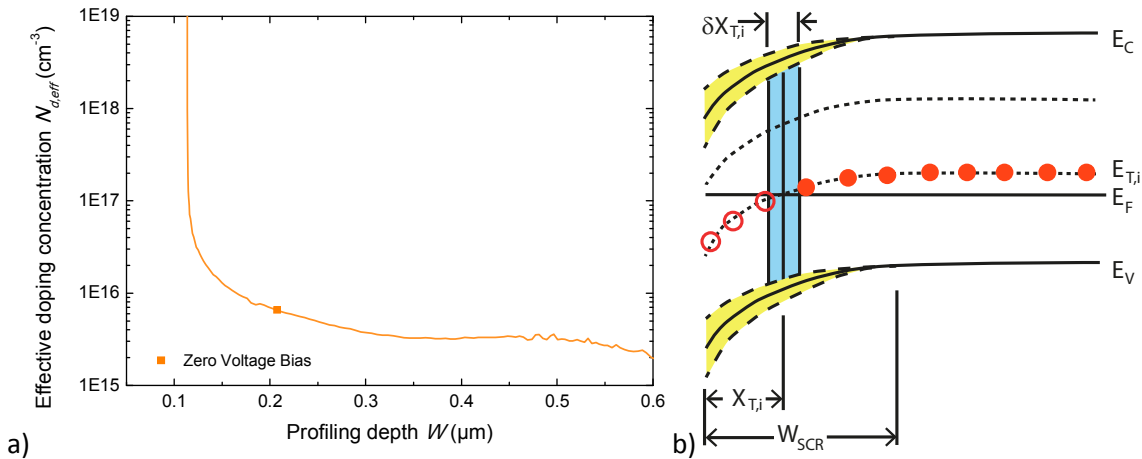
Figure 2.11: a) Example of a profile of the effective doping concentration, the width of the space charge region is marked (■) b) the influence of charge carrier traps on capacitative measurement methods.

20

While some authors interpret the increase towards the heterojunction as real increase in defect concentration [121], other authors note that these values have to be treated carefully as they are determined with a large forward bias applied [20]. In order to avoid the influence of charge state transitions of defects within the energy gap on the capacitance the excitation frequency ω needs to be reasonably high [118]. By keeping the bias voltage constant and sweeping the excitation frequency instead (admittance spectroscopy) these defects can be accessed.

In Figure 2.11b a defect i with energy $E_{T,i}$ is introduced within the energy gap. At distance $x_{T,i}$ from the heterojunction it crosses the Fermi level E_F, i.e. all defects of this type within distance $x_{T,i}$ are filled. The capture and emission of charge carriers via these defects is described by Shockley-Read-Hall theory. By application of the principle of detailed balance the emission rate is given by

$$e_{n/p} = \underbrace{N_{C/V} v_{th} \sigma_{n/p}}_{T^2 \xi_0} \exp\left(\frac{-\left|E_{T,i} - E_{C/V}\right|}{kT}\right). \tag{2.16}$$

Where $\sigma_{n/p}$ is the capture cross section, $N_{C/V}$ and $E_{C/V}$ is the effective density of states resp. the energy level of the conduction/valence bands and v_{th} the thermal velocity. The exponential coefficient contains a T^2 dependency and the temperature-independent contribution is labeled ξ_0. The charge state of the defects directly at $x_{T,i}$ is determined by the excitation frequency ω. If $e_{nlp} > \omega$, then the emission from these defects follow the excitation and the distance until all defects are charged oscillates about $\delta x_{T,i}$, which can be detected as change in the admittance. However, if $e_{n/p} < \omega$, then the defects cannot follow the excitation oscillation anymore and they are deactivated. Consequently at $\omega = e_{n/p}$ a capacitance step will occur which enables the determination of $e_{n/p}$ from equation (2.17):

$$e_{n/p} = -\omega \frac{dC}{d\omega}\bigg|_{\max} \tag{2.17}$$

According to equation (2.16) the emission rate is thermally activated with a transition energy $E_{a,i} = |E_{T,i} - E_{C/V}|$ corresponding to their distance to one of the band edges. By performing admittance spectroscopy at different temperatures (TAS) and considering the T^2 dependency the transition energy can be determined from the slope of an Arrhenius plot:

$$\ln\left(\frac{e_{n/p}}{T^2}\right) = \frac{E_{a,i}}{k}\frac{1}{T} + \ln \xi_0 \tag{2.18}$$

As this method requires that the Fermi level is crossed by the defect, mainly majority defects are detected. Minority defects are only accessible when a strong type inversion and large concentration of the particular defect is present. The deeper the defect, the more the sensitivity is reduced as lower emission rates require low oscillation frequencies [122]. Deep-level transient spectroscopy (DLTS) is an alternative defect spectroscopic method and more suitable to detect deep traps. Keeping the sample at reverse bias V_r the defects are all depleted and the junction capacitance is C_0. Then a forward bias pulse V_f is applied which fills all defects until at time $t = 0$ the sample is kept at reverse bias once again. The trapped charges in the defects relax over time

resulting in a transient change of the capacitance $\Delta C(t) = C(t) - C_0$ which depends on the emission rate and the density of occupied traps $N_{T,i}$ right after the pulse [118]. If $V_f < V_r$ mainly majority traps are detected (Majority-DLTS), however, by applying $V_f > V_r$ also the minority carrier traps are charged during the filling pulse and can be detected as well (Minority-DLTS)

$$\frac{\Delta C(t)}{C_0} = \mp \frac{N_{T,i}}{2 N_{d,eff}} \exp(-e_{p/n} t) \qquad (2.19)$$

As the space charge region width decreases if minority carrier traps are charged the sign of the transient is positive, and vice versa for majority carriers. The emission rate is extracted from these transients by application of a lock-in filter and the density of the occupied defects can be calculated from $\Delta C(0)$. Longer emission rates can be detected by extending the recording time of the transient. Therefore DLTS avoids the shortcomings of TAS as it is able to detect deep traps in the energy gap and to differentiate between charge types.
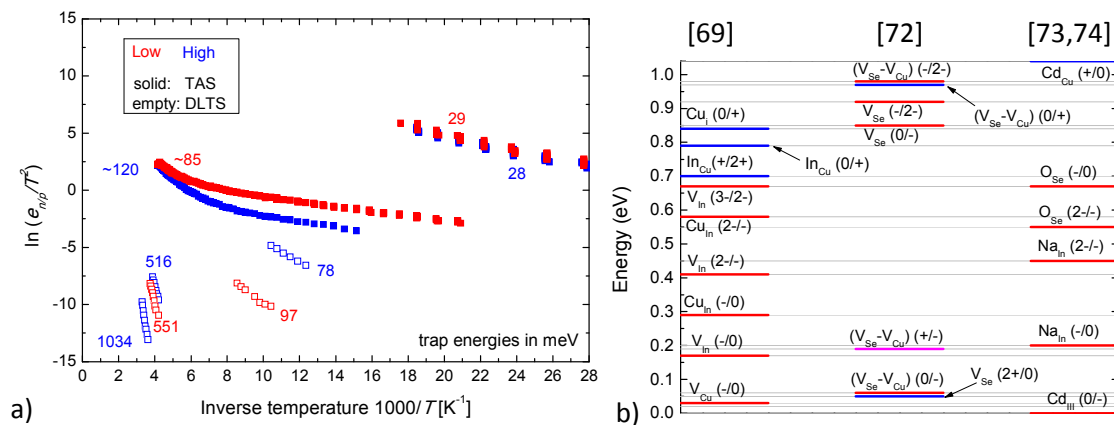
Figure 2.12: a) Arrhenius-Plot of the emission rates of the samples discussed in chapter 5 b) Defect levels for CuInSe$_2$ (including the charge state) as calculated in the given references. The grey lines were added for better orientation.

In Figure 2.12a the emission rates of the samples investigated in chapter 5 as determined from TAS and DLTS are shown in an Arrhenius plot. The activation energies were extracted by a linear fit according to equation (2.18) and are given for the detected levels. Figure 2.12b shows the positions of defect levels which were obtained from calculations [69,72–74]. This allows the identification of the detected defects. A special admittance signal named N1 is the most prominent and widely discussed capacitance signal and its origin is not yet fully understood [20,121,123]. Since N1 could potentially be caused by a back contact diode [20,124] or hopping conduction [123], it is not even verified that N1 is a defect at all.

2.3.4 Structural and compositional characterization

In chapter 2.2 the importance of the distribution of elements in the chemical profiles has been explained. Even though deposition parameters like elemental fluxes and the temperature of the atmosphere are known the corresponding chemical composition as well as the desired crystal phases are not necessarily represented in the absorber. Furthermore slight variations in the process conditions might lead to different growth conditions, inhomogeneities and formation of structural imperfections. Therefore the internal structure of the actual device under investigation should be examined in parallel to the electric characterization.
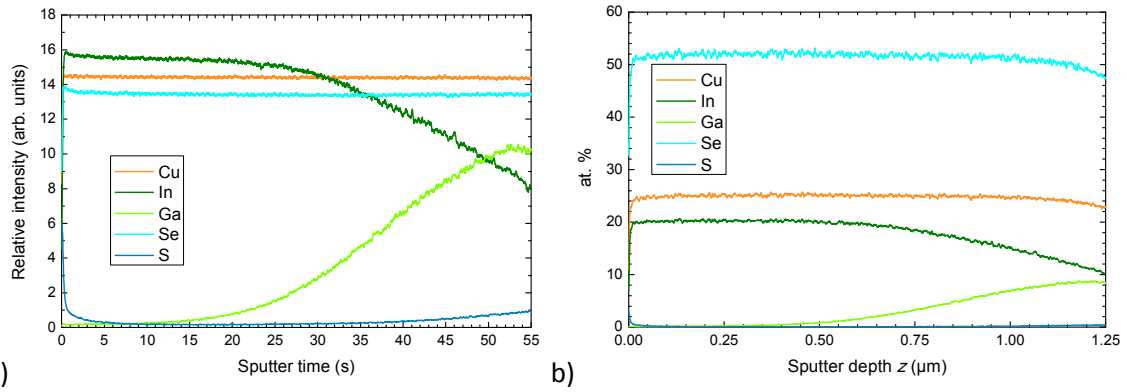
Figure 2.13: a) From the intensity signals for each element measured over time b) the relative atomic concentrations at different locations in the absorber can be calculated

A first visual assessment of the layer parameters can be performed by scanning electron microscopy (SEM) [125]. Depending on the sample preparation structural information of different quality can be obtained. The first method is breaking the device cleanly and scanning along the whole sample edge. This allows assessing the thickness and roughness of the different layers over a large cross section of the device. Using this method grain sizes can be estimated which might indicate phase separations, since more Ga-rich phases form smaller grains. However, the rough preparation might induce structural deformations and introduce additional errors. The second method is the preparation of clean cross sections by focused ion beam (FIB) milling (see Figure 2.3a). While the grains are no longer distinguishable, the layer thickness can be determined much more accurately. Even though, it must be considered that these values are only accurate on a small lateral length scale since FIB milling on larger scales is impractical due to the duration of this method.

Using glow discharge optical emission spectroscopy (GDOES), chemical depth profiles can be measured with a resolution depth of about 5-10% very quickly in about 3 minutes for a layer with a thickness of 2 μm [126]. In a noble gas atmosphere the sample which acts as a cathode is brought into short distance of the anode in order to sputter ions from the sample. The number of all atoms N sputtered within unit time Δt is denoted by the sputter rate $q = N/\Delta t$ and the relative concentration of element species i among those sputtered atoms by $c_i = N_i/N$, where N_i is the number of ions of element i in the plasma. The relaxing ions emit spectral lines characteristic for each element which are amplified with photomultipliers. At wavelengths characteristic to each ion dedicated detectors receive the light intensity I_i which is quantified by the assumption of constant emission yield [127], that is, the light intensity emitted per single ion of a specific species can be described by a constant R_i. Consequently, by measuring the light intensity the number of ions of a specific element sputtered during Δt can be quantified according to equation (2.20). However, a careful calibration of the constant R_i is necessary, which is of higher quality the closer the reference material is to the investigated sample:

$$N_i \, / \, \Delta t = qc_i = I_i \, / \, R_i \tag{2.20}$$

With $N = \Sigma N_i$ the relative concentrations and the sputter rate can be calculated. The volume ablated during Δt is given by $V = A\Delta z$ where A is the sputter area and Δz the change in sputter depth. Assuming that the average compound concentration is described by $\rho = \Sigma c_i \rho_i$ where ρ_i

is the specific pure element concentration, the volume can be calculated by $V = N/\rho$. Therefore the change in sputter depth is given by [126]:

$$\Delta z = \sum \frac{q}{\rho A} \Delta t \qquad (2.21)$$

The sputter crater is ideally flat. However, progressive sputtering of samples with rough surfaces preserves the topology during continuous ablation of the sample material. Hence, good spatial resolution and profiling of internal interfaces are only possible if the sample exhibits planar surfaces.

While GDOES gives information about elemental distributions, it does not reveal if or how the elements are integrated into a crystal structure. With x-ray diffraction spectroscopy the crystal phases and to a certain extent their composition ratios can be determined which is used in chapter 4 to extract the mixing ratio $y = [S]/([S]+[Se])$ of $CuIn(S,Se)_2$. Only if the Bragg condition is fulfilled which depends on the interlattice distance d, the monochromatic light is reflected from lattice planes described by the Miller indices (hkl) [128]. For tetragonal unit cells as in CIGSSe the interlattice distance d can be calculated if unit cell dimensions are known with:

$$\frac{1}{d^2} = \frac{h^2 + k^2}{a^2} + \frac{l^2}{c^2} \qquad (2.22)$$

However, it is impossible to determine x and y from the interlattice distance since according to equation (2.1) the unit cell dimensions scale independently with x as well as y. Yet, in chapter 4 this method is applied for the analysis of the Ga-depleted phase which had formed due to the segregation process described in chapter 2.2.2. As CIGSSe obeys Vegard's law and it is assumed $x = 0$ y can be easily determined [55,129,130]. A total replacement of Se

Crystal	CuInSe$_2$	CuInS$_2$
a (Å)	5.78	5.52
c (Å)	11.62	11.13
2θ (°)	26.59	27.89

Table 2.2: Unit cell dimensions and first order reflection angles of the (112) peak in $CuIn(S,Se)_2$ for under monochromatic radiation with λ(Cu Kα) = 1.541 Å

by S results only in a shift of little more than 1° (see Table 2.2). A common error which causes a shift of the XRD patterns is the sample displacement. Since already small inaccuracies in the determination of the peak position will lead to substantial errors in the determination of y the height displacement correction is performed. The sample displacement s causes a shift $\Delta 2\theta$ (rad) in the 2θ-plot which depends on the cosine of the actual detection angle θ, with R being the goniometer radius.

$$\Delta 2\theta = \frac{2s \cos \theta}{R} \qquad (2.23)$$

Since s is unknown it is determined with a reference peak. The position of the Mo (100) peak is well known and by determining the Mo (100) shift $\Delta 2\theta$ at diffraction angle θ the sample displacement can be calculated.

Using the grazing incidence (GI) mode of XRD the x-ray penetrates the absorber only close to the surface. By varying the GI angle ω the penetration depth changes [28] and the homogeneity of the crystal with thickness can be examined. A phase segregation between a Ga-rich and Ga-
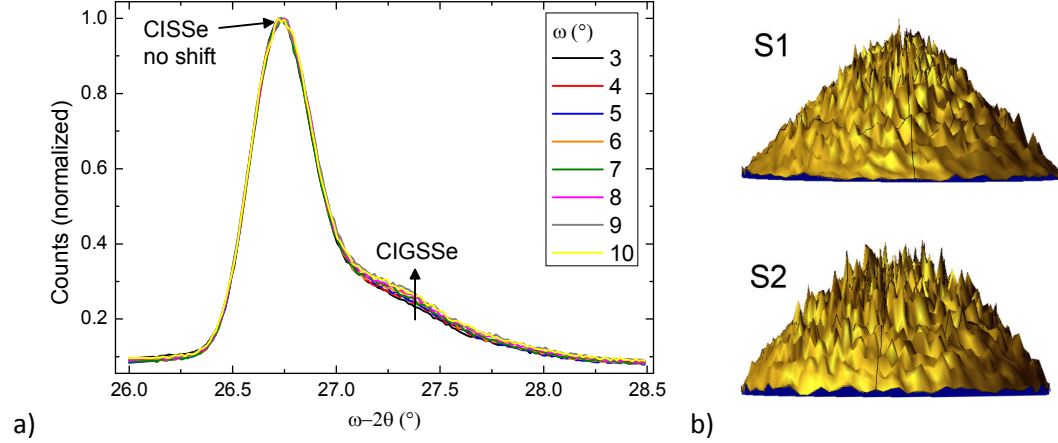
Figure 2.14: a) Grazing Incidence XRD in a sample prepared by the sequential process showing a phase separation between a CuIn(S,Se)$_2$ phase at the absorber surface and a CIGSSe phase towards the back contact b) 2.5 dimensional presentation of the MoSe$_2$ (100) peak in Texture XRD measurements for two samples investigated in chapter 4.

depleted phase shows in the increase of the Ga-rich CIGSSe peak with increasing ω (Figure 2.14a). The XRD spectra also reveal the presence of phases like MoSe$_2$ in some samples of the investigations in chapter 4. The texture mode of XRD detects the changes of the reflection intensities at a fixed angle for different incidence directions which provides information about the presence of preferred crystal orientations. This was applied in order to detect growth differences of the differently thick MoSe$_2$ layers but only small differences are suggested in the very amorphous signals (Figure 2.14b).

2.3.5 Transient Photoluminescence

Observed losses from incomplete charge carrier collection do not only depend on W_{SCR} but also on the diffusion length L_D as seen in section 2.3.2. The diffusion length relates to the minority carrier lifetime τ_n via the Einstein relation $L_D = \sqrt{D\tau_n}$ where D is the diffusion constant of electrons in the material. The diffusion constant was reported to be constant for CIGSSe and about $D \sim 1\,\mathrm{cm}^2/\mathrm{s}$ [131]. The minority carrier lifetime is tracked by the time-resolved photoluminescence (TRPL) of the semiconducting absorber. Time-correlated single photon counting (TCSPC) is a suitable method to measure TRPL decay curves [132]. Using a fast laser an excess electron concentration Δn is injected into the absorber. After the light pulse the carrier ensemble undergoes radiative and non-radiative recombination. Under low-injection conditions, i.e. $\Delta n < N_d$, the luminescence signal emitted by radiative recombination processes is proportional to Δn [133]. Therefore the decay of the photoluminescence correlates with the lifetime of the excess electrons in the absorber. Photoluminescence decay curves reported in the literature are mostly fit with a biexponential function:

$$PL(t) = A_1 e^{-t/\tau_1} + A_2 e^{-t/\tau_2} \quad, \tag{2.24}$$

with A_1 and A_2 the exponential coefficients and τ_1 and τ_2 the time constants. Different recombination rates in the bulk or at interfaces via different recombination mechanisms (radiative, Shockley-Read-Hall, Auger, etc.) can cause non-exponential decays with different decay time constants [134]. Therefore it is difficult to assign the observed decays to a specific recombination channel. The order of magnitude of reported time constants varies for the short

$$PL(t) = A_1 e^{-t/\tau_1} + A_2 e^{-t/\tau_2}$$
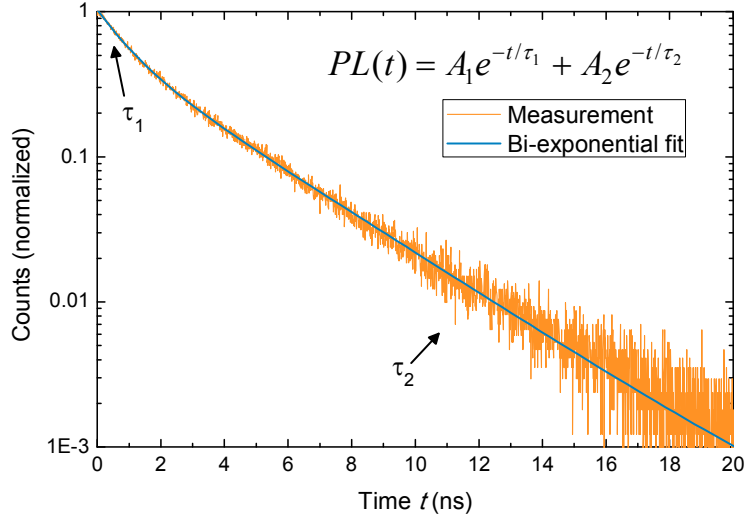
Figure 2.15: Transient photoluminescence of a CIGSSe solar cell.

time constant τ_1 from hundreds of picoseconds to nanoseconds and for the long time constant τ_2 from hundreds of picoseconds to tens of nanoseconds [132,135–137] and are very sensitive to the exact experimental conditions (e.g., air exposure, laser intensity, measurements on full devices or only the absorber) [138]. Therefore the observed time constants are difficult to assign to the actual minority lifetimes in the device under operating conditions, though relative quality differences of the absorber can be determined. The physical meaning of τ_1 and τ_2 is not yet clarified [139]. Figure 2.15 shows the PL transients of a CIGSSe sample.

2.3.6 Optical characterization

Absorption in the ZnO:Al window layer has a large impact on the optical losses of the solar cell as seen in the quantum efficiency. The absorption spectrum shown in Figure 2.16 which was used for the simulations in chapter 5 was determined from measurements of reflection R and transmittance T of the window layer on glass using equation (2.25). In order to obtain the correct T the measured transmittance T_{meas} is corrected by adding the glass absorbance $A_g = 1 - R_g - T_g$ which was determined in reference measurements of the glass only.

$$\alpha = -\frac{1}{d} \ln\left(\frac{1-T}{R}\right) \tag{2.25}$$

The conductive transparent oxide not only removes photons with energies larger than $E_g = 3.3$ eV from the spectrum but the high density of charge carriers leads to free carrier absorption which is seen in the increase above 550 nm [140]. An electromagnetic wave causes in highly doped semiconductors a plasmonic oscillation of the electron gas with a characteristic frequency which depends on the charge carrier density. This counter acts the desire to dope the TCO as highly as possible in order to decrease transport losses.

The absorption of CIGS was attempted to calculate in a similar way. Window and buffer layers were removed by etching and the absorber lifted-off the metallic back contact to achieve a pure absorber layer on a transparent substrate. Due to the high absorption coefficient of the chalcopyrite the transmission was negligible and the obtained absorption spectra highly questionable. Therefore literature values measured by ellipsometry [141,142] were employed and interpolated for the local GGI in the investigated samples.
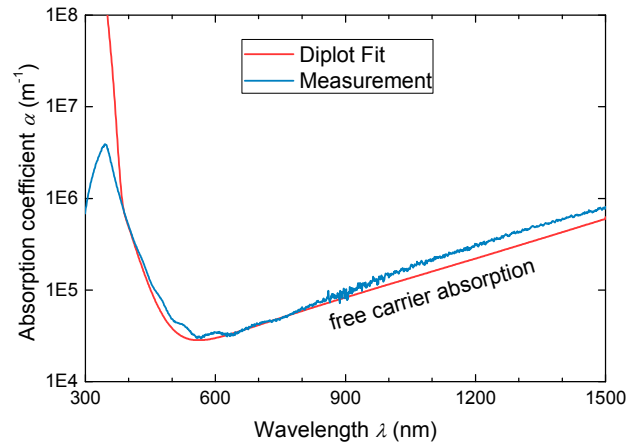
Figure 2.16: Absorption spectrum of the ZnO:Al window layer. The fit was realized with the simulation program Diplot and includes contributions from the Drude model of free carrier absorption.

2.3.7   Simulation

Device simulations are a valuable tool to reconstruct loss processes in the device structure. Using well calibrated device models, simulations may pinpoint optimization strategies (e.g. by changing physical properties of the functional layers or by altering the layer sequence of the device). These can be evaluated quickly and inexpensively without the need for manufacturing of devices incorporating the parameter variations under investigation, and their subsequent extensive and time-consuming experimental characterization.

However, the choice of the used simulation tool is vital to the extent, accuracy and speed of the calculations. In chapter 5, the one dimensional simulation program SCAPS-1D is used which was and is being developed at the University of Gent [143]. Yet, the reduction of the device geometry to one dimension does not represent the only approximation of this program to describe the electronic behavior of the device. Further restrictions are its inability to model transient processes and the lack of an optical solver necessitates that reflection and absorption spectra are provided by optical measurements. Nevertheless, SCAPS-1D is provided to the scientific community without charge, is able to deliver results of calculations within reasonable time, allows for short training periods (compared to considerably more complex commercial alternatives), and as a decisive feature supports the ability to describe the value of almost all material properties as a function of location. This enables the implementation of bandgap gradings as investigated in chapter 5 by specifying the material properties for two endpoints and along the depth coordinate between them SCAPS will interpolate according to a specified function which can be linear or non-linear [144].

In order to achieve reliable results the simulation baseline which is used for optimization needs to be well calibrated. The most trustworthy model uses results from the optical, chemical and electrical characterization as input parameters where possible, though, many parameters which are not experimentally accessible are acquired from literature. In order to emulate the measurements, the simulation program uses fundamental material parameters which are positioned close to the bottom of Figure 2.7. Therefore it is reasonable to calibrate the simulation baseline in a bottom-up approach. The baseline should be calibrated by first emulating those measurements which are influenced by the fundamental parameters. This

reduces the number of parameters to consider initially and will provide a solid starting point for the subsequent calibrations. As an example the initial calibration performed in chapter 5 was to adjust for the external quantum efficiency. As described in section 2.3.2 the EQE spectrum determines J_{SC} under a given illumination. Since J_{SC} is one of the cell parameters extracted from the current-voltage characteristics under illumination, the reliable emulation of J_{SC} provides a fix point in the calibration to the more integral device behavior. In order to create a more robust simulation baseline, the successful simulation of these two measurements is not sufficient. Further calibration is necessary to correctly simulate other measurements which are supported by the simulation program as well (e.g. capacitance-voltage, admittance). From the discussions in the previous sections it is apparent, that not all important cell parameters are determined from measurements at room temperature in the dark or under standard illumination. Using the successful calibration to standard test conditions as a fix point first the behavior of the device under varying light-intensity should be simulated and subsequently adjusted for measurements at different temperature in order to simulate TAS and IVT. However, it was beyond the scope of this thesis to consider any measurements in the calibration other than EQE and STC-IV. Even though, the results in chapter 5 show that reasonable simulations could be achieved just with calibration to these two methods.

The one dimensional device model is made up of several layers and interfaces whose physical properties have to be clearly defined. SCAPS-1D allows the implementation of multiple donor or acceptor levels or surface states with individual charge states and distribution options (e.g. uniform, Gauß, or tail-like distribution). Considering the definition parameters of the model, the incident illumination spectrum and the applied voltage bias, the steady state solution is numerically calculated by solving three coupled differential equations, i.e. the Poisson equation and the continuity equations for electrons and holes respectively using a Gummel iteration algorithm [145]. However, during the analysis of the simulation results the approximations made by the program must be kept in mind. For example as only one dimension is considered, lateral fluctuations of layer composition, thickness or roughness cannot be modeled correctly and the model parameters have to be interpreted as effective physical quantities.

References:

[1]   D.W. Aitken, Transitioning to a Renewable Energy Future, International Solar Energy Society, 2003.

[2]   W.C. Turkenburg, in:, World Energy Assessment: Energy and the Challenge of Sustainability, 2000, pp. 219–272.

[3]   A. Luque, S.S. Hegedus, eds., Handbook of Photovoltaic Science and Engineering, Wiley-VCH, Weinheim, 2003.

[4]   P. Würfel, The Physics of Solar Cells - From Principles to New Concepts, Wiley-VCH, Weinheim, 2005.

[5]   R. Scheer, H.-W. Schock, Chalcogenide Photovoltaics: Physics, Technologies, and Thin Film Devices, Wiley-VCH, Weinheim, 2011.

[6]   M.A. Green, K. Emery, Y. Hishikawa, W. Warta, E.D. Dunlop, Progress in Photovoltaics: Research and Applications 20 (2012) 606–614.

[7]   O. Dreissigacker, http://www.pro-physik.de/details/news/2568801/CIGS_erreicht_erstmals_Wirkungsgrad_von_multikristallinen_Modulen.html (2012) 1.

[8]   C. Brabec, U. Scherf, V. Dyakonov, eds., Organic Photovoltaics - Materials, Device Physics, and Manufacturing Technologies, Wiley-VCH, Weinheim, 2008.

[9]   W. Hoffmann, Solar Energy Materials and Solar Cells 90 (2006) 3285–3311.

[10]   A. Shah, P. Torres, R. Tscharner, N. Wyrsch, H. Keppner, Science 285 (1999) 692–698.

[11]   K. Zweibel, Solar Energy Materials and Solar Cells 59 (1999) 1–18.

[12]   N.G. Dhere, Solar Energy Materials and Solar Cells 91 (2007) 1376–1382.

[13]   M. de Wild-Scholten, in:, Proceedings of the 26th EU PVSEC, 2011, pp. 2009–2012.

[14]   L.L. Kazmerski, M. Hallerdt, P.J. Ireland, R.A. Mickelsen, W.S. Chen, Journal of Vacuum Science & Technology A: Vacuum, Surfaces, and Films 1 (1983) 395–398.

[15]   O. Lundberg, M. Bodegard, J. Malmström, L. Stolt, Progress in Photovoltaics: Research and Applications 11 (2003) 77–88.

[16]   S.B. Zhang, S.-H. Wei, A. Zunger, Physical Review B 57 (1998) 9642–9656.

[17]   W. Shockley, H.J. Queisser, Journal of Applied Physics 32 (1961) 510.

[18]   M. Igalson, M. Cwil, M. Edoff, Thin Solid Films 515 (2007) 6142–6146.

[19] R. Hunger, M.V. Lebedev, K. Sakurai, T. Schulmeyer, T. Mayer, A. Klein, S. Niki, W. Jaegermann, Thin Solid Films 515 (2007) 6112–6118.

[20] T. Eisenbarth, T. Unold, R. Caballero, C.A. Kaufmann, H.-W. Schock, Journal of Applied Physics 107 (2010) 034509.

[21] D. Hariskos, S. Spiering, M. Powalla, Thin Solid Films 480-481 (2005) 99–109.

[22] A.E. Delahoy, L. Chen, M. Akhtar, B. Sang, S. Guo, Solar Energy 77 (2004) 785–793.

[23] K. Orgassa, H.-W. Schock, J.H. Werner, Thin Solid Films 431-432 (2003) 387–391.

[24] B.M. Basol, V.K. Kapur, C.R. Leidholm, A. Halani, in:, Proceedings of the 25th IEEE PVSC, 1996, pp. 157–162.

[25] B. Dimmler, M. Powalla, H.-W. Schock, Progress in Photovoltaics: Research and Applications 10 (2002) 149–157.

[26] M. Powalla, B. Dimmler, Thin Solid Films 361-362 (2000) 540–546.

[27] R. Herberholz, V. Nadenau, U. Rühle, C. Köble, H.-W. Schock, B. Dimmler, Solar Energy Materials and Solar Cells 49 (1997) 227–237.

[28] V. Probst, F. Hergert, B. Walther, R. Thyen, B. Neumann, A. Windeck, T. Letzig, A. Gerlach, in:, Proceedings of the 24th EU PVSEC, 2009, pp. 2455–2459.

[29] U. Rau, T. Kirchartz, A. Helbig, J.H. Werner, R. Schäffler, Photovoltaics International 6 (2009) 110.

[30] T. Dullweber, G. Hanna, U. Rau, H.-W. Schock, Solar Energy Materials and Solar Cells 67 (2001) 145–150.

[31] W.N. Shafarman, L. Stolt, in:, A. Luque, S.S. Hegedus (Eds.), Handbook of Photovoltaic Science and Engineering, Wiley-VCH, Weinheim, 2003, pp. 567–616.

[32] A. Bollero, L. Kaupmees, T. Raadik, M. Grossberg, S. Fernández, Thin Solid Films 520 (2012) 4163–4168.

[33] M. Hartmann, M. Schmidt, A. Jasenek, H.-W. Schock, F. Kessler, K. Herz, M. Powalla, in:, Proceedings of the 28th IEEE PVSC, 2000, pp. 638–641.

[34] M. Bodegard, L. Stolt, J. Hedström, in:, Proceedings of the 12th EU PVSEC, 1994, p. 1743.

[35] V. Probst, J. Rimmasch, W. Riedl, W. Stetter, J. Holz, H. Harms, F.H. Karg, H.-W. Schock, in:, Proceedings of the First WCPEC, 1994, pp. 144–147.

[36] J. Palm, Probst, A. Brummer, W. Stetter, R. Tölle, T.P. Niesen, S. Visbeck, O. Hernandez, M. Wendl, H. Vogt, H. Calwer, B. Freienstein, F.H. Karg, Thin Solid Films 431-432 (2003) 514–522.

[37] R.J. Matson, O. Jamjoum, A.D. Buonaquisti, P.E. Russell, L.L. Kazmerski, P. Sheldon, R.K. Ahrenkiel, Solar Cells 11 (1984) 301–305.

[38] R. Takei, H. Tanino, S.F. Chichibu, H. Nakanishi, Journal of Applied Physics 79 (1996) 2793.

[39] M. Bär, S. Nishiwaki, L. Weinhardt, S. Pookpanratana, W.N. Shafarman, C. Heske, M. Bär, Applied Physics Letters 93 (2008) 042110.

[40] D. Abou-Ras, G. Kostorz, D. Bremaud, M. Kälin, F.V. Kurdesau, A.N. Tiwari, M. Döbeli, Thin Solid Films 480-481 (2005) 433–438.

[41] V.K. Kapur, B.M. Basol, E.S. Tseng, Solar Cells 21 (1987) 65–72.

[42] J. Pouzet, H. Hadouda, J.C. Bernede, R.L. Ny, Journal of Physics and Chemistry of Solids 57 (1996) 1363–1369.

[43] N. Kohara, S. Nishiwaki, Y. Hashimoto, T. Negami, T. Wada, Solar Energy Materials and Solar Cells 67 (2001) 209–215.

[44] J. Nelson, The Physics of Solar Cells, Imperial College Press, 2003.

[45] D. Schmid, M. Ruckh, H.-W. Schock, Solar Energy Materials and Solar Cells 41-42 (1996) 281–294.

[46] M. Rusu, T. Glatzel, A. Neisser, C.A. Kaufmann, S. Sadewasser, M.C. Lux-Steiner, Applied Physics Letters 88 (2006) 143510.

[47] L.C. Olsen, W. Lei, F.W. Addis, W.N. Shafarman, M.A. Contreras, K. Ramanathan, in:, Proceedings of the 26th IEEE PVSC, 1997, pp. 363–366.

[48] R.N. Bhattacharya, W. Batchelor, K. Ramanathan, M.A. Contreras, T. Moriarty, Solar Energy Materials and Solar Cells 63 (2000) 367–374.

[49] K. Kushiya, M. Tachiyuki, T. Kase, I. Sugiyama, Y. Nagoya, D. Okumura, M. Sato, O. Yamase, H. Takeshita, Solar Energy Materials and Solar Cells 49 (1997) 277–283.

[50] T. Nakada, K. Furumi, A. Kunioka, in:, IEEE Transactions on Electron Devices, 1999, pp. 2093–2097.

[51] M. Ruckh, D. Hariskos, U. Ruhle, H.-W. Schock, R. Menner, B. Dimmler, in:, Proceedings of the 25 IEEE PVSC, 1996, pp. 825–828.

[52] U. Rau, M. Schmidt, Thin Solid Films 387 (2001) 141–146.

[53] S. Brehme, F. Fenske, W. Fuhs, E. Nebauer, M. Poschenrieder, B. Selle, I. Sieber, Thin Solid Films 342 (1999) 167–173.

[54] V. Alberts, Materials Science and Engineering: B 107 (2004) 139–147.

[55] L. Vegard, Zeitschrift Für Physik 5 (1921) 17–26.

[56] S.B. Zhang, S.-H. Wei, A. Zunger, Journal of Applied Physics 83 (1998) 3192.

[57] M. Turcu, I.M. Kötschau, U. Rau, Applied Physics A 73 (2001) 769–772.

[58] S.-H. Wei, A. Zunger, Journal of Applied Physics 78 (1995) 3846.

[59] M. Turcu, I.M. Kötschau, U. Rau, Journal of Applied Physics 91 (2002) 1391–1399.

[60] S.-H. Chang, M.-Y. Chiang, C.-C. Chiang, F.-W. Yuan, C.-Y. Chen, B.-C. Chiu, T.-L. Kao, C.-H. Lai, H.-Y. Tuan, Energy & Environmental Science 4 (2011) 4929.

[61] R. Herberholz, U. Rau, H.-W. Schock, T. Haalboom, T. Gödecke, F. Ernst, C. Beilharz, K.W. Benz, D. Cahen, The European Physics Journal - Applied Physics 6 (1999) 131–139.

[62] D. Abou-Ras, R. Caballero, C.A. Kaufmann, M. Nichterwitz, K. Sakurai, S. Schorr, T. Unold, H.-W. Schock, Physica Status Solidi – Rapid Research Letters 2 (2008) 135–137.

[63] G. Hanna, A. Jasenek, U. Rau, H.-W. Schock, Thin Solid Films 387 (2001) 71–73.

[64] J. Palm, V. Probst, F.H. Karg, Solar Energy 77 (2004) 757–765.

[65] W.N. Shafarman, R. Klenk, B.E. McCandless, Journal of Applied Physics 79 (1996) 7324–7328.

[66] V. Probst, W. Stetter, W. Riedl, H. Vogt, M. Wendl, H. Calwer, S. Zweigart, K.-D. Ufert, B. Freienstein, H. Cerva, F.H. Karg, Thin Solid Films 387 (2001) 262–267.

[67] U. Rau, M. Schmitt, F. Engelhardt, O.P. Seifert, J. Parisi, W. Riedl, J. Rimmasch, F.H. Karg, Solid State Communications 107 (1998) 59–63.

[68] T. Nakada, H. Ohbo, M. Fukuda, A. Kunioka, Solar Energy Materials and Solar Cells 49 (1997) 261–267.

[69] S.-H. Wei, S.B. Zhang, A. Zunger, Journal of Applied Physics 85 (1999) 7214.

[70] D. Cahen, R. Noufi, Applied Physics Letters 54 (1989) 558.

[71] T. Nakada, Electronic Materials Letters 8 (2012) 179–185.

[72] S.-H. Wei, S.B. Zhang, A. Zunger, Applied Physics Letters 72 (1998) 3199.

[73] S. Lany, A. Zunger, Journal of Applied Physics 100 (2006) 113725.

[74] C. Persson, Y.-J. Zhao, S. Lany, A. Zunger, Physical Review B 72 (2005) 035211.

[75] H. Neumann, R.D. Tomlinson, Solar Cells 28 (1990) 301–313.

[76] D. Schmid, M. Ruckh, F. Grunwald, H.-W. Schock, Journal of Applied Physics 73 (1993) 2902.

[77] S.B. Zhang, S.-H. Wei, A. Zunger, Physical Review Letters 78 (1997) 4059–4062.

[78]   R. Gay, M. Dietrich, C. Fredric, C. Jensen, K. Knapp, D. Tarrant, D. Willett, in:, R. Hill, W. Palz, P. Helm (Eds.), Proceedings of the 12th EU PVSEC, 1994, p. 935.

[79]   A.M. Gabor, J.R. Tuttle, M.H. Bode, A. Franz, A.L. Tennant, M.A. Contreras, R. Noufi, D.G. Jensen, A.M. Hermann, Solar Energy Materials and Solar Cells 42 (1996) 247–260.

[80]   M. Topič, F. Smole, J. Furlan, Journal of Applied Physics 79 (1996) 8537.

[81]   T. Dullweber, O. Lundberg, J. Malmström, M. Bodegard, L. Stolt, U. Rau, H.-W. Schock, J.H. Werner, Thin Solid Films 387 (2001) 11–13.

[82]   R. Klenk, Thin Solid Films 387 (2001) 135–140.

[83]   T. Wada, N. Kohara, S. Nishiwaki, T. Negami, Thin Solid Films 387 (2001) 118–122.

[84]   N. Naghavi, S. Spiering, M. Powalla, B. Cavana, D. Lincot, Progress in Photovoltaics: Research and Applications 11 (2003) 437–443.

[85]   M. Sahal, B. Marí, M. Mollar, Thin Solid Films 517 (2009) 2202–2204.

[86]   D. Guimard, P.P. Grand, N. Bodereau, P. Cowache, J.-F. Guillemoles, D. Lincot, S. Taunier, M.B. Farah, P. Mogensen, in:, Proceedings of the 29th IEEE PVSC, 2002, pp. 692–695.

[87]   M. Kemell, M. Ritala, M. Leskelä, Critical Reviews in Solid State and Materials Sciences 30 (2005) 1–31.

[88]   M. Powalla, M. Cemernjak, J. Eberhardt, F. Kessler, R. Kniese, H.D. Mohring, B. Dimmler, Solar Energy Materials and Solar Cells 90 (2006) 3158–3164.

[89]   V. Probst, J. Palm, S. Visbeck, T.P. Niesen, R. Tölle, A. Lerchenberger, M. Wendl, H. Vogt, H. Calwer, W. Stetter, F.H. Karg, Solar Energy Materials and Solar Cells 90 (2006) 3115–3123.

[90]   T. Wada, Y. Matsuo, S. Nomura, Y. Nakamura, A. Miyamura, Y. Chiba, A. Yamada, M. Konagai, Physica Status Solidi (a) 203 (2006) 2593–2597.

[91]   A. Knowles, H. Oumous, M. Carter, R. Hill, Semiconductor Science and Technology 3 (1988) 1143–1145.

[92]   J.J.M. Binsma, H.A. Van Der Linden, Thin Solid Films 97 (1982) 237–243.

[93]   N.G. Dhere, S. Kuttath, K.W. Lynn, R.W. Birkmire, W.N. Shafarman, in:, Proceedings of the First WCPEC, 1994, pp. 190–193.

[94]   F.H. Karg, V. Probst, H. Harms, J. Rimmasch, W. Riedl, J. Kotschy, J. Holz, R. Treichler, O. Eibl, A. Mitwalsky, A. Kiendl, in:, Proceedings of the 23rd IEEE PVSC, 1993, pp. 441–446.

[95]   G.D. Mooney, A.M. Hermann, J.R. Tuttle, D.S. Albin, R. Noufi, Applied Physics Letters 58 (1991) 2678.

[96] M. Purwins, A. Weber, P. Berwian, G. Muller, F. Hergert, S. Jost, R. Hock, Journal of Crystal Growth 287 (2006) 408–413.

[97] R. Mainz, R. Klenk, M.C. Lux-Steiner, Thin Solid Films 515 (2007) 5934–5937.

[98] S. Merdes, R. Mainz, H. Rodriguez-Alvarez, J. Klaer, R. Klenk, A. Meeder, H.-W. Schock, M.C. Lux-Steiner, Thin Solid Films 519 (2011) 7189–7192.

[99] F.B. Dejene, M. Sugiyama, H. Nakanishi, V. Alberts, S.F. Chichibu, Physica Status Solidi (c) 3 (2006) 2572–2575.

[100] K. Kushiya, S. Kuriyagawa, T. Kase, M. Tachiyuki, I. Sugiyama, Y. Satoh, M. Satoh, H. Takeshita, in:, Proceedings of the 25 IEEE PVSC, 1996, pp. 989–992.

[101] A.M. Gabor, J.R. Tuttle, D.S. Albin, M.A. Contreras, R. Noufi, A.M. Hermann, Applied Physics Letters 65 (1994) 198.

[102] I.L. Repins, M.A. Contreras, B. Egaas, C. Dehart, J. Scharf, C.L. Perkins, B. To, R. Noufi, Progress in Photovoltaics: Research and Applications 16 (2008) 235–239.

[103] T. Walter, A. Content, K.O. Velthaus, H.-W. Schock, Solar Energy Materials and Solar Cells 26 (1992) 357–368.

[104] W.N. Shafarman, J. Zhu, Thin Solid Films 362 (2000) 473–477.

[105] F.S. Hasoon, Y. Yan, H. Althani, K.M. Jones, H.R. Moutinho, J. Alleman, R. Noufi, Thin Solid Films 387 (2001) 1–5.

[106] K. Ramanathan, M.A. Contreras, C.L. Perkins, S. Asher, F.S. Hasoon, J. Keane, D.L. Young, M.J. Romero, W.K. Metzger, R. Noufi, J.S. Ward, A. Duda, Progress in Photovoltaics: Research and Applications 11 (2003) 225–230.

[107] P. Jackson, D. Hariskos, E. Lotter, S. Paetel, R. Würz, R. Menner, W. Wischmann, M. Powalla, Progress in Photovoltaics: Research and Applications 19 (2011) 894–897.

[108] P.-O. Westin, U. Zimmermann, M. Ruth, M. Edoff, Solar Energy Materials and Solar Cells 95 (2011) 1062–1068.

[109] U. Malm, M. Edoff, Progress in Photovoltaics: Research and Applications 16 (2008) 113–121.

[110] U. Rau, J.H. Werner, Applied Physics Letters 84 (2004) 3735.

[111] L. Gütay, G.H. Bauer, Thin Solid Films 517 (2009) 2222–2225.

[112] S.S. Hegedus, W.N. Shafarman, Progress in Photovoltaics: Research and Applications 12 (2004) 155–176.

[113] ASTM, Standard G173, Standard Tables for Reference Solar Spectral Irradiances: Direct Normal and Hemispherical on 37° Tilted Surface, American Society for Testing and Materials, West Conshocken, PA, USA. (2012).

[114] V. Shrotriya, G. Li, Y. Yao, T. Moriarty, K. Emery, Y. Yang, Advanced Functional Materials 16 (2006) 2016–2023.

[115] U. Rau, H.-W. Schock, Applied Physics A: Materials Science & Processing 69 (1999) 131–147.

[116] T. Walter, R. Menner, C. Köble, H.-W. Schock, in:, R. Hill, W. Palz, P. Helm (Eds.), Proceedings of the 12th EU PVSEC, Stephens, Bedford, 1994, p. 1755.

[117] U. Rau, Applied Physics Letters 74 (1999) 111–113.

[118] J.T. Heath, P. Zabierowski, in:, D. Abou-Ras, T. Kirchartz, U. Rau (Eds.), Advanced Characterization Techniques for Thin Film Solar Cells, Wiley-VCH, Weinheim, 2011, pp. 81–106.

[119] U. Malm, M. Edoff, Solar Energy Materials and Solar Cells 93 (2009) 1066–1069.

[120] V. Mertens, Capacitance Spectroscopy on Copper Indium Diselenide Based Solar Cells, Oldenburg, 1978.

[121] M. Igalson, A. Urbaniak, M. Edoff, Thin Solid Films 517 (2009) 2153–2157.

[122] D.V. Lang, Journal of Applied Physics 45 (1974) 3023.

[123] U. Reislöhner, H. Metzner, C. Ronning, Physical Review Letters 104 (2010) 226403.

[124] J.V. Li, in:, Proceedings of the 37th IEEE PVSC, 2011, p. 75.

[125] D. Abou-Ras, M. Nichterwitz, M.J. Romero, S.S. Schmidt, in:, D. Abou-Ras, T. Kirchartz, U. Rau (Eds.), Advanced Characterization Techniques for Thin Film Solar Cells, Wiley-VCH, Weinheim, 2011, p. 299.

[126] V. Hoffmann, D. Klemm, V. Efimova, C. Venzago, A. Rockett, T. Wirth, T. Nunney, C.A. Kaufmann, R. Caballero, in:, D. Abou-Ras, T. Kirchartz, U. Rau (Eds.), Advanced Characterization Techniques for Thin Film Solar Cells, Wiley-VCH, Weinheim, 2011, p. 411.

[127] A. Bengtson, T. Nelis, Analytical and Bioanalytical Chemistry 385 (2006) 568–585.

[128] S. Schorr, C. Stephan, T. Törndahl, R. Mainz, in:, D. Abou-Ras, T. Kirchartz, U. Rau (Eds.), Advanced Characterization Techniques for Thin Film Solar Cells, Wiley-VCH, Weinheim, 2011, p. 347.

[129] B. Grzeta-Plenkovic, S. Popovic, B. Celustka, B. Santic, Journal of Applied Crystallography 13 (1980) 311–315.

[130] K. Zeaiter, Y. Llinares, C. Llinarès, Solar Energy Materials and Solar Cells 61 (2000) 313.

[131] M. Nishitani, T. Negami, N. Kohara, T. Wada, Journal of Applied Physics 82 (1997) 3572.

[132] B.M. Keyes, P. Dippo, W.K. Metzger, J.A. Abushama, R. Noufi, Journal of Applied Physics 94 (2003) 5584.

[133] W.K. Metzger, I.L. Repins, M.A. Contreras, Applied Physics Letters 93 (2008) 022110.

[134] R. Scheer, A. Pérez-Rodríguez, W.K. Metzger, Progress in Photovoltaics: Research and Applications 18 (2010) 467–480.

[135] S. Shirakata, T. Nakada, Thin Solid Films 515 (2007) 6151–6154.

[136] S. Shimakawa, K. Kitani, S. Hayashi, T. Satoh, Y. Hashimoto, Y. Takahashi, T. Negami, Physica Status Solidi (a) 203 (2006) 2630–2633.

[137] B. Ohnesorge, R. Weigand, G. Bacher, A. Forchel, W. Riedl, F.H. Karg, Applied Physics Letters 73 (1998) 1224.

[138] W.K. Metzger, I.L. Repins, M.J. Romero, P. Dippo, M.A. Contreras, R. Noufi, D.H. Levi, Thin Solid Films 517 (2009) 2360–2364.

[139] S. Shirakata, T. Nakada, Physica Status Solidi (c) 6 (2009) 1059–1062.

[140] C. Kittel, Semiconductor Physics, Oldenbourg Wissenschaftsverlag, 1999.

[141] M.I. Alonso, M. Garriga, C.A. Durante Rincón, E. Hernández, M. León, Applied Physics A: Materials Science & Processing 74 (2002) 659–664.

[142] M.I. Alonso, K. Wakita, J. Pascual, M. Garriga, N. Yamamoto, Physical Review B 63 (2001) 075203.

[143] A. Niemegeers, S. Gillis, M. Burgelman, in:, Proceedings of the 2nd WCPEC, 1998, pp. 672–675.

[144] M. Burgelman, J. Marlein, in:, Proceedings of the 23rd EU PVSEC, 2008, p. 2151.

[145] A. Niemegeers, M. Burgelman, in:, Proceedings of the 25 IEEE PVSC, 1996, pp. 901–904.

3 Article I: Optoelectronic characteristics of Cu(In,Ga)(S,Se)$_2$ thin film solar cells obtained from varied chalcogenization processes

Optoelectronic characteristics of Cu(In,Ga)(S,Se)$_2$ thin film solar cells obtained from varied chalcogenization processes

Robin Knecht, Martin Knipper, Jörg Ohland,
Ingo Riedel, and Jürgen Parisi

Abstract:

We investigated industrially produced chalcopyrite solar cells based on the absorber modifications Cu(In,Ga)Se$_2$ and Cu(In,Ga)(S,Se)$_2$ in order to study the nature of the experimentally verified efficiency improvement, mainly caused by an increased open circuit voltage. We show that the introduction of sulfur during the absorber formation via rapid thermal processing leads to a substantial lowering of the surface doping concentration and widening of the space charge region (SCR). Temperature dependent diode analysis revealed a reduction of the SCR recombination in (Se,S) devices which would lead to a larger splitting of quasi-Fermi levels and hence to an increased open circuit voltage as compared to neat Cu(In,Ga)Se$_2$ devices.

3.1 Introduction

Thin film solar cells made of the chalcopyrite compound semiconductor Cu(In,Ga)(S,Se)$_2$ (CIGSSe) exhibit strong potential for achieving high efficiency at low production costs [1]. Large scale production of CIGSSe-modules has been launched in different companies [2], but the transfer of high laboratory cell efficiencies reaching up to 20.1% [3] to the module scale (up to around 13% [4]) is still a major challenge. Improvement of the module efficiency in the large scale production process presents therefore a major issue to further lower production costs. Sulfurization of Selenium-based absorbers was found to enhance the solar cell performance [5-7]. Therefore modification of a pure Se-based rapid thermal processing (RTP) process to a Se-S RTP could be one beneficial step to achieve higher module efficiencies. In this work we studied the influence of the chalcogenization variation (individual selenization or selenization followed by sulfurization) during the RTP on the device characteristics of the thin film solar cells. In our experiments we used temperature dependent current-voltage measurements, external quantum efficiency measurements as well as capacitance-voltage profiling.

3.2 Experimental

Thin film solar cells based on either Cu(In,Ga)Se$_2$ or Cu(In,Ga)(S,Se)$_2$ have been obtained from cutting 1 cm^2 pieces from an industrially processed PV-module. The absorbers were prepared as follows: Sputtering metallic precursors Cu, In and Ga onto a preconditioned Mo film coated on a glass substrate. This was followed by the so-called chalcogenization process performed by rapid thermal processing which forms the actual absorber. In a first chalcogenization phase the absorber was heated up in a Se rich atmosphere to a temperature of $T = 550\,°C$ and is consecutively annealed at this temperature in a second phase either in a Se atmosphere (sample Se) or a S atmosphere (sample Se+S) resulting in a Se-rich absorber with a graded Ga content totaling to a Ga/Ga+In ratio of 23% and a Cu/Ga+In ratio of 92%. The heterojunction is formed by chemical bath deposition of a 50 nm thick CdS buffer layer. In the next step a thin layer of intrinsic zinc oxide is deposited by reactive RF magnetron sputtering onto the sample, followed by DC magnetron sputtering a highly aluminum-doped ZnO window layer. For better lateral current collection we deposited a 500 nm Ni front grid by vapor deposition. In order to contact the back electrode we used indium contacts for the molybdenum which has proven to improve the contact between the Mo-electrode and the gold pins used for the measurements.

Current-Voltage (IV) measurements for the basic characterization were performed using an Advantest TR 6143 source measure unit and a custom four probe sample holder. For the measurements under standard test conditions the samples were illuminated by a metal halide sun simulator. In order to measure the external quantum efficiency (EQE) a custom setup was used. A Xenon short-arc lamp and a halogen lamp were used as light sources combined with a Bentham monochromator TM300. The measurement signal was amplified by a Stanford Research Systems Lock-In Amplifier SR810 DSP. Temperature-and-illumination-dependent current-voltage (IV(T,P_L)) measurements were performed using a Keithley 2400 source measure unit. The sample was cooled in a Janis cryostat and its temperature controlled via a Lakeshore 330 temperature controller. The sample was illuminated by a Xenon short-arc lamp through a water filter to provide a spectrum comparable to AM1.5g and a programmable filter wheel with 6 neutral density filters transmitting 0%, 1%, 10%, 25%, 63% and 100% of the incoming light intensity. Capacitance-Voltage (CV) measurements were performed in a helium contact gas cryostat. The temperature of the samples was controlled using a Lakeshore 340 temperature controller. The measurement data was obtained with a Solartron SI 1260 Impedance/Gain-Phase Analyzer while assuming a parallel RC circuit as equivalent circuit.

3.3 Results

3.3.1 External Quantum Efficiency

Figure 3.1 shows the external quantum efficiency spectra of solar cells derived from the process variations Se and Se+S, respectively (The parameters deduced from the shape-analysis are summarized in Table 3.1). The general shape of the EQE spectra is the same for both sample types and only minor differences are observed in the absolute height of the quantum efficiency. The theoretical possible short circuit current density $J_{SC,AM1.5}$ was calculated using the AMG1.5 reference spectrum [8] and yielded slightly higher values for the Se-samples. The intercept with the energy axis of a linear fit to the low-energy edge of the EQE spectrum corresponds to the minimum band gap in the material and is $E_{g,min}$ = 0.97 eV in all cases. It is noteworthy that even if all spectra are normalized the Se+S samples have systematically lower quantum efficiencies on the low energy edge.
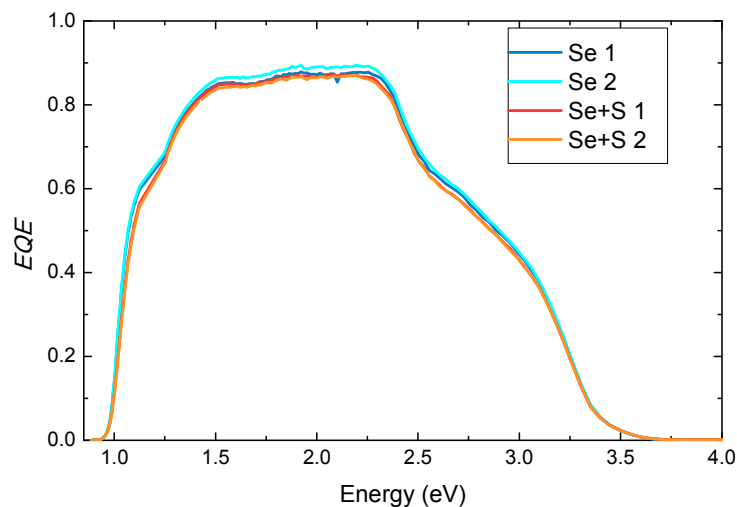
Figure 3.1: EQE (no optical bias) as function of photon energy plotted for the two absorber modifications: The Se samples (dashes) have only slightly better quantum efficiency as compared to the Se+S samples (dots) while the general shape is almost identical.

	EQE_{max} (%)	$J_{sc,AM1.5g}$ (mA/cm²)	$E_{g,min}$ (eV)	V_{oc} (mV)	$J_{sc,meas}$ (mA/cm²)	FF (%)	η (%)	E_A: $n \ln J_0$ (eV)	E_A: V_{oc} (eV)	V_D (mV)	$N_{A,eff}$ (x10^{15} cm^{-3})	SCR 0 bias (µm)
Se 1	87.9	32.0	0.97	504	34.0	71.6	12.3	1.06	1.01	511	10.2	0.26
Se 2	89.5	32.4	0.97	505	35.1	71.4	12.7					
Se+S 1	87.3	31.3	0.97	560	34.6	75.0	14.5	1.11	1.06	507	5.8	0.33
Se+S 2	87.0	30.9	0.97	558	35.0	74.0	14.5					

Table 3.1: Characterization parameters retrieved from the measurements presented in the text

3.3.2 Current-Voltage Characteristics

The results obtained from the IV characterization of the different samples are shown in Figure 3.2 and summarized in Table 3.1. The most pronounced effect of sulfur incorporation is the increase of the open circuit voltage (V_{OC}) of about 10% relative to values measured in the Se-only devices. Agreeing with the results obtained from the EQE integration the measured short circuit current density $J_{SC,meas}$ basically remains unchanged upon the addition of sulfur. Neither for the series resistance nor the shunt resistance a significant change was found such that the fill factor (*FF*) is increased by about 4 pp. Overall the power conversion efficiency (*η*) is substantially raised by about 2 pp in the samples treated with sulfur.
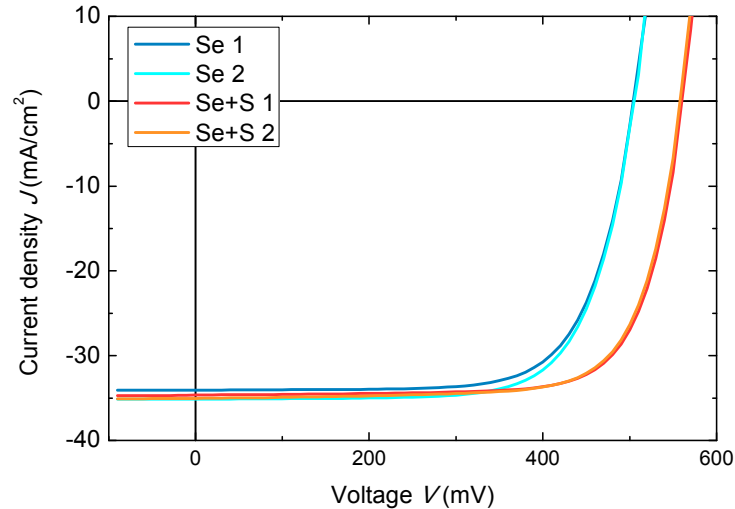
Figure 3.2: Results of current-voltage profiling of the two sample structures performed under standard test conditions: The introduction of S in the Se+S samples (dots) leads to a substantial increase of the V_{OC} as compared to the Se-only samples (dashed). Only minor effects of sulfurization on the J_{SC} and *FF* were observed.

3.3.3 Temperature and Intensity Dependent Current-Voltage Analysis

Temperature dependent current-voltage measurements give information about recombination mechanisms and the internal barriers present in the heterostructure [1]. According to the reformed Shockley equation (3.1), which can be found in textbooks such as [9], we can determine the ideality factor *n* and the saturation current density (J_0) from a semi-logarithmic

plot of J_{SC} vs. V_{OC}, pair wise determined at different illumination intensities (P_L) at a fixed temperature T.

$$\ln J_{SC} = \frac{q}{nkT} \cdot V_{OC} + \ln J_0 \qquad (3.1)$$

In (3.1) k is the Boltzmann constant and q the elementary charge. In our experiments IV curves were measured in the temperature range from 150 K to 300 K in steps of 10 K for five white light intensities ranging from 1 mW/cm^2 to 100 mW/cm^2. The IV data for the start and end temperatures are shown in Figure 3. The IV curves become distorted at a certain temperature below 300 K and exhibit a kink (rollover) which is more pronounced in samples including additional sulfur (dashed lines). This deviation from the expected Shockley behaviour in the first quadrant at low temperature is well known [10] for CIGS solar cells and reflects internal barriers impeding the minority carrier injection.
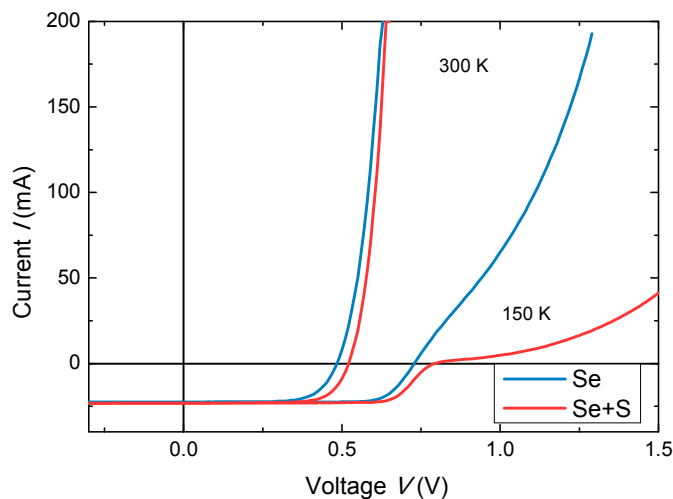
Figure 3.3: IV(T) characteristics recorded for both sample variations in the dark and under PL = 100 mW/cm2 for T = 300 K and T = 150 K. At low temperatures the Se+S sample (dashed lines) exhibit substantial impedance of the injection current as compared to the Se sample (straight line).

At room temperature the ideality factors lie between 1.4 (Se+S) and 1.7 (Se) indicating that recombination in the space charge region is the predominant recombination mechanism in both sample variations [1].

Using (3.1) one obtains J_0 from the intercept of the characteristics with the current-density axis. J_0 is considered to be thermally activated following the Meyer-Neldel rule [11,12] with activation energy E_A and a nearly temperature independent prefactor J_{00}:

$$J_0 = J_{00} e^{\frac{-E_A}{nkT}} \qquad (3.2)$$

Since the ideality factor is temperature dependent one must plot

$$n(T) \ln J_0 = n(T) \ln J_{00} - \frac{E_A}{kT} \qquad (3.3)$$

to retrieve the activation energy as shown in Figure 3.4.
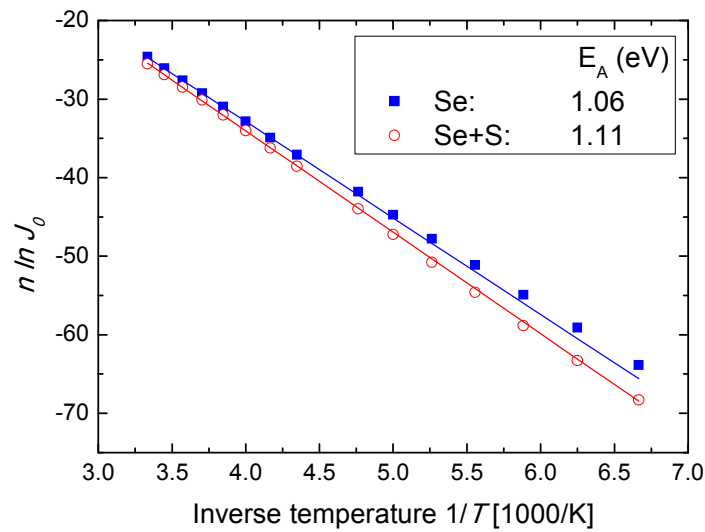
Figure 3.4: Derivation of the ideality factor, saturation-current density and activation energy from the "suns-V_{OC}-method". The slope relates to the activation energy via equation (2). It is slightly lower for the Se sample (square) than the Se+S sample (circle). The activation energies obtained from the fits are presented in Table 3.1.
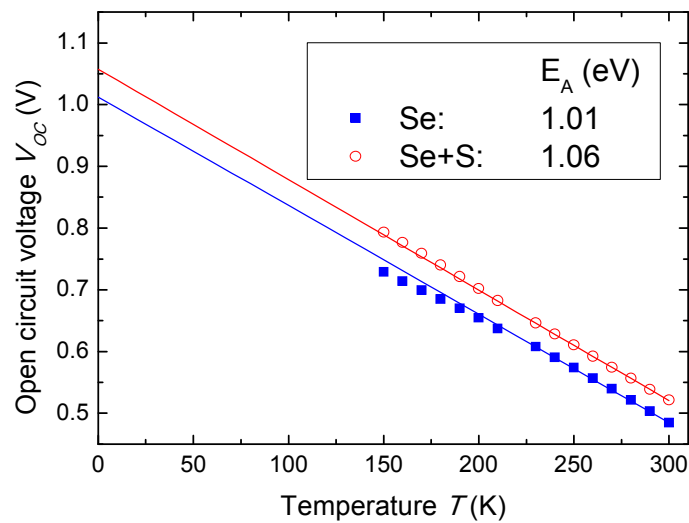
Figure 3.5: Variation of the open circuit voltage with temperature for both absorber types under study (P_L = 100 mW/cm2): The T = 0 K limit of the linear V_{OC} extrapolation relates to the activation energy responsible for the V_{OC}-limitation according to (3). E_A is slightly lower for the Se sample (square) than the Se+S sample (circle).

A second approach to calculate the activation energy of recombination is derived from equations (1) and (2):

$$V_{OC} = \frac{E_A}{q} - \frac{nkT}{q} \cdot \ln\left(\frac{J_{00}}{J_{SC}}\right)$$

(3.4)

Equation (3.4) predicts a nearly linear decrease of V_{OC} with increasing temperature such that from a linear fit of $V_{OC}(T)$ the activation energy (E_g/q) is obtained from the intercept with the V_{OC}-axis. The results obtained from this method are presented in Figure 3.5. The fitting range was restricted to the temperature range where the influence of the rollover effect on V_{OC} could be neglected. In both cases the activation energies correspond well to the band gap energy close to the heterojunction. Both methods show that E_A is slightly higher in the Se+S-sample than the Se-sample corresponding to expectations in the literature [13].

In the paper by Schock and Rau [1] it is argued that the measured E_A in equation (3.2) corresponds to the band gap energy if the ideality factor is about 2 which is roughly the case.

3.3.4 Capacitance-Voltage-Profiling

CV measurements give information about the depth profile of the doping concentration N_{eff}, the diffusion potential V_D and the width w of the SCR, which is derived by approximating the SCR with a plane plate capacitor: $w = \varepsilon_0\varepsilon_r/C$ [14]. These values can be determined by measuring the area-normalized capacitance C at a particular bias voltage V and applying the Mott-Schottky relation (assuming n$^+$p) [15]:

$$\frac{1}{C^2} = \frac{2}{\varepsilon_0\varepsilon_r q}\frac{1}{N_{eff}}(V_D - V)$$

(3.5)

where ε_0 is the dielectric constant and ε_r is the relative permittivity of the material. By plotting $1/C^2$ vs. V one should obtain a straight line if the doping concentration does not vary with distance from the heterojunction and defect concentrations are homogeneously distributed
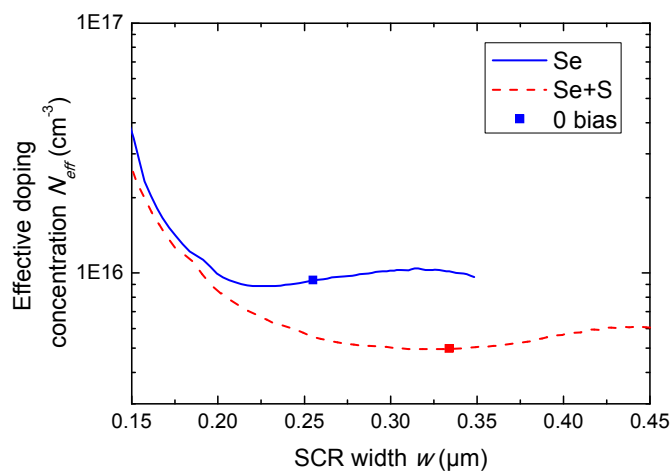
Figure 3.6: Depth profile of the doping concentration for the Se-only sample (straight line) and the Se+S sample (dashed line) as determined from CV measurements. The width of the space charge region in equilibrium is indicated by the full squares. Measured at T = 300 K and ω = 30 kHz.

across the absorber volume. In chalcopyrite absorbers both conditions are likely to be not fulfilled resulting in a non-linear variation of $1/C^2$ vs. V. One can still estimate the spatial variation of the doping concentration by altering w with the applied voltage. By measuring at high frequencies exceeding the emission rate of deep defect levels their influence is reduced and the condition of homogenous defect concentrations fulfilled. In our experiments the fit to estimate V_D was performed in the negative bias region, where the characteristics can be approximated linearly yielding a value of about 510 mV for both sample types. In the Se-only case the diffusion voltage is therefore similar to the open circuit voltage. Surprisingly, the doping concentration for the Se-only sample is double as high as for the Se+S sample. The results of the Mott-Schottky-analysis are summarized in 0. The doping depth profile derived from CV analysis is shown in Figure 3.6. Both samples show inhomogeneously distributed doping concentrations in the expected U-shape [16]. Note that the equilibrium width of the SCR (■ in Figure 3.6) is nearly 100 nm larger in the sulfurized sample.

3.4 Discussion

Compared to the reference system Cu(In,Ga)Se$_2$ the data obtained from IV-characterization clearly demonstrates substantial improvements of the device efficiency in Cu(In,Ga)(S,Se)$_2$ solar cells, mainly caused by increased fill factor and open circuit voltage. The short circuit current remained basically unchanged as determined from the IV data and the integrated quantum efficiency spectra. For both sample types the overall shape of the EQE spectra is almost identical and the absorption onsets coincide which lets us conclude that there is no significant effect of sulfur incorporation on the minimum band gap energy of the absorber material. In the literature several authors report that the introduction of sulfur increases the surface band gap energy of the host material [13]. This discrepancy can be explained by an almost S-free region within the Se+S absorber which has the same bandgap as the Se absorber. The minimum bandgap of both materials measured by EQE is therefore the same. The observed difference in V_{OC} in the IV characteristic is too large to be solely explained by the higher band gap as has been argued by Rau et al [7] and explained through passivation of midgap recombination centers at the heterojunction interface by sulfur. CV measurements showed that the spatial doping profile is different in sulfurized samples: The lower doping concentration at the surface observed in (Se,S) samples can possibly be explained by sulfur compensating the copper depletion close to the heterojunction leading to a slight broadening of the SCR. This particular effect is not very clear at the moment. Competing issues are the increased SCR recombination compared to the improved carrier collection. As the respective ideality factor is by 0.15 lower than derived for the Se-samples, reduction of the SCR recombination rate may therefore be concluded. In the $IV(T,P_L)$ measurements we observe in both cases a rollover effect at 150 K but much more severe for the (Se,S) device. In the literature the origin of rollover effect is explained by an internal barrier for minority carrier injection but the location of this barrier is heavily debated. Discussed locations are a non-Ohmic back contact at the CIGS/Mo interface [16], the spike at the band discontinuity between the CIGS/CdS heterojunction [17] or acceptor-like defect states in or close to the ODC layer [10]. We observe that the addition of sulfur leads to an increased distortion which corresponds to an increase of this barrier even though a combined effect cannot be excluded. It is therefore not possible for us to localize the origin of the rollover effect. The activation energies of the saturation currents and the open circuit voltages correspond well to the band

gap within the SCR in both sample types. Thus rather SCR- than interface recombination dominates the recombination losses.

3.5 Conclusion

We have presented the effects on various solar cell parameters when sulfur is added during the absorber formation in the chalcogenization process of chalcopyrite solar cells. A substantial increase of the open circuit voltage was observed in (Se,S) samples. Capacity-voltage measurements have shown an increase in the space charge region width in the S-alloyed sample, while its effective doping concentration in the vicinity of the SCR is halved, but the diffusion voltage does not change in spite of this. A lower surface doping concentration causes a widening of the SCR whereas no indication was found for increased SCR recombination or improved collection efficiency in the (Se,S) samples. The lower ideality factor in (Se,S) samples indicates that SCR recombination is reduced which has a direct and beneficial consequence for the open circuit voltage. The activation energy of the saturation current (slightly higher than the minimum bandgap determined from external quantum efficiency measurements) corresponds to the SCR band gap in both absorber cases which indicates minor interface recombination. It has been shown that $Cu(In,Ga)(S,Se)_2$ thin film solar cells from an industrial production process with S-Se-chalcogenization demonstrate improved cell performance due to a higher fill factor and open circuit voltage. In this work the dominant reason was found in a reduced recombination loss in the vicinity of the widened SCR region. Future work will address the investigation of the defect states in these absorbers in order to include changes of the defect state distribution and the creation/annihilation/conversion of such centers. Also further measurements have to be carried out to localize the origin of the rollover effect.

References:

[1] U. Rau, H.W. Schock, Applied Physics A 69 (1999) 131.

[2] W. Diehl, V. Sittinger, B. Szyszka, Surface and Coatings Technology 193 1-3 (2005) 329.

[3] M.A. Green, K. Emery, Y. Hishikawa, W. Warta, Progress in Photovoltaics: Research and Applications 18 (2010) 346.

[4] K. Kushiya, Solar Energy 77(6) (2004) 717.

[5] R. Gay, M. Dietrich, C. Fredric, C. Jensen, K. Knapp, D. Tarrant, D. Willett, in: Proceedings of the 12th EU PVSEC, 1994, p. 935.

[6] T. Nakada, H. Ohbo, T. Watanabe, H. Nakazawa, M. Matsui, A. Kunioka, Solar Energy Materials and Solar Cells 49 (1997) 285.

[7] U. Rau, M. Schmitt, F. Engelhardt, O. Seifert, J. Parisi, W. Riedl, J. Rimmasch, F. Karg, Solid State Communications 107 2 (1998) 59.

[8] Reference Solar Spectral Irradiance Air Mass 1.5, http://rredc.nrel.gov/solar/spectra/am1.5/ASTMG173/ASTMG173.xls , 2. Feb. 2010.

[9] J. Nelson, The Physics of Solar Cells, Imperial College Press, London, 2003.

[10] M. Topic, F. Smole, J. Furlan, Solar Energy Materials and Solar Cells 49 (1997) 311.

[11] A. Yelon, B. Movaghar, R.S. Crandall, Reports on Progress in Physics 69 (2006) 1145.

[12] R. Herberholz, T. Walter, C. Müller, T. Friedlmeier, H.W. Schock, M. Saad, M.Ch. Lux-Steiner, V. Alberts, Applied Physics Letters 69 (1996) 2888.

[13] I.M. Kötschau, H.W. Schock, Journal of Applied Crystallography 39 (2006) 683.

[14] S.S. Hegedus, Progress in Photovoltaics: Research and Applications 12 (2004) 155.

[15] S.M. Sze, Physics of Semiconductor Devices, Wiley, New York, 1981.

[16] T. Eisenbarth, T. Unold, R. Caballero, Ch.A. Kaufmann, H.W. Schock, Journal of Applied Physics 107 (2010) 034509.

[17] A.O. Pudov, J.R. Sites, M.A. Contreras, T. Nakada, H.W. Schock, Thin Solid Films 480–481 (2005) 273.

4 Article II: Impact of varied sulfur incorporation on the device performance of sequentially processed Cu(In,Ga)(Se,S)$_2$ thin film solar cells

Impact of varied sulfur incorporation on the device performance of sequentially processed Cu(In,Ga)(Se,S)$_2$ thin film solar cells

Robin Knecht, Maria S. Hammer, Jürgen Parisi, and Ingo Riedel

Abstract

In order to improve the performance of chalcopyrite $Cu(In_{1-x},Ga_x)(Se_{1-y}S_y)_2$ solar cells, the implementation of a bandgap widening at the absorber/buffer interface via an increase of the [S]/[S+Se] ratio is investigated. In this work we examine industrially processed samples, which were fabricated via the deposition-reaction process with varied H_2S pressure during rapid thermal processing (RTP). Precursors which were exposed to a crucial amount of sulfur during the RTP step resulted in samples with significantly improved device performance. The increase of the open circuit voltage by about 150 mV cannot sufficiently be explained by bandgap widening. Observation of a strongly reduced saturation current density and ideality factor in intensively sulfurized samples suggest subdued recombination via mid-gap defect states located in the space charge region. This hypothesis is supported by results of deep-level transient spectroscopy measurements which show that in both samples a mid-gap minority defect is present albeit its concentration is about one magnitude larger in sulfur-poor samples. These results confirm that sulfur passivates recombination centers in the depletion layer and hence significantly increases the open circuit voltage and the overall device performance of the photovoltaic devices.

4.1 Introduction

$Cu(In_{1-x},Ga_x)(S_y,Se_{1-y})_2$ (CIGSSe) chalcopyrite thin films demonstrate remarkable flexibility for application in photovoltaic devices due to the tunability of the position of energy bands and the width of the energy bandgap in a wide range [1–3]. Power conversion efficiencies of 20.3% were recently achieved for co-evaporated $Cu(In,Ga)Se_2$ (CIGS) laboratory cells using absorber films with a double bandgap grading at the front and back contact [4]. The bandgap engineering is realized through variation of the ratios $x = $ [Ga]/[Ga+In] (GGI) and $y = $ [S]/[S+Se] (SSSe) throughout the absorber thickness [5]. By varying the x and y values, bandgaps between $E_g = 1.04$ eV ($CuInSe_2$) and $E_g = 2.47$ eV ($CuGaS_2$) can be realized [6]. In the sequential deposition reaction, i.e., selenization/sulfurization of metal precursor films, it is difficult to achieve a bandgap widening at the absorber surface because of different reaction kinetics of the binary phases. This results in a segregation of a Ga-depleted chalcopyrite phase close to the heterojunction and a Ga-rich phase at the back contact [7]. The selenized precursor is therefore exposed to sulfur vapor in a final step of the deposition reaction which creates a thin, sulfur-enriched surface region of the chalcopyrite [8]. Due to the symmetric separation of the band edges upon sulfur incorporation [9], the hole-recombination barrier at the heterojunction is increased and interface recombination reduced. Practically, the amount of sulfur (y) as well as the extension of the CIGSSe phase into the absorber volume needs to be thoroughly optimized in order to benefit from this approach. Previous work on this subject suggested a further beneficial effect of sulfur incorporation in terms of passivation of deeper trap states in the space charge region as confirmed by admittance spectroscopy [10]. This method is however less suitable for the investigation of deep trap states and only sensitive to majority carrier traps [11].

In this work we studied the effect of varied sulfur incorporation on CIGSSe samples obtained from a large-scale industrial deposition reaction process. The samples were varied in terms of the sulfur concentration during the final sulfurization step. By inspection of the chemical depth

profiles, x-ray diffraction patterns, and the device cross sections the structural differences are analyzed. Differences in the device performance are subsequently investigated by application of a basic characterization consisting of current-voltage, external quantum efficiency, and capacitance-voltage measurements. Deep-level transient spectroscopy is a suitable method for characterization and evaluation of deep traps in chalcopyrite devices [12] and has been applied to investigate the sulfur-induced passivation of deep trap states.

4.2 Experimental

4.2.1 Samples

The investigated modules were manufactured using the deposition reaction process detailed in principle elsewhere [13,14]. Deposition of molybdenum as a back contact and of the metallic precursors Cu, In, Ga was performed via DC-magnetron sputtering from 150 cm long cathodes under equal conditions. The composition was slightly Cu deficient and $x = 0.23$. Chalcogenization was achieved using rapid thermal processing (RTP) in a reactive H_2Se/H_2S atmosphere at 525 °C containing nominally either no sulfur (S0) or a small amount (S1), medium amount (S2) or high amount (S3) of sulfur. The subsequent deposition of the CdS buffer layer by chemical bath deposition, the intrinsic ZnO layer by RF magnetron sputtering and the ZnO:Al window layer by DC-sputtering was again performed equally for all samples. No patterning was performed on the coated sheets. Instead five 15 cm $\times$ 15 cm slates were cut from different positions of each sheet and transported in bags under nitrogen atmosphere to the investigation lab. For electric measurements 200 nm thick Ni grids were evaporated onto the window layer using electron beam physical vapor deposition. The absorbers were now divided into 8×8 solar cells of 1 cm^2 size using mechanical scribing such that each cell contains one Ni grid and the active area is about 0.85 cm^2. Some methods required the removal of the window and buffer layers realized by etching in 5 % hydrochloric acid.

4.2.2 Characterization methods

External quantum efficiency (EQE) measurements were performed with a Bentham PVE300 spectrometric EQE system. Current-voltage measurements under standard test conditions (STC-IV) were performed using a solar simulator featuring a metal-halide lamp (HMI 575W/Se) and an Advantest TR6143 source-meter unit (SMU) operated in 4-probe configuration. The light intensity of the light source was calibrated with a 4 cm^2 mc-Si-reference cell (Fraunhofer ISE calibration lab) and the measured cell light-current was corrected for the spectral mismatch of the solar simulator. In order to determine the current density, only the illuminated area of the solar cells was accounted for, which was determined via high resolution photography. To ensure statistical significance, 4-6 cells for each process variation have been characterized. Capacitance-voltage measurements were performed using a Solartron SI1260 impedance-gain/phase analyzer. Temperature and light-intensity dependent current-voltage measurements (IV-T) were performed in an optical nitrogen-cooled cold finger cryostat under vacuum. The temperature stabilization of the sample was done with a LS-330 temperature controller together with a Pt-100 sensor mounted on the sample surface. For IV-T measurements, IV data were assessed with a KTH 2400 SMU in four-probe configuration at five illumination levels per temperature step.

For chemical depth profiling, glow discharge optical emission spectroscopy (GDOES) was performed on etched devices using a Spectruma GDA750 GDOES spectrometer. X-ray diffraction (XRD) measurements were carried out with an X'Pert Pro MRD diffractometer (PanAlytical) using a Cu-Kα radiation source. The XRD spectra were evaluated using the X'Pert Pro HighScore Plus software. Scanning electron microscopy (SEM) and preparation of cross sections by focused ion beam milling were performed using a FEI Helios Nanolab 600i. DLTS was done with a custom-built transient-DLTS based on a Boonton 7200 capacitance meter using a sampling frequency of 1 MHz for measuring the transients of the sample capacitance.

4.2.3 Structural characterization

The actual ratios of H_2S/H_2Se in the reactive atmosphere do not necessarily reflect the amount of sulfur incorporated into the device. Therefore GDOES was applied on samples with removed window and buffer layers in order to evaluate the content and distribution of sulfur in the absorber. The inset of Figure 4.1 shows the profile of y and in Table 4.1 the integrated amounts of sulfur relative to the most sulfur-rich sample ($S/S3$) are summarized.

Interestingly, sample S0 which was processed in a pure H_2Se atmosphere contained traces of sulfur which seem to originate from sulfur remaining in the process chamber from previous sulfurization of different absorbers.

The x profile (not shown) reveals the segregation between a Ga-depleted phase close to the heterojunction ($x < 0.01$) and a Ga-rich phase towards the back contact. As CIGSSe is polycrystalline the detected sulfur could potentially accumulate at the grain boundary instead of being incorporated into the chalcopyrite crystal. The chalcopyrite lattice constants are influenced by x and y which can be observed as a shift in XRD patterns. The measurements were performed on etched devices in order to avoid the superposition of reflection peaks by the window and buffer layers and evaluated after height dislocation correction.
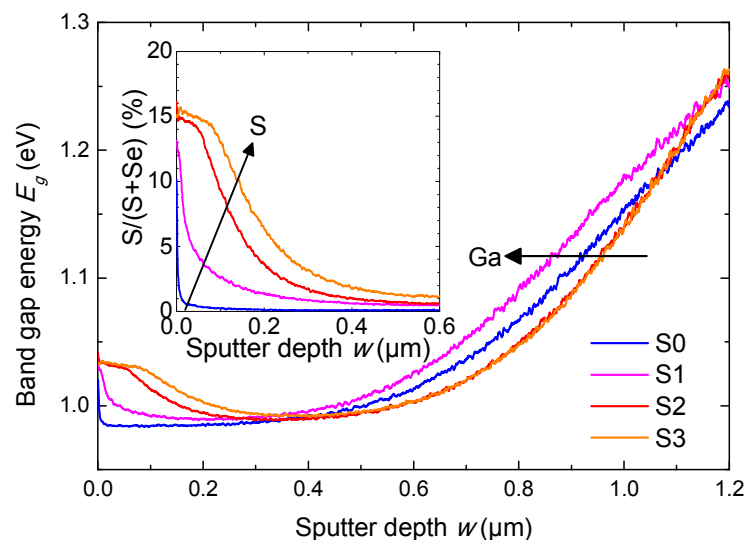
Figure 4.1   Bandgap energy profile of samples S0-S3 as calculated from element-specific signal intensities of the GDOES profiles. The inset shows the sulfur concentration profiles close in the surface region of the absorber.
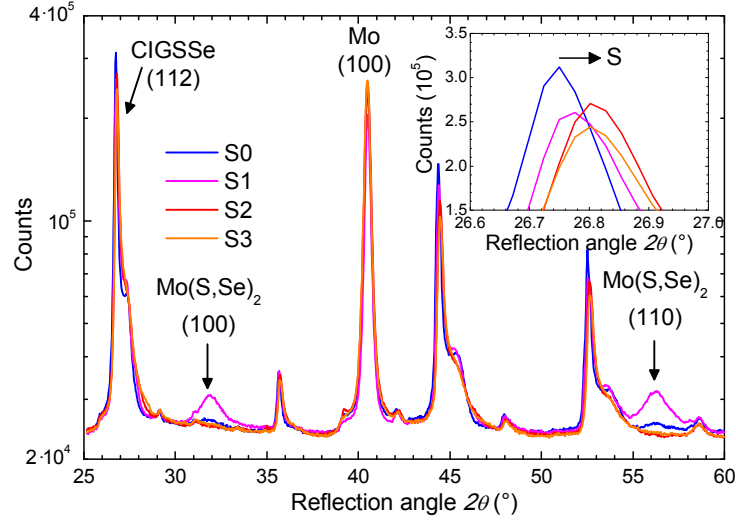
Figure 4.2 XRD-patterns of etched samples S0-S3. The inset shows a magnified view of the top of the CIGSSe (112) peak.

In Figure 4.2 the CIGSSe patterns appear as a superposition of two slightly shifted peaks. Grazing incidence XRD at different angles (not shown) relate the peak at higher reflection angles to a phase at the back contact which according to GDOES corresponds to the Ga-rich phase. The larger peak at lower reflection angles is therefore related to the Ga-depleted phase close to the heterojunction. The shift of the CIGSSe (112) peak in the inset in Figure 4.2 is therefore attributed to the incorporation of sulfur. Assuming $x = 0$ the calculated values of y are given in Table 4.1 and confirm the incorporation of sulfur into the chalcopyrite crystal. This motivates the calculation of the local bandgap $E_g(x,y)$ from the x and y profiles via Eq. (4.1) [15] which results in the double bandgap grading displayed in Figure 4.1:

$$E_g(x,y) = (0.98 + 0.167x^2 + 0.17y^2 + 0.0023x^2y - 0.17xy^2 + 0.397xy + 0.31y + 0.523x) \text{ eV} \quad (4.1)$$

The front grading observed for samples S1-S3 is caused by the sulfur incorporation while the increase of $E_g(x,y)$ towards the back contact is essentially due to the strong Ga accumulation. Samples S2 and S3 exhibit the highest sulfur concentration at the heterointerface and a deep penetration of sulfur into the space charge region.

Noticeable in Figure 4.2 is also a difference in the peaks around $2\theta = 31.9°$ resp. $2\theta = 56.2°$ which are identified as (100) and (110) signatures of $Mo(Se,S)_2$ [16]. Inspecting the back contact region in the SEM cross sections shown in Figure 4.3 we observe such intermediate layer between the CIGSSe and Mo films. Typical for sequentially processed chalcopyrite films the absorber does not adhere to the $Mo(Se,S)_2$ layer at some locations [17]. By measuring the molybdenum surface to the edge of voids closest to the back contact the thickness of the $Mo(Se,S)_2$ layer can be estimated. The measured average thickness of the $Mo(Se,S)_2$ layers is given in Figure 4.3. Samples S2 and S3 exhibit the thinnest $Mo(Se,S)_2$ film which was found to be more amorphous than in sample S1 as revealed by XRD texture measurements (not shown). The reduced crystallinity in the thinner films explains that the corresponding XRD signatures could not be resolved.
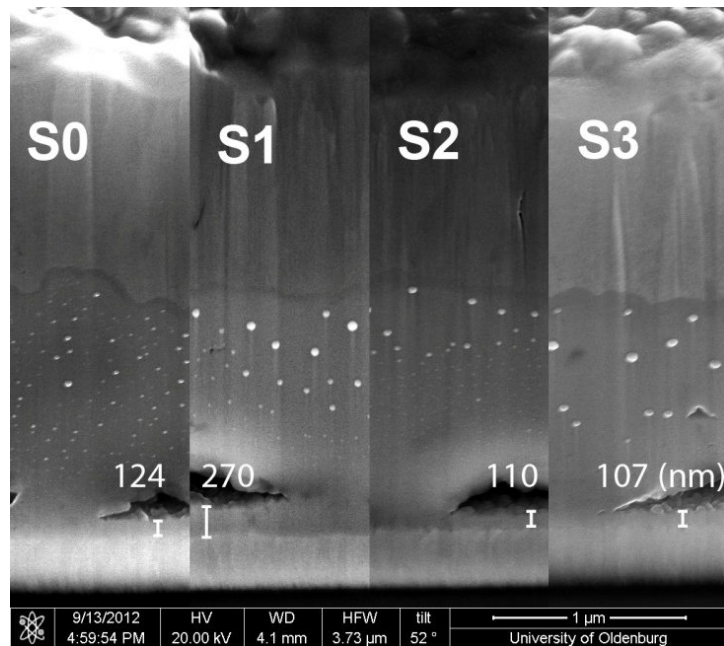
Figure 4.3 Scanning electron microscopy image of the samples under investigation. A Mo(S,Se)$_2$ layer reactively formed on top of the molybdenum back electrode during formation of the CIGSSe film.

As for the origin of the observed difference in Mo(Se,S)$_2$ formation, slightly different substrate temperatures during absorber processing of samples S0-S3 are the most likely explanation. This is supported by GDOES results which show that in S1 gallium has diffused the farthest towards the front while the second farthest gallium progression was found in sample S0 following the trend observed with the Mo(Se,S)$_2$ thickness. For this deposition method it is known that gallium diffusion towards the heterojunction increases with temperature often accompanied by the secondary effect of accelerated Mo(Se,S)$_2$ formation under Se overpressure [17]. Despite different formation of the intermediate Mo(Se,S)$_2$ layer the morphology of the other layers in the device stack seem to be comparable.

4.2.4 Performance characterization

The photovoltaic performance of the devices was extracted from STC-IV measurements. The analysis of the data was done according to a procedure described in [18]. The results are shown in Figure 4.4 and the characteristic sample parameters are summarized in Table 4.1. Qualitatively, the four samples separate into two categories characterized by a low and a high V_{OC} value. With respect to sample S0 we observe a considerable improvement of V_{OC} for devices processed with medium/high sulfur concentration (samples S2/S3). Within statistical error ($\sigma(J_{SC}) < 1$ mA/cm^2) the measured J_{SC} are rather close for all samples reflecting results from EQE measurements (inset of Figure 4.4) with S3 being slightly lower.

The observed difference in V_{OC} for the samples S0/S1 and S2/S3 directly correlates with the values of the ideality factor A and the saturation current density J_0 which have been extracted from the $J+J_{SC}$ characteristics (Table 4.1). Both diode parameters are further analyzed by IV-T measurements in the temperature range $T = 150$ K–300 K at different illumination levels. At low temperatures a rollover could be observed at $V > V_{OC}$ for all samples which indicates the
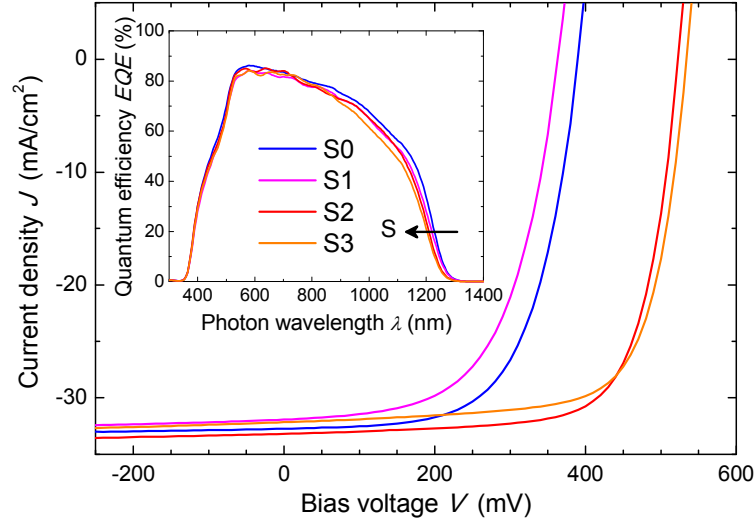
Figure 4.4 Current-voltage characteristics (STC-IV) of representative CIGSSe solar cells with varied sulfur concentration. EQE spectra of samples S0-S3 with different sulfur concentration. The spectra were taken without additional white-light bias under short circuit conditions.

presence of an injection barrier either at the front or at the back contact which is addressed in section 4.3.

The saturation current density is thermally activated and independently of the particular recombination channel can be expressed by the general form [19,20]:

$$J_0 = J_{00} \cdot exp(-E_a \, / \, AkT),$$ (4.2)

where the reference current density J_{00} is nearly independent of temperature, E_a is the activation energy of the saturation current density and kT is the thermal energy. The activation energy is related to the location of the dominating recombination channel [20] and according to equation (4.2) can be determined from the $J_0(T)$ characteristics as the slope of $A \cdot ln(J_0)$ versus the inverse temperature in an Arrhenius plot (Figure 4.5).

From the IV-T characteristics, we determined the parameters A and J_0 from a linear fit of $A \cdot ln(J_{SC})$ vs. V_{OC} for each temperature step. This method allows the assessment of the diode parameters without being influenced by the series resistance [21]. The ideality factor of samples S0, S2 and S3 is essentially independent of temperature whereas A of S1 increases upon cooling the device (inset of Figure 4.5). The temperature dependent contribution to A was related to tunneling-

sample	S/S3 (%)	γ_{XRD}	J_{SC}^{EQE} (mAcm^{-2})	J_{SC}^{IV} (mAcm^{-2})	V_{OC} (mV)	FF	η (%)	A	J_0 (Acm^{-2})	$E_{g,min}$ (eV)	E_a (eV)
S0	4	0.13	33.5	31.0	389	0.63	7.6	1.91	$1.1 \cdot 10^{-5}$	0.99	1.11
S1	29	0.15	32.3	30.4	363	0.59	6.5	2.03	$2.8 \cdot 10^{-5}$	1.00	0.83*
S2	72	0.17	33.7	31.6	523	0.72	11.9	1.51	$4.3 \cdot 10^{-8}$	1.01	1.09
S3	100	0.17	31.7	30.8	535	0.72	11.8	1.50	$3.0 \cdot 10^{-8}$	1.02	1.12

Table 4.1 Solar cell parameters determined from GDOES, XRD, IV, EQE, and IV-T(* corrected according to ref. [19])
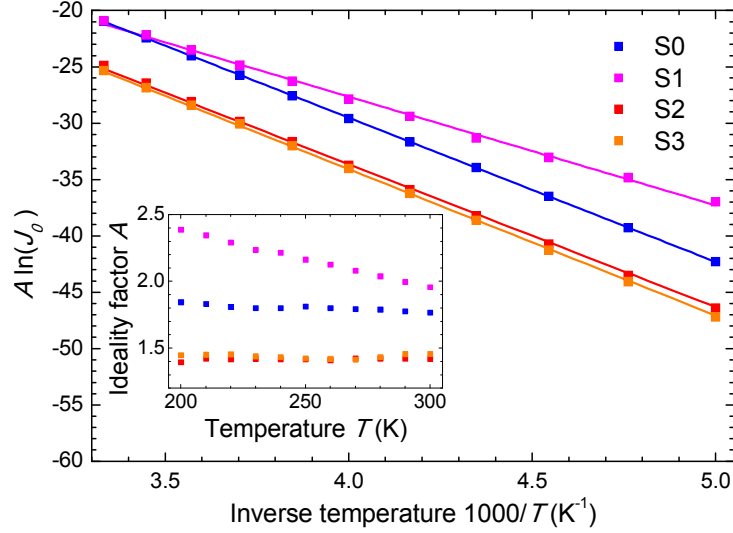
Figure 4.5 The activation energy of the saturation current density of samples S0-S3. The solid lines are fits to eq. (4.2). The values of A and J_0 have been derived from evaluation of $\ln(J_{SC})$ vs. V_{OC} at the corresponding temperatures.

assisted recombination via energetically distributed defect levels in the SCR [19] and necessitates a correction in that only the temperature independent contribution is used in the calculation of E_a. Details about the correction follow in the discussion. The calculated E_a are presented in Table 4.1.

For samples S0, S2 and S3 we obtained an E_a close to the interface bandgap (compare Figure 4.1) which indicates dominant bulk recombination. Exclusively for S1 we found an activation energy below the interface bandgap which points towards interface recombination as a dominating recombination channel competing with SCR recombination. The ideality factor of $A \sim 2$ suggests that the device performance of samples S0/S1 is limited by carrier recombination via mid-gap states in the space charge region. This loss channel appears to be impeded (e.g. by defect passivation) in the sulfurized samples S2/S3 as reflected by the lowered ideality factor, i.e., $A \sim 1.5$. The large difference of J_0 between S0/S1 and S2/S3 (three orders of magnitude) indicates dramatic carrier recombination in the samples with insufficient sulfur content.

Therefore the presence and concentration of mid-gap defect states was investigated with DLTS [11]. In a DLTS measurement, the heterojunction is held at a negative voltage bias V_r to empty a fraction of the trap states in the SCR. The junction capacitance in this state is named C_0. A forward bias pulse $V_f > V_r$ is applied filling the emptied traps with charge carriers (minority DLTS). After the filling pulse the device is again held at V_r and the occupied traps release their trapped carriers resulting in an exponential change $\Delta C(t)$ of the junction capacitance with reference to C_0 [22]:

$$\frac{\Delta C(t)}{C_0} = \pm \frac{N_t}{2N_{d,eff}} \exp(-e_{n/p}t) \tag{4.3}$$

In Eq. (4.3) $N_{d,eff}$ is the effective doping concentration, N_t the density of occupied trap states, $e_{n/p}$ the trap emission rate for holes (electrons) and t is the time. The sign of the transient indicates the trap type, being negative for majority carrier traps and positive for minority carrier traps. The time constant of the capacitance transient $\tau_{n/p} = 1/e_{n/p}$ relates to the trap energy level E_t according to:

$$e_{n/p} = \underbrace{N_{C/V} v_{th} \sigma_{n/p}}_{T^2 \xi_0} \exp\left(\frac{-|E_t - E_{C/V}|}{kT}\right) \qquad (4.4)$$

Here $N_{C/V}$ and $E_{C/V}$ is the effective density of states resp. the energy level of the conduction/valence bands, v_{th} the thermal velocity and $\sigma_{n/p}$ the capture cross section of the trap.
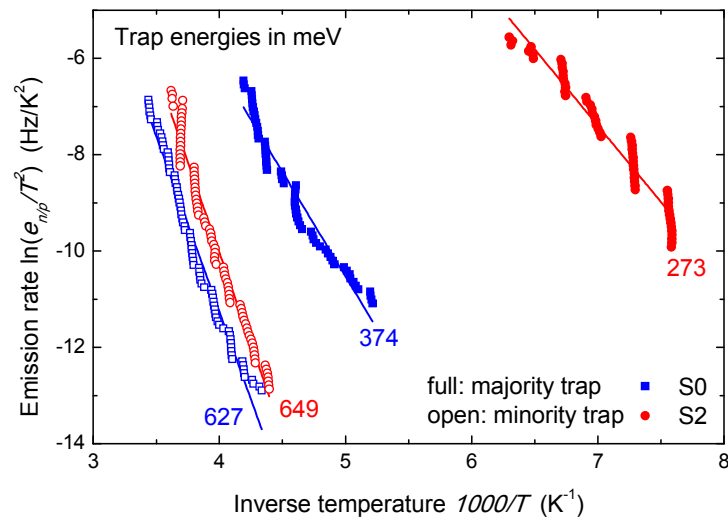
Figure 4.6   Arrhenius plot of the carrier emission rates showing the mid-gap minority defect and a majority defect detected in samples with relative small (S0) and high (S2) sulfur incorporation.
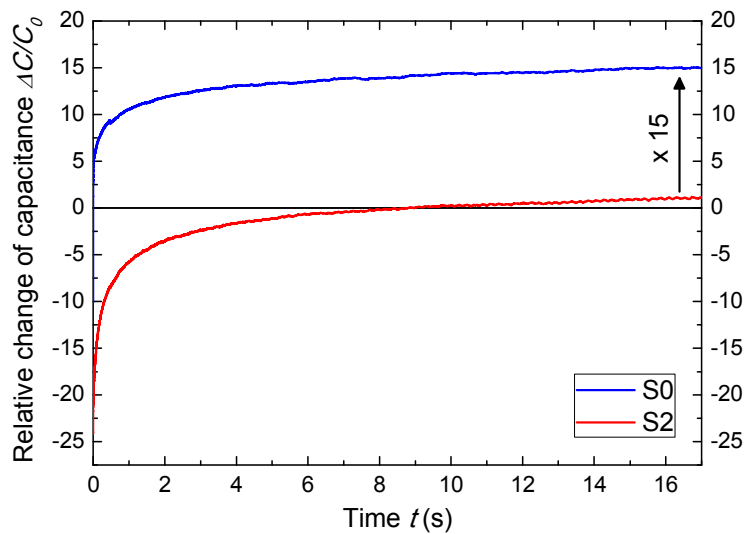
Figure 4.7   Capacity transients at 300 K in samples without or with sulfur incorporation. The majority trap transient is shifted up by superposition with a minority transient with a longer time constant.

The exponential coefficient contains a T^2 dependency and a temperature-independent contribution ξ_0.

The trap emission rate is determined with the lock-in analysis of the transients in the temperature range T = 30 K–350 K enabling the determination of the trap energy levels from an Arrhenius plot (Figure 4.6). Samples without and with a crucial amount of sulfur, i.e. S0 and S2, yield a mid-gap minority carrier defect for both samples which shows up around room temperature. Moreover, deep majority carrier traps with different activation energies were found in S0 and S2 which are superimposed to the minority carrier emission at room temperature (Figure 4.7).

From Eq. (4.3) follows that the concentration N_t of a single defect can be extracted from the transients by determination of the initial $\Delta C/C_0$ at t = 0 and $N_{d,eff}$. The latter is obtained by CV measurements which are analyzed according to [18] giving $N_{d,eff}$ = 6.5 × 10^{15} cm^{-3} for S0 and $N_{d,eff}$ = 9.6 × 10^{15} cm^{-3} for S2. The occupied trap state densities are evaluated and put in relation in the next section.

4.3 Discussion

From the results of the STC-IV measurements (Table 4.1) can be seen that the J_{SC} of all samples are within statistical error which is in accordance with previous reports that moderate sulfur concentrations in the surface region of the CIGSSe absorber have only minor impact on J_{SC} [20]. Sample S3 has a slightly reduced J_{SC}, which fits the expectation that an increased sulfur content causes a larger bandgap reducing photon absorption in the space charge region and hence J_{SC}. This trend is supported by EQE measurements. By integration of the EQE spectra in the inset of Figure 4.4 and multiplication with the AM1.5G spectrum one calculates J_{SC} which would be obtained under standard test conditions [23,24]. The corresponding J_{SC} values are presented in Table 4.1. The shape of the EQE spectra provides insight into the optical and electronic loss mechanisms [18]. One loss mechanism in samples containing sulfur which was already mentioned above is the decreased absorption due to a larger minimum bandgap $E_{g,min}$ which is seen in the EQE spectra in a shift of the high wavelength edge to lower wavelengths. Assuming a direct fundamental bandgap the extrapolation of the squared EQE yields the smallest bandgap present in the absorber material (Table 4.1) which gradually increases (by some 10 meV) with increasing sulfur content. We note that extraction of $E_{g,min}$ from the EQE spectra is physically not really accurate as the near-infrared slope of the EQE is influenced by several loss mechanisms yet the extracted $E_{g,min}$ are reasonably close to the $E_{g,min}(x,y)$ values determined from respective GDOES profiles. Physical mechanisms which impact the current loss in the infrared regime ($\lambda > 830$ nm, $E_{ph} < 1.5$ eV) are free carrier absorption in the ZnO:Al window layer, inefficient collection of minority carriers generated deep in the absorber volume and an insufficient absorber thickness [18]. Compared to the EQE spectra previously reported for state-of-the-art CIGSSe samples we observe large losses in this region for all samples. The SEM micrographs in Figure 4.3 show that the CIGSSe absorber is only little thicker than 1 µm and relatively thin which might cause losses due to incomplete absorption of large wavelength photons. Simultaneously the ZnO:Al window layer is rather thick, designed to reduce the series resistance in the module, which enhances free-carrier absorption. Incomplete collection might be weakly dependent on sulfur content.

The limited carrier injection observed as a rollover in the IV characteristics at $V > V_{OC}$ and low temperature is strongest for samples S1 and S0, while S2 and S3 exhibit smaller impedance of the injection current (Figure 4.8). Three possible origins of the IV rollover are suggested [20]: 1) acceptor states located at the buffer/window interface 2) a large positive conduction band offset at the i-ZnO/CdS interface and 3) a barrier located at the interface between the chalcopyrite absorber and the back contact. Since the deposition of the buffer and window layers was performed in the same way for all samples, we may exclude options 1) and 2). A hole injection barrier at the back contact may be induced by a valence band offset at the Mo(Se,S)$_2$ and CIGSSe interface. The height of the valence band offset depends on the chemical composition of both films. The valence band position of Mo(Se$_{1-z}$,S$_z$)$_2$ and thereby the valence band offset to the absorber decreases linearly with increasing $z = [S]/[Se+S]$ ratio [25]. Different sulfur concentrations in Mo(Se,S)$_2$ result in different lattice constants. This would show up as a shift of the respective peak position in the XRD pattern which was not observed for S0/S1 ($z = 0.4$). Due to the small signal intensity of the Mo(Se,S)$_2$ XRD signatures in S2 and S3 and the poor spatial resolution of GDOES deeper in the device no determination of the corresponding z-values could be achieved which allows only for speculation on this matter.
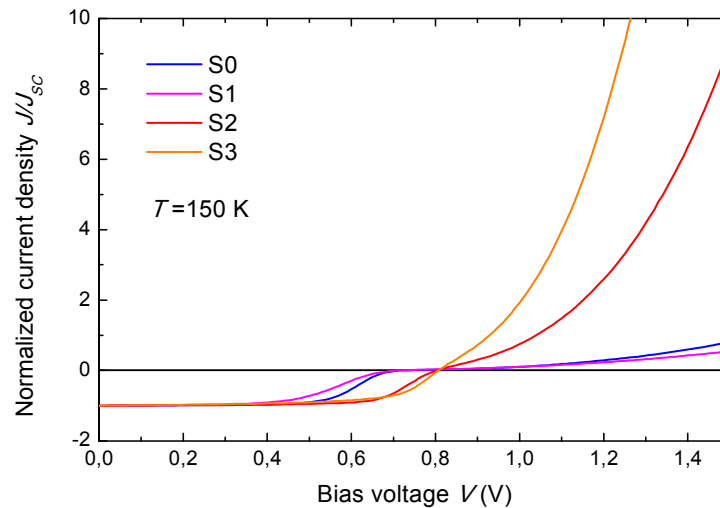
Figure 4.8 Current-voltage characteristics of samples S0-S3 at 1 sun illumination at $T = 150$ K. The current density was normalized for clarity.

For sulfur containing devices prepared with the sequential deposition reaction method it is known, that the sulfur concentration increases not only towards the heterojunction but also in the vicinity of the back contact, e.g., by diffusion of sulfur along grain boundaries [26,27]. Assuming that the larger sulfur availability during Mo(Se,S)$_2$ formation results in a higher [S]/[S+Se] ratio in the Mo(Se,S)$_2$ layer, the position of the valence band would decrease [28]. Consequently the hole injection barrier in devices containing more sulfur would decrease giving one possible answer to a decreased rollover in S2/S3. This is not reflected in S1 compared to S0 which could be due to inhibited sulfur diffusion or might be related to the increased thickness of the Mo(Se,S)$_2$ layer in this particular device. However, in order to confirm this model further investigations of the chemical composition are required, e.g. by STEM-EDX which is capable to image the chemical composition of the internal interface with high spatial resolution.

Since the J_{SC} does not change much with sulfur content in the device the observed performance deviations originate from the fill factor FF and V_{OC} both summarized in Table 4.1. In sequentially processed chalcopyrite solar cells, whose surface is almost fully depleted of gallium, the commonly observed increase of V_{OC} in sulfurized devices was attributed to the passivation of recombination centers [10]. This hypothesis matches the trend of the saturation current density J_0 in our samples which is reduced by approximately three orders of magnitude in samples processed with higher sulfur concentration, i.e., S2 and S3 (Table 4.1). Comparing only the samples with larger sulfur content we observe that S3 has slightly lower efficiency than S2. The larger V_{OC} cannot compensate the lower J_{SC}. Comparing the samples with lower sulfur concentration sample S1 exhibits a temperature dependent ideality factor. According to [19] this can be modeled by tunneling-assisted recombination via energetically distributed defect levels in the SCR

$$\frac{1}{A} = \frac{1}{2}\left(1 + \frac{T}{T^*} - \frac{E_{00}^2}{3(kT)^2}\right) \tag{4.5}$$

where T^* relates to a characteristic energy of the distribution of the recombination centers and E_{00} is the characteristic tunneling energy. The measured data can be fit very well with this model giving $E_{00} = 15.6$ meV for S1 and $T^* = 231$ meV. In order to determine the activation energy for S1 the temperature independent ideality factor $A = 2$ is used. The E_a calculated with this correction is given in Table 4.1 and is lower than the interface bandgap of this device (see Figure 4.1). This suggests an additional interface recombination channel which reduces V_{OC} below the value obtained for S0 which contains even less sulfur.

The DLTS results clearly show the presence of mid-gap minority defects. According to literature no mid-gap minority traps were found in theoretical calculations, whereas for the majority defect the Cu_{In} (-/0) anti-site defect is a likely candidate [29]. The calculation of N_t for the minority carrier defect needs some further discussion since the transients at room temperature shown in Figure 4.7 reflect a superposition of a majority and a minority defect emission. The fundamental shape of the DLTS transients is indicative of a majority defect state. However, the curves do not saturate at C_0 for long transient recording time. This behavior can be qualitatively understood by assuming minority carrier emission with a time constant which is considerably higher than that describing the majority carrier emission. The ratio of the time constants τ_n/τ_p is roughly estimated by extrapolating the linear fit of the majority and minority traps in Figure 4.6 to the abscissa value corresponding to the temperature of the shown transients. Ratio values between 20 (S0) and 10^4 (S2) support the assumption of minority carrier emission with a comparatively large time constant. Since the minority carrier emission transient extends over a far longer timescale than that of the majority carrier emission, the contribution of the minority traps to the junction capacitance effectively shifts the majority transient upwards proportional to the minority trap concentration (see Eq. (4.3)). Assuming the same origin of the majority traps and identical minority carrier emission rates for both samples the observed shift can be assigned to a density of occupied trap states which is substantially larger in S0 than in S2 ($N_t^{S0}/N_t^{S2} \sim 20$). This finding qualitatively confirms the passivation of mid-gap minority carrier traps by sulfur and explains the observed improvement of V_{OC}.

4.4 Conclusions

We investigated CIGSSe solar cells processed in an industrial production line via the deposition-reaction method. The solid state reaction was carried out via rapid thermal processing of metal precursors in a chalcogene-containing atmosphere while the amount of sulfur was varied between the samples. Structural analysis confirmed the sulfur incorporation into the absorber surface and separation of a Ga-depleted phase close to the front and a Ga-rich phase close to the back contact. We detect differences in the formation of an intermediate Mo(Se,S)2 layer which we assume to be responsible for the different IV rollover characteristics observed at low temperatures. On increasing sulfur incorporation the short circuit current density decreases due to a larger band gap which on the other hand results in a larger open circuit voltage. With respect to samples S0/S1 which have been exposed to a sulfur-free or sulfur–poor atmosphere we observed a substantial improvement of the device performance for samples exhibiting considerable sulfur incorporation. The improvements were essentially indicated by an increase of the fill factor and the open circuit voltage. The latter observation could not be caused by the band gap widening in the surface region of the CIGSSe absorber alone and is explained by passivation of mid-gap recombination centers in the space charge region by sulfur. With DLTS we unambiguously confirmed the presence of such minority trap centers. Based on the analysis of the capacitance transients of samples S0 and S2 we concluded that the defect concentration is reduced by about one order of magnitude by addition of sulfur. The poor performance of sample S1 (small amount of sulfur) is further reduced by interface recombination This large defect concentration in S0/S1 is the origin of the strong carrier recombination in the space charge region as reflected in the large ideality factor and strongly increased saturation current density.

References:

[1]   T. Dullweber, G. Hanna, U. Rau, H.W. Schock, Solar Energy Materials and Solar Cells 67 (2001) 145–150.

[2]   V. Alberts, Materials Science and Engineering: B 107 (2004) 139–147.

[3]   D.L. Young, J. Abushama, R. Noufi, X. Li, J. Keane, T.A. Gessert, J.S. Ward, M. Contreras, M. Symko-Davies, T.J. Coutts, in:, Proceedings of the 29th IEEE PVSC, 2002, pp. 608–611.

[4]   M.A. Green, K. Emery, Y. Hishikawa, W. Warta, E.D. Dunlop, Progress in Photovoltaics: Research and Applications 20 (2012) 606–614.

[5]   V. Alberts, Thin Solid Films 517 (2009) 2115–2120.

[6]   M. Alonso, K. Wakita, J. Pascual, M. Garriga, N. Yamamoto, Physical Review B 63 (2001) 1–13.

[7]   V. Alberts, M. Klenk, E. Bucher, Thin Solid Films 387 (2006) 44–46.

[8]   T. Nakada, H. Ohbo, M. Fukuda, A. Kunioka, Solar Energy Materials and Solar Cells 49 (1997) 261–267.

[9]   S.-H. Wei, A. Zunger, Journal of Applied Physics 78 (1995) 3846.

[10   U. Rau, M. Schmitt, F. Engelhardt, O. Seifert, J. Parisi, W. Riedl, J. Rimmasch, F. Karg, Solid State Communications 107 (1998) 59–63.

[11]   D.V. Lang, Journal of Applied Physics 45 (1974) 3023.

[12]   M. Igalson, M. Wimbor, J. Wennerberg, Thin Solid Films 403-404 (2002) 320–324.

[13]   V. Probst, W. Stetter, W. Riedl, H. Vogt, M. Wendl, H. Calwer, S. Zweigart, K.-D. Ufert, B. Freienstein, H. Cerva, F.. Karg, Thin Solid Films 387 (2001) 262–267.

[14]   V. Probst, F. Hergert, B. Walther, R. Thyen, B. Neumann, A. Windeck, T. Letzig, A. Gerlach, in:, Proceedings of the 24th EU PVSEC, 2009, pp. 2455–2459.

[15]   S.-H. Chang, M.-Y. Chiang, C.-C. Chiang, F.-W. Yuan, C.-Y. Chen, B.-C. Chiu, T.-L. Kao, C.-H. Lai, H.-Y. Tuan, Energy & Environmental Science 4 (2011) 4929.

[16]   N. Kohara, S. Nishiwaki, Y. Hashimoto, T. Negami, T. Wada, Solar Energy Materials and Solar Cells 67 (2001) 209–215.

[17]   W.N. Shafarman, L. Stolt, in:, A. Luque, S.S. Hegedus (Eds.), Handbook of Photovoltaic Science and Engineering, Wiley-VCH, Weinheim, 2003, pp. 567–616.

[18]   S.S. Hegedus, W.N. Shafarman, Progress in Photovoltaics: Research and Applications 12 (2004) 155–176.

[19] U. Rau, H.W. Schock, Applied Physics A: Materials Science & Processing 69 (1999) 131–147.

[20]   R. Scheer, H.W. Schock, Chalcogenide Photovoltaics: Physics, Technologies, and Thin Film Devices, Wiley-VCH, Weinheim, 2011.

[21]   T. Walter, R. Menner, C. Köble, and H.W. Schock, in: Proceedings of the 12th EC PVSEC, 1994, pp. 1755–1758.

[22] J. Heath, P. Zabierowski, in:, D. Abou-Ras, T. Kirchartz, U. Rau (Eds.), Advanced Characterization Techniques for Thin Film Solar Cells, Wiley-VCH, Weinheim, 2011, pp. 81–106.

[23] ASTM, Standard G173, Standard Tables for Reference Solar Spectral Irradiances: Direct Normal and Hemispherical on 37° Tilted Surface, American Society for Testing and Materials, West Conshocken, PA, USA. (2012).

[24] J. Nelson, The Physics of Solar Cells, Imperial College Press, London, 2003.

[25] M.K. Agarwal, Physica Status Solidi (a) 95 (1986) 303–307.

[26] T. Nakada, H. Ohbo, T. Watanabe, H. Nakazawa, M. Matsui, A. Kunioka, Solar Energy Materials and Solar Cells 49 (1997) 285–290.

[27] A. Halani, C. Leidholm, G. Norsworthy, V.K. Kapur, A. Swartzlander, R. Matson, Progress in Photovoltaics: Research and Applications 8 (2000) 227–235.

[28] H. Jiang, Journal of Physical Chemistry C 116 (2012) 7664–7671.

[29] S.-H. Wei, S.B. Zhang, A. Zunger, Applied Physics Letters 72 (1998) 3199.

4.A   Post-publishing results

The investigations on sulfur incorporation into chalcopyrite solar cells processed via the deposition-reaction method left some questions unanswered. A comparison of the current-voltage anomaly at low temperatures between the samples investigated in chapter 3 and 4 reveals that the roll over intensity does not correlate with the exposition to sulfur. In chapter 3 the roll over is strongest in those samples which were exposed to sulfur, however, in chapter 4 the contrary was observed and the roll over appeared to be less strong the more the samples were exposed to sulfur. As suggested in section 4.3 the characteristics of the Mo(S,Se)$_2$ layer might be decisive in this question and the application of the proposed chemical profiling methods with higher depth resolution at the absorber/back contact interface might clarify the contrasting behavior between the samples from the different measurement series.

Another deviation between the samples from chapter 3 and 4 was observed in the doping profiles. In section 4.2.4 the effective doping concentrations at zero voltage bias were given which were extracted from the doping profiles shown in Figure 4.9. A comparison with Figure 3.6 reveals that in chapter 4 the sample not exposed to sulfur yields a lower doping concentration compared to samples exposed to sulfur and vice versa in chapter 3. The origin of the different doping profiles could not be identified, yet. In chapter 2.2.2 the influence of selenium pressure and sodium on the doping concentrations was discussed. Specific details about any changes of these two constituents between the production of the two sample series are unavailable and only speculation is possible. However, both measurement series were processed during the ramp up of a commercial production line several months apart. During the ramp up the specifics of the processing parameters change rather quickly, therefore it seems plausible that parameters like partial pressures of the chalcogenes in the reactive atmosphere or the provision of sodium changed as well. As these parameters influence the doping concentration profiles strongly, a comparison of the two measurement series in this aspect appears to be futile.
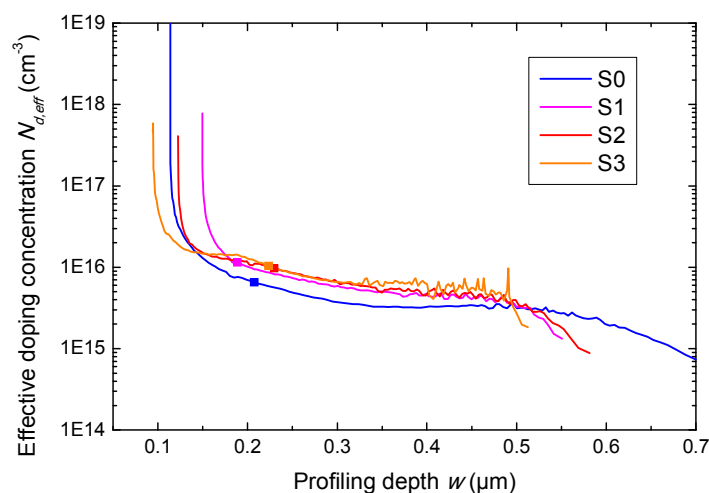
Figure 4.9:   Profiles of the effective doping density of CIGSSe samples exposed to different concentrations of sulfur during absorber formation

The observation of these two differences might raise the question, if the rollover could actually be determined by the characteristics at the heterojunction instead of the back contact. However, no correlation of the rollover behavior to the doping profiles could be found. Additionally it was

already pointed out in chapter 2.3.3, that the strong increase of the doping concentration towards the heterojunction has to be treated with care as those values were extracted from a strongly biased device. In order to distinguish the influence of the heterointerface and the back contact methods selective to either of these regions have to be applied.

5 Article III: Investigation of Cu(In,Ga)Se$_2$ Solar Cell Performance Deviations in Nominally Equal Absorbers

Investigation of Cu(In,Ga)Se$_2$ Solar Cell Performance Deviations in Nominally Equal Absorbers

Robin Knecht, Jürgen Parisi, Ingo Riedel,

Raymund Schäffler, and Bernhard Dimmler

Abstract

Cu(In,Ga)Se$_2$ (CIGSe) solar cells were fabricated independently by industrial scale co-evaporation in two separate production lines with the same nominal composition and thickness of the absorber film. Although the device properties were believed to be the same we observed substantial deviations of the respective values of the open circuit voltage (ΔV_{OC} = 40 mV) and of the fill factor (ΔFF = 4%), whereas the short circuit current was essentially the same. We performed fundamental device analysis, space charge and defect spectroscopy, transient photoluminescence as well as in-depth profiling of the chemical gradients of the absorber films. Using the results from the experiments we set up a simulation baseline which allowed us to conclude that the apparent deviations can be related to the presence of deep recombination centers with different concentration within the CIGSe absorber as well as to variations of the band gap grading.

5.1 Introduction

Among all thin-film technologies Cu(In,Ga)Se$_2$ (CIGSe) solar cells to date demonstrate the highest power conversion efficiencies with a champion lab scale efficiency of 20.3% [1].However, satisfactory transfer of this performance to industrial scale is not straightforward as the well defined homogeneous absorber formation on large areas presents a major challenge and ohmic losses are introduced by integrated series connection of the cell stripes. Due to limited opportunities for inline characterization differences of the film properties might remain undetected until the final current-voltage (I-V) characterization step is performed. We investigated CIGSe solar cells (cut from large-area modules) with light absorbers independently processed in separate co-evaporation chambers. Both samples have been prepared under the same nominal process conditions and yield the same elemental composition as confirmed by X-ray fluorescence spectroscopy (XRF) measurements. However, the two samples exhibit a significant performance deviation (Figure 5.1 and Table 5.1) which highlights that not all influences during absorber and interface formation are controlled in such detail to realize equal cell performance. In a detailed experimental analysis of the two samples we tried to identify the relevant properties responsible for the observed performance difference. The collection efficiency for minority charge carriers is evaluated by analysis of the space-charge region (SCR) characteristics via capacitance-voltage (C-V) measurements and by estimation of the minority carrier lifetime as deduced from time-resolved photoluminescence (TRPL). The recombination of photogenerated charge carriers via deep recombination centers within the SCR was studied in detail by thermal admittance (TAS) and transient defect spectroscopy (DLTS). Together with results obtained from in-depth profiling of the chemical gradients by glow discharge emission spectroscopy (GDOES) we created a baseline model for simulations with SCAPS-1D [2] which allows us to simulate the experimental device characteristics for analysis of the specific characteristics of the two studied sample types.

5.2   Experimental Procedure

5.2.1   Sample preparation

The absorber films of the investigated samples were prepared by inline single step CIGS co-evaporation on 60 x 120 cm^2 molybdenum coated glass sheets in two different evaporation chambers in the CIS Fab of Wuerth Solar. The nominal process parameters relevant for the absorber formation were the same with the average Ga/(Ga+In) in the range of 0.33 and the average Cu/(Ga+In) in the range of 0.74-0.78. Details of the production process have been described elsewhere [3]. The samples consist of a layer stack in the conventional sequence glass/Mo/CIGSe/CdS/i-ZnO/ZnO:Al with an absorber film thickness in the range of 2.0-2.3 µm. The large samples were cut into smaller pieces (~0.4 cm^2) for further investigation. For the energy dispersive X-ray spectroscopy (EDX) measurements of the CIGSe thin films we removed the window and buffer layers in 5% hydrochloric acid. For application of EDX to the absorber surface at the back contact we applied a glue strip on the absorber front surface and put it into liquid nitrogen which caused the absorber to lift off very cleanly from the intermediate MoSe$_2$ between CIGSe and the back electrode.

5.2.2   Results

After production the samples were investigated by XRF which yielded the same Ga/(Ga+In) ratio (GGI), the same copper content and the same thickness. However, measuring the I-V characteristics of the solar cells under standard test conditions (STC) revealed considerable deviations of the cell performances. Figure 1 depicts larger values of the open circuit voltage (V_{OC}) and the fill factor (*FF*) of sample with identifier *high* resulting in improved power conversion efficiency (η) compared to the other sample (identifier: *low*).
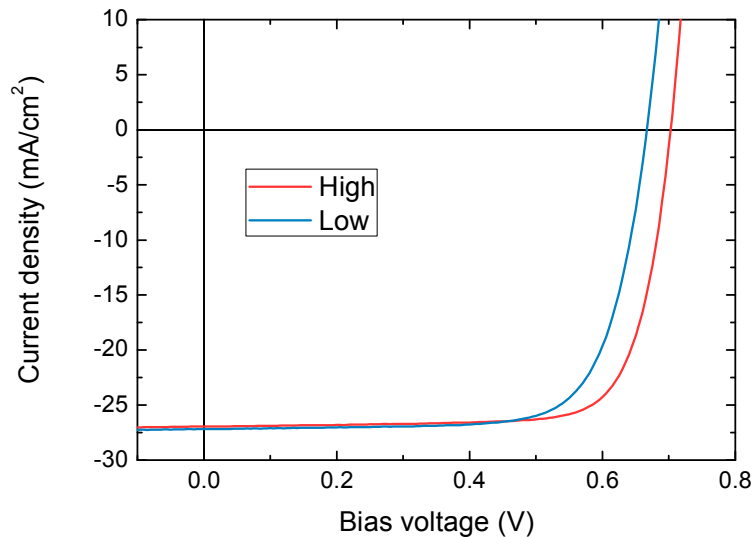
Figure 5.1:   Experimental I-V characteristics (standard test conditions) of two CIGSe samples nominally processed under the same conditions in two independent co-evaporation chambers.

The short circuit current densities (J_{SC}) of both samples are basically the same which is confirmed by integrating the respective EQE spectra (not shown). Since CIGSe is a direct semiconductor the minimum bandgap $E_{g,min}$ of the absorbers can be determined by a linear fit of the low-energy

Sample	FF (%)	V_{OC} (mV)	J_{SC} (mA/cm^2)	J_0 (A/cm^2)	η (%)	W_{SCR} (nm)	$E_{g,min}$ (eV)
High	79.1	701	25.8	1.3×10^{-9}	14.2	440	1.19
Low	75.3	661	25.9	2.8×10^{-9}	12.9	406	1.17

Table 5.1 Cell parameters for the two samples types determined from I-V, C-V, and EQE measurements

slope of the $EQE^2(E)$ plot, where E is the photon energy. Using this method we determined a minimum optical bandgap of about 1.19 eV for sample *high* and 1.17 eV for the sample *low*. The difference of 20 meV is too small to explain the observed difference ΔV_{OC} = 40 mV. These results do not change upon illumination with white light bias of one sun. These differences in current-voltage performance were reproduced with a large set of samples which were taken from all over the module thus confirming a good spatial homogeneity.

For a given thickness of the absorber film the width of the space charge region W_{SCR} and the minority carrier diffusion length $L_{D,n}$ determine the collection efficiency of a photovoltaic device. We used C-V measurements to extract the width W_{SCR} of the SCR from the depletion capacitance $C(V=0)$ at zero voltage bias using

$$W_{SCR} = \frac{\varepsilon_r \varepsilon_0 A}{C(V=0)},$$ (5.1)

where ε_r is the relative permittivity, ε_0 the vacuum permittivity, A the cell area and C the measured capacitance. For sample *high* we obtained W_{SCR} = 440 nm which is by ΔW_{SCR} = 34 nm larger than the SCR width of sample *low* which suggests differences of the carrier collection efficiency of both samples. Using this method we could also obtain the effective carrier concentration N_D for the *high* sample to be 8.42×10^{15} cm^{-3} compared with the only slightly higher concentration of 1.00×10^{16} cm^{-3} in the *low* sample.

We also observe a difference in the saturation current density J_0 (Table 5.1) which strongly influences the open circuit voltage according to equation

$$V_{OC} = \frac{nkT}{q} \ln\left(\frac{J_{SC}}{J_0} + 1\right),$$ (5.2)

where k is Boltzmann constant, T the sample temperature, n the diode ideality factor, and q the elementary charge. The saturation current density reflects the contributions of the diffusion and recombination characteristics. From I-V measurements we extract the saturation current density as 2.8×10^{-9} A/cm^2 for the *low* and 1.3×10^{-9} A/cm^2 for the *high* sample thus suggesting better diffusion parameters and therefore the higher open circuit voltage in the *high* sample. Several methods to determine the minority carrier diffusion length $L_{D,n}$ and lifetime τ_n were performed. The method of calculating $L_{D,n}$ from the inversed internal quantum efficiency [4] proved to be unreliable while measuring the TRPL lead to consistent results (Figure 5.2).

For this, we consider the characteristic decay time of the photoluminescence transient as the minority carrier lifetime which can be deduced from a biexponential fit of the TRPL signal $I(t)$ [5]:

$$I(t) = A_0 + A_1 e^{-\frac{t}{\tau_1}} + A_2 e^{-\frac{t}{\tau_2}} \text{,} \qquad (5.3)$$

where t is the time, A_0, A_1 and A_2 are fitting parameters. With an excitation intensity of about 2.5×10^{11} photons per pulse/cm^2 each with a wavelength of 633 nm the excitation was is the low injection regime. The meaning of the shorter time constant τ_1 is heavily debated in the literature [5-8] whereas the longer time constant τ_2 is commonly attributed to the minority carrier lifetime. Figure 2 shows the normalized decays of both samples. Both samples do not differ significantly in τ_1 but the difference in τ_2 can clearly be seen. The minority carrier lifetime amounts to τ_2 = 19 ns in sample *high* compared to τ_2 = 14 ns obtained for sample *low*. The ratio A_2/A_1 relates to the number of decays along the recombination path with τ_2 in relation to those with τ_1. In sample *high* the ratio A_2/A_1 is with about 2.0% slightly higher than in the *low* sample where A_2/A_1 = 1.7%, therefore the charge carriers do not only live longer in the *high* sample, but also relatively more charge carriers take this recombination path. Using the Einstein relation $L_{D,n} = \sqrt{D_n \tau_n}$ and assuming a diffusion constant D_n = 1 cm^2/s for both CIGSe samples yields reliable values of $L_{D,n}$ [9]. The larger minority carrier diffusion length in sample *high* leads to a better collection efficiency and therefore to a larger J_{SC}. This effect in combination with the slightly better reflection of the *high* sample compensates the generally expected drop of J_{sc} when the minimum bandgap decreases and therefore explains the small difference in the short circuit current densities. The observed difference of the bulk minority carrier lifetimes might be related to the presence of active defect states with different concentrations and capture rates in both samples.
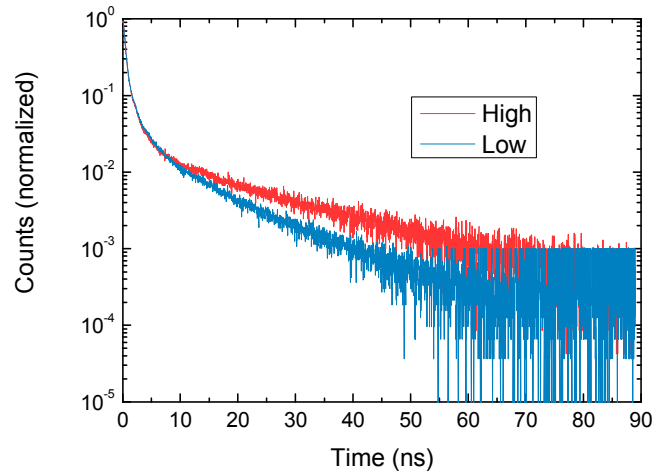
Figure 5.2: TRPL: The slope of the high sample (straight) shows a slower decay than the low sample (dotted) thus indicating reduced charge carrier recombination.

The analysis of the frequency- and temperature- dependent SCR capacitance gives access to electrically active defect states that are present in the absorber material. While TAS accesses rather shallow majority carrier trap states deeper levels can be identified with DLTS which enables identification of the charge state. Besides unspecific shallow states with activation energies (E_a) in the range of 30 meV both sample types (relaxed state) exhibit minority carrier trap states with similar activation energy ($E_a \approx$ 500 meV) being close to the center of the band gap. These states may act as recombination centers which could be assigned to Cu_{In} antisites

[10]. The high-efficiency sample shows an additional minority defect at $E_a \approx 75$ meV whereas a minority state with $E_a \approx 120$ meV was found in samples with lower efficiency. The presence of mid-gap states acting as recombination centers is generally detrimental for the device performance and particularly limits V_{OC}.

In order to investigate the samples for different chemical profiles in the absorber we applied EDX at the front and the back surfaces of the neat CIGSe absorbers. Within the measurement error, the atomic percentages of the compound constituents were identical in both samples except for a slightly higher Cu content in sample *low*. The same result was obtained for the back contact. However, both samples exhibit a 5% higher GGI value at the back surface than at the heterojunction indicating a significant bandgap grading in the material. Since the surface sensitivity of EDX is relatively poor and the chemical grading of the absorber material has a major impact on solar cell performance investigations with GDOES were carried out. With GDOES one obtains in-depth resolution of the chemical gradients and compositional properties of the thin films which were calibrated to the initial XRF data. The results revealed the in-depth variation of GGI and CGI from which the bandgap grading profiles (Figure 5.3) of the two sample types (unit: eV) was calculated for $Cu(In_{1-x}Ga_x)Se_2$ with [11].

$$E_g(x) = 1.02 + 0.67x + 0.11x(x-1). \tag{5.4}$$

Since GDOES was applied on complete cells we ignore the window layer which was determined in XRF measurements to be about 1 µm thick because we are only interested in the absorber composition. The heterojunction is therefore situated at about 1000 nm in Figure 5.3. In both cases the in-depth variation is qualitatively similar and can roughly be divided into three domains: (A) From the heterojunction to about 2000 nm in Figure 5.3 the bandgap is almost constant and only slightly decreasing and reaches the minimum bandgap at x = 2000 nm. As derived from GDOES data the minimum bandgap of the sample *high* is by 10 meV higher than the value obtained for the sample *low*. (B) In the middle of the absorber we observe a linear increase of the bandgap. In region (C) i.e., close to the back contact, the E_G values saturate. The most striking difference between the two profiles is the fact, that the grading steepness is much stronger in the *low* efficiency sample. The shape displayed in Figure 5.3 is typical for a double profile [12] obtained from a multi-step process which is surprising since only a one-step process was used.

5.3 Simulation

Using the presented results as well as absorption data of the ZnO:Al window layer (equal for both samples) and reflection measurements of the total stack we created a device model for SCAPS-1D where the CIGSe absorber was sectioned into the regions (A)-(C) as described above. Using the direct-semiconductor bandgap absorption model for CIGSe delivered by SCAPS-1D yields a too steep low-energy slope (compared to the measured data) in the simulated EQE spectra. However, measurement of the actual absorption coefficient of the individual CIGSe absorbers turns out to be quite difficult because of the high absorption. Hence we had to interpolate the CIGSe absorption spectra reported by Paulson et al. [13] and cut off the high-wavelength domain by the Gloeckler [14] absorption spectrum from the SCAPS-1D absorption file library.
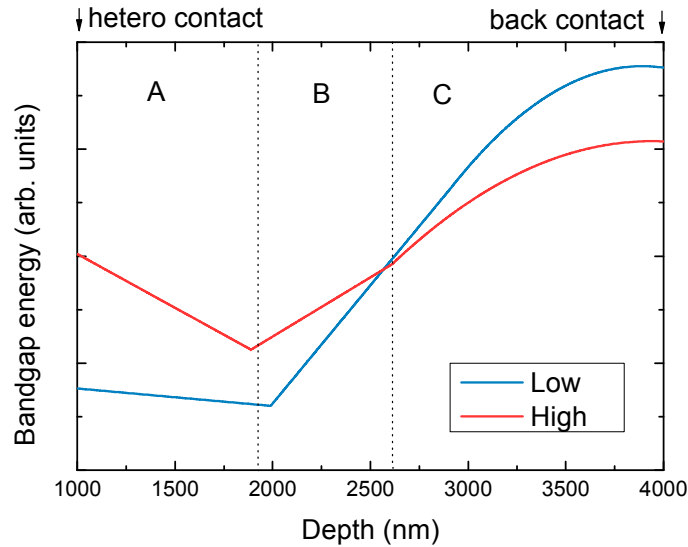
Figure 5.3: Bandgap profile as determined from GDOES measurements. The slope of the bandgap grading in the high sample is weaker, the minimum bandgap higher than the low sample (dashed). The heterojunction is situated at 1000 nm, the back contact at about 3750 nm.

In a first step, the device model was adjusted to fit the experimental EQE spectra and the I-V characteristics of the sample *low*. The result is shown in Figure 5.4 as a dashed line. The dotted line is the result if we take this model and only exchange the stack reflection and the band gap grading with the respective data of the *high* sample. The simulation shows, that the quantum efficiency did not change in a way corresponding to the experiment. Likewise, the I-V simulation yielded an increase of the open circuit voltage by 20 mV using the grading of the sample *high*, which accounts only for half of the observed ΔV_{OC}.
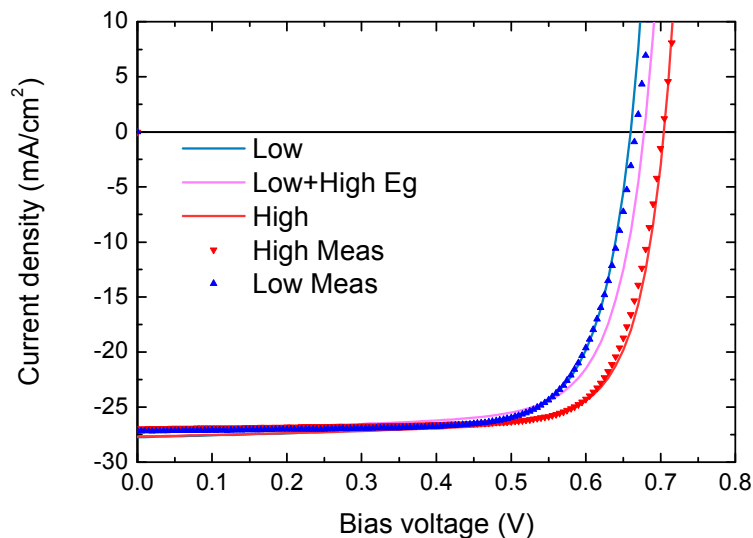
Figure 5.4: Simulated I-V characteristics: low sample (dashed) and low model adjusted with high reflection and bandgap grading (dotted). The open circuit voltage increases but only about half as much as measured. The symbols represent the measurement data (▲: low, ▼: high)

Since we observed differences in the minority carrier life time we adjusted the defect concentrations and capture cross sections for electrons and holes of the mid gap defect states, which have been experimentally confirmed. Other parameters were varied to check for possible other candidates to explain the observed effect. Although some gave small changes in the open circuit voltage none of the chosen parameters was able to do this without dramatic changes of FF as well. The straight line in Figure 5.4 shows the results after the adjustment of the parameters fitting the measurements quite well.

5.4 Conclusions

Two samples fabricated in different process chambers with nominally same process conditions showed significant differences in their macroscopic solar cell parameters as well as small differences in the width of the SCR and the minority carrier lifetime. While inline characterization methods provide only limited information about performance-critical properties like defects and bandgap grading these issues have to be explored by more detailed analysis in conjunction with device simulations. GDOES revealed substantial differences between the bandgap profiles of both sample types. The device with the higher efficiency exhibits a larger minimum energy gap than the sample with weaker performance allowing for a stronger splitting of the quasi Fermi levels and thus for higher V_{OC}. Moreover, the higher V_{OC} is in correspondence with the lower saturation current density obtained for the sample *high*. The cell with higher efficiency also presents a smaller gradient of the conduction band edge (E_C) towards the back contact. Our simulation studies confirm the importance to control the bandgap grading since a profile with a relatively weak grading already increases the open circuit voltage significantly. However, this change alone could not explain the experimental observations. The simulations suggest that the defect formation in both evaporation chambers is different resulting in changes of the minority carrier lifetime and thus the open circuit voltage. Unfortunately, we could not yet determine the origin of the deep defects as well as the bandgap grading. In order to validate the GDOES results further measurements are underway and will be cross-checked with the results from other in-depth profiling techniques like secondary neutral mass spectroscopy. For industrial absorber formation inline monitoring sensitive to the actual bandgap grading would improve the reliability of the process control and hence the mean module performance. Particularly, the further improvement of the simulation baseline could help to predict strategies for device optimization with regard to the chemical gradients of CIGSe absorbers.

References

[1]   M. A. Green, K. Emery, Y. Hishikawa, W. Warta, E.D. Dunlop, Progress in Photovoltaics: Research and Applications 19 (2011) 565.

[2]   M. Burgelman, P. Nollet, S. Degrave, Thin Solid Films 361-362 (2000) 527.

[3]   M. Powalla, M. Cemernjak, J. Eberhardt, F. Kessler, R. Kniese, H.D. Mohring, B. Dimmler, Solar Energy Materials and Solar Cells 90 (2006) 3158.

[4]   J. Parisi, D. Hilburger, M. Schmitt, U. Rau, Solar Energy Materials and Solar Cells 50 (1998) 79.

[5]   W.K. Metzger, I. L. Repins, M.A. Contreras, Applied Physics Letters 93 (2008) 022110.

[6]   B.M. Keyes, P. Dippo, W.K. Metzger, J. AbuShama, R. Noufi, Journal of Applied Physics 94 (2003) 5584.

[7]   S. Shirakata, T. Nakada, Thin Solid Films 515 (2007) 6151.

[8]   S. Shirakata, T. Nakada, Physica Status Solidi (c) 6 (2009) 1059.

[9]   M. Nishitani, T. Negami, N. Kohara, T. Wada, Journal of Applied Physics 82 (1997) 3572.

[10]   S. Zhang, S.H. Wei, A. Zunger, H. Katayama-Yoshida, Physical Review B 57 (1998) 9642.

[11]   S.H. Wei, A. Zunger, Journal of Applied Physics 78 (1995) 3846.

[12]   M.A. Contreras, J. Tuttle, A. Gabor, A. Tennant, K. Ramanathan, S. Asher, A. Franz, J. Keane, L. Wang, R. Noufi, Solar Energy Materials and Solar Cells 41-42 (1996) 231.

[13]   P.D. Paulson, R.W. Birkmire, W.N. Shafarman, Journal of Applied Physics 94 (2003) 879.

[14]   M. Gloeckler, A. L. Fahrenbruch, J.R. Sites, in:, Proceedings of the 3rd WCPEC, 2003, p. 491.

5.A   Post-publishing results

The inclusion of mid-gap interface defects in the simulation model is motivated by the results from defect spectroscopy which are shown in Figure 2.12a. The mid-gap defects could possibly be identified as Cu_{In} (2-/-) and the low energy traps could be attributed to the copper vacancies. The curved trap level is characterized for higher temperatures since at lower temperatures it is strongly influenced by the low level defect which leads to the observed flattening. The transition energy of about 80 meV and 120 meV respectively are in range 40 meV-160 meV which has often been related to the N1 defect, even though, additional annealing studies would be needed to support this.

The GDOES measurements used for the simulation published in the article were performed on complete samples including window and buffer layers. As previously pointed out in chapter 2.3.4 the depth resolution is negatively affected when the layer structure is not planar, and best results are only achieved for the uppermost layer. Therefore, subsequent GDOES measurements of the chemical profiles were performed on samples with removed window and buffer layers in order to check the validity of the previous profiles. As a second measurement method to profile the distribution of chemical elements in the same samples SNMS measurements were performed at the ZSW.
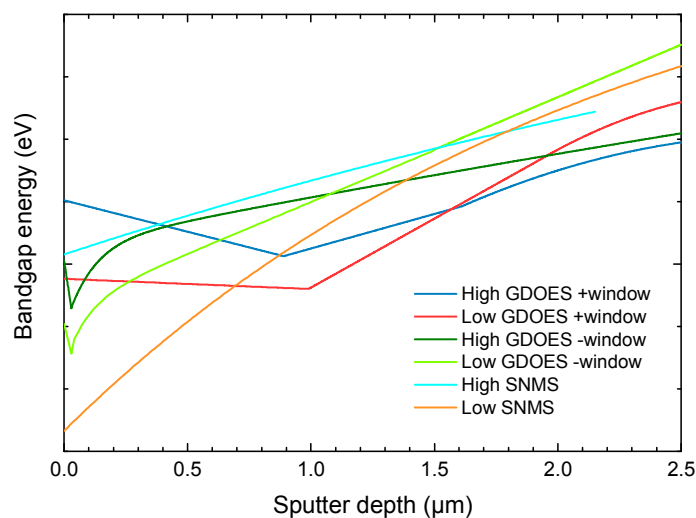
Figure 5.5:   Bandgap gradings as determined using various methods. All methods show the slope in the reddish sample to be steeper than in the bluish sample

All methods confirmed the steeper slope of the bandgap grading in the bulk and the lower minimum bandgap energy for the samples with lower open circuit voltage. Considering the low depth resolution the slopes in the bulk were comparable. However, the profiles differed in the details close to the heterojunction. Instead of the slight front bandgap widening towards the heterojunction as published in the article, SNMS measurements suggest a linear slope across the whole absorber. GDOES measurements on samples with removed window and buffer layers, even show a decrease of the interface bandgap towards the heterojunction with a widening only in the first nanometers of the absorber surface. While the latter measurement seems to be much more reliable than the GDOES measurements on complete devices, it could yet not be

clarified if the SNMS or the GDOES profiles are more trustworthy as the removal of the window layers potentially alters the element distribution.

The different profiles might also change the simulation results, therefore the bandgap gradings resulting from the newer chemical profiles need to be implemented into the device model in order to evaluate if the simulations deliver comparable results.
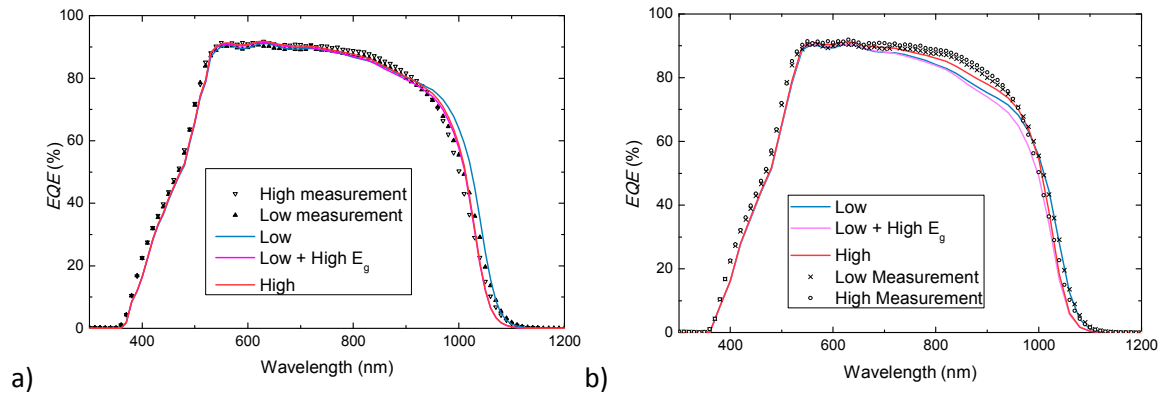
Figure 5.6: Calibration of the device model to fit quantum efficiency measurements a) implementing the bandgap grading as determined from GDOES measurements on devices with window layers and b) without window/buffer layers.

Figure 5.6 shows the preliminary results for simulations of a device model which implements the bandgap profile from the GDOES measurements on samples with and without window/buffer layers. Due to time constraints the calibration of the samples without window/buffer layers to the EQE measurements (Figure 5.6b) is in not as advanced as the calibration used for the simulations published in the article (Figure 5.6a). The simulations of the current-voltage measurements with the new device model are shown in Figure 5.7. A comparison with the corresponding plot of the simulation published in the article (Figure 5.4) shows that the conclusion made in the article still holds. A reliable calibration of a device model implementing the linear grading as measured by SNMS could not be realized within the scope of this thesis.
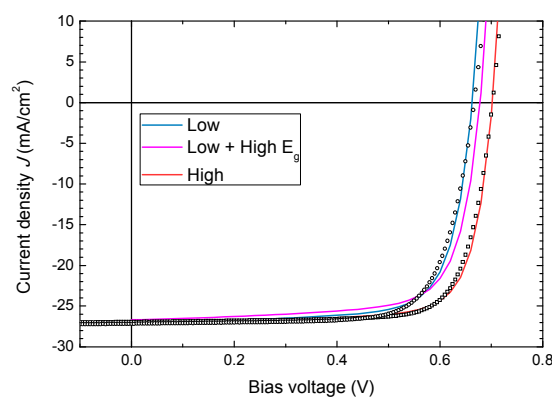
Figure 5.7: Calibration of the device model to fit current-voltage measurements implementing the bandgap grading as determined from GDOES measurements on devices without window/buffer layers.

6 Thesis conclusions

In this thesis a comprehensive characterization procedure has been established which has been applied on several absorber variations. Following this procedure the application of basic characterization methods on absorber variations revealed deviations in macroscopic quality factors. By using suitable more advanced measurement methods, the origin of the performance variations can be systematically traced back to fundamental device features, material properties and loss mechanisms. The identification of loss mechanisms in the device enables dedicated process optimizations, which is exemplified in the first project.

The initial investigation of samples obtained from the deposition-reaction method using rapid thermal processing concerned the exchange of H_2Se with H_2S in the reactive atmosphere during the later part of the annealing phase. The results showed an increased open circuit voltage and slightly higher fill factor in samples which were exposed to sulfur while the short circuit current and the minimal bandgap remained about constant. Temperature dependent current voltage measurements suggested a bandgap widening in the absorber at the heterointerface, and the analysis of the diode parameters implies that defects contribute to the observed behavior. The beneficial effect of sulfur is subsequently examined in further studies where the concentration of sulfur in the chalcogenization atmosphere was varied. In this study the previous observations were confirmed and the implied features investigated by more advanced methods. The application of glow discharge optical emission spectroscopy showed the band gap widening at the heterointerface, and by means of deep-level transient spectroscopy the increase of the open circuit voltage was unambiguously attributed to a passivation of mid-gap recombination centers. However, in order to find the optimal concentration of H_2Se and H_2S in the atmosphere more samples should be processed in more refined concentration steps and the influence on sulfur incorporation and grading depth investigated.

Further results from the characterization of this measurement series revealed differences in the formation of the intermediate $Mo(Se,S)_2$ layer at the back contact. With the available methods the influence of this layer on the device performance could not be completely solved. The application of methods with higher resolution deep within the absorber, e.g. STEM-EDX, is proposed to give more insight into this topic. However, the origin of the differences does not seem to be correlated with the sulfur content and is more likely due to different sample temperatures in contrast to constant temperatures of the atmospheres. Another unsolved phenomenon is the roll-over of the current voltage characteristic at low temperatures which might be related to this $Mo(Se,S)_2$ layer. The initial study showed an increased roll-over in samples exposed to sulfur, however, the contrary was observed in the second study which indicates that this effect is not related to the sulfur content.

The observation of poorly controlled processing conditions highlights that in order to achieve a homogeneous and reproducible manufacturing output the process parameters have to be very strictly controlled and their effect on the properties of the processed sample well understood. This question is elaborated upon in the second project carried out in collaboration with a different industry partner. Instead of the deposition-reaction method the new samples were manufactured using the co-evaporation process. Though the samples were processed with the same nominal co-evaporation parameters, their photovoltaic performance differed substantially regarding the value of the open circuit voltage. The application of multiple chemical profiling

methods on differently prepared samples revealed a stronger bandgap grading in the samples with the lower open circuit voltage. Since the integral chemical composition is equal, samples with larger slopes yield a lower bandgap minimum which partially explains the reduced open circuit voltage.

In order to test if the slope variation could further explain the remaining losses the results available from the characterization procedure were input into a one dimensional simulation tool. The results of these calculations fit the measurements and suggest that the remaining open circuit voltage deviation is caused by mid-gap defects modeled with different concentrations. However, the simulation baseline was just calibrated to fit quantum efficiency measurements and current voltage measurements under standard test condition. In order to obtain a robust simulation baseline the device model needs to be calibrated such that the optoelectronic device characteristics at different temperature and illumination conditions are satisfactorily emulated. Furthermore, capacitance measurements should be considered in the calibration as well, since capacitance simulations are supported by the applied simulation tool. Using the well calibrated device model as simulation baseline for further optimizations could then accelerate the development cycle of more efficient modules as the optimization strategies can be pursued by calculations instead of time consuming and expensive manufacturing variations.

In summary, the samples, which were investigated in both projects, showed similar features as origin of the observed performance deviations. Despite being processed differently and being investigated with a different focus, it is concluded for both projects that the bandgap grading and defect formation are essential material properties which should be controlled very well for the production of high quality reproducible devices. The characterization procedure presented in chapter 2.3 is far from exhaustive and includes mainly those methods suitable to give answers to the original problems of the different projects. Particularly, the implementation of absorption spectra in the simulation could be improved by a systematic characterization of graded CIGSSe absorbers by means of spectral ellipsometry instead of interpolation of literature values. This approach is mandatory to accurately model the local generation/recombination rates. For the scope of this thesis, however, the physical origins of the performance variation in very different devices could be identified by application of the established characterization procedure. This comprehensive perspective on the fundamental device and material properties is necessary for the understanding of the solar cell which is often not accessible with the methods available to the manufacturer. The knowledge gained about the dominating device loss mechanisms is valuable for more dedicated rather than purely empirical device optimizations and the results of this thesis emphasize the importance to accompany industrial process optimizations with an advanced and in-depth characterization procedure.

Lebenslauf

Robin Knecht

geboren am 5. August 1981
in Haiger

ledig

Promotion:

2. Dezember 2008 – 7. Dezember 2012	Universität Oldenburg, Abteilung Energie- und Halbleiterforschung *Characterization of industrially processed chalcopyrite solar cells with varied absorber composition* Abschluss: Dr.rer. nat. Prädikat: magna cum laude

Schul- und Hochschulausbildung:

Sommer 2002 – Sommer 2008	Justus-Liebig Universität Gießen Diplomarbeit am Institut für Angewandte Physik: *Präparation und Charakterisierung organischer Halbleiterkontakte mit hoher innerer Grenzfläche für photovoltaische Anwendung* Abschluss: Diplom-Physiker Note: 1,2
Sommer 2005 – Sommer 2006	Umeå Universitet, Schweden

Zivildienst:

Sommer 2001 – Sommer	Neurologische Klinik Braunfels

Schulbildung:

Sommer 1992 – Sommer 2001	Gymnasium Philippinum Weilburg Abschluss: Abitur Note: 1,4
Sommer 1998 – Sommer 1999	Jones County High School, Gray, Georgia, USA
Sommer 1988 – Sommer 1992	Grundschule Leun

Hundsmühler Str. 50, 26131 Oldenburg (Oldb),
E-Mail: Robin.Knecht@gmx.de, *Mobil:* (0176) 2198 2138

Printed publications

(1) D. Klaus, R. Knecht, A. Dragässer, C. Keil, D. Schlettwein, *„(Photo-)conduction measurements during the growth of evaporated bulk heterojunctions of a subphthalocyanine donor and a perfluorinated phthalocyanine acceptor*", Phys. Status Solidi A 206, 2723–2730 (2009)

(2) R. Knecht, M. Knipper, J. Ohland, I. Riedel, J. Parisi, *„Optoelectronic characteristics of $Cu(In,Ga)(S,Se)_2$ thin film solar cells obtained from varied chalcogenization processes*", Thin Solid Films 519 (2011) 7324–7327

(3) J. Parisi, D. Heinemann, W. Jürgens, R. Knecht, *„30 Years at the Service of Renewable Energies*", Einblicke (Forschungsmagazin der Carl von Ossietzky Universität Oldenburg), 54, 6 (2011)"

(4) R. Knecht, J. Parisi, I. Riedel, R. Schäffler, B. Dimmler, *„Investigation of CIGSe Solar Cell Performance Deviations in Nominally Equal Absorbers*", Japanese Journal of Applied Physics 51 (2012) 10NC07

(5) R. Knecht, M. S. Hammer, J. Parisi, I. Riedel, *„Impact of varied sulfur incorporation on the device performance of sequentially processed $Cu(In,Ga)(Se,S)_2$ thin film solar cells* ", Physica Status Solidi (a) (status: submitted)

Conference contributions

(1) R. Knecht, D. Schlettwein, "*Characterization of evaporated organic mixed films with varying ratios*", Materialforschungstag Mittelhessen 2008, Marburg

(2) R. Knecht, D. Schlettwein, "*Electronic and optical properties of evaporated organic bulk heterojunctions*", DPG-Frühjahrstagung 2008, Berlin

(3) D. Schlettwein, R. Knecht, "*Control of the Aggregation Characteristics in Mixed Donor-Acceptor Films for Evaporated Organic Bulk Hetero-Junctions*" DFG Schwerpunktprogramm 2008, Bad Honnef

(4) R. Knecht, M. Knipper, I. Riedel, J. Parisi, "*Influence of damp-heat exposure on the electronic properties of Cu(In,Ga)(S,Se)$_2$ thin film solar cells*", DPG-Frühjahrstagung 2009, Dresden

(5) R. Knecht, M. Knipper, I. Riedel, J. Parisi, "*Optoelectronic properties of Cu(In,Ga)(S,Se)$_2$ (CIGSSe) thin film solar cells obtained from varied chalcogenization processes*", DPG-Frühjahrstagung 2010, Regensburg

(6) R. Knecht, T. Klinkert, J. Parisi, I. Riedel, R. Schäffler, B. Dimmler, "*Investigation of Recombinatoric loss mechanisms in Cu(In,Ga)Se$_2$ Thin Film Solar Cells*", DPG-Frühjahrstagung 2011, Dresden

(7) M. Knipper, R. Knecht, I. Riedel, J. Parisi, "*Variation of sulfur content in Cu(In,Ga)(S,Se)2 thin film solar cells*", DPG-Frühjahrstagung 2011, Dresden

(8) R. Knecht, J. Parisi, I. Riedel, R. Schäffler, B. Dimmler, "*Investigation of Solar Cell Performance Deviations In Nominally Equal Absorbers*"PV-SEC 2011, Fukuoka

(9) R. Knecht, J. Parisi, I. Riedel, R. Schäffler, B. Dimmler, "*Investigation of CIGSe Solar Cell Performance Deviations In Nominally Equal Absorbers*", DPG-Frühjahrstagung 2012, Berlin

Erklärung gemäß §10 der Promotionsordnung

Hiermit erkläre ich, dass ich diese Arbeit selbstständig verfasst und nur die angegebenen Hilfsmittel benutzt habe.

Oldenburg, den 31. Oktober 2012
(Robin Knecht)

Acknowledgements

I am more than grateful that I did not need to embark on this journey alone and could count myself part of a very special fellowship. At this opportunity I would like to express my gratitude to all those individuals who contributed to this work and provided helpful advice and support: Sincerely I would like to thank…

… Prof. Dr. Jürgen Parisi, head of the Energy and Semiconductor Research Laboratory, for providing me with the opportunity to conduct my research and write this thesis in his group.

… Dr. Ingo Riedel, head of the photovoltaics group, for supervising this thesis and for always finding a slot in his ever occupied calendar, when discussion was needed

… the company which provided the samples from the sequential deposition-reaction process. Without naming the company or the employees I had the pleasure to work with I assume that my thanks will arrive at the right address.

… Manz GmbH for providing samples from the co-evaporation process. Especially I like to thank Raymund Schäffler for the many discussions and suggestions.

… Martin Knipper, for supervising me at the very beginning of my time in Oldenburg, before he joined the energy storage group and for his support with the XRD measurements.

… Torben Klinkert, the diploma student I had the pleasure to supervise, who contributed a lot to the project work with Manz and improved my understanding of the device by raising important questions.

… Dr. Jörg Ohland and Janet Neerken, for their support during everyday labwork and their morale raising attitude.

… our technical staff: Matthias Macke, Ulf Micolajak Thomas Madena, Holger Koch, Wilhelm Jürgens, and Andrea Geisler.

... Michael Powalla, Waltraud Wischmann, Oliver Kiowsky, and Axel Eicke from the ZSW for their attention and fruitful discussions at project meetings.

… my PhD fellows Jan Keller, Anton Werth, Julia Riediger, and Folker Zutz for sharing the good and bad times in the life of a PhD student. I further like to thank Kathrin Fuchs and Heiner Lendzian for the good atmosphere in my office during my first year.

… my other colleagues from the thin film group for the helpful discussions: Michael Richter, Viktor Gerlitz, Christiane Schroth, Nils Neugebohrn, Christiane Chory.

… Ela and Grit, our secretaries, for protecting me from the worst of bureaucracy.

… my parents, my brother and the rest of my family for the condition-less support only family can provide.

… my dearest Laura, who was always at my side and gave me the strength to go on.